STIMULATED COHERENT TRANSITION RADIATION[*]

Hung-chi Lihn

Stanford Linear Accelerator Center
Stanford University
Stanford, California 94309

---

[*]Ph.D thesis, Stanford University, Stanford, CA.

Abstract

Coherent radiation emitted from a relativistic electron bunch consists of wavelengths longer than or comparable to the bunch length. The intensity of this radiation outnumbers that of its incoherent counterpart, which extends to wavelengths shorter than the bunch length, by a factor equal to the number of electrons in the bunch. In typical accelerators, this factor is about 8 to 11 orders of magnitude. The spectrum of the coherent radiation is determined by the Fourier transform of the electron bunch distribution and, therefore, contains information of the bunch distribution.

This dissertation utilizes two aspects of coherent transition radiation, bunch information and high intensity, to study the stimulation of coherent transition radiation as a new source of high-intensity far-infrared radiation. Coherent transition radiation emitted from subpicosecond electron bunches at the Stanford SUNSHINE facility is observed in the far-infrared regime through a room-temperature pyroelectric bolometer and characterized through the electron bunch-length study. To measure the bunch length, a new frequency-resolved subpicosecond bunch-length measuring system is developed. This system uses a far-infrared Michelson interferometer to measure the spectrum of coherent transition radiation through optical autocorrelation with resolution far better than existing time-resolved methods. Hence, the radiation spectrum and the bunch length are deduced from the autocorrelation measurement.

To study the stimulation of coherent transition radiation, a special cavity named

BRAICER is invented. Far-infrared light pulses of coherent transition radiation emitted from electron bunches are delayed and circulated in the cavity to coincide with subsequent incoming electron bunches. This coincidence of light pulses with electron bunches enables the light to do work on electrons, and thus stimulates more radiated energy. The stimulation of radiation is observed through detuning measurements of the cavity and agrees with theoretical predictions.

The possibilities of extending the bunch-length measuring system to measure the three-dimensional bunch distribution and making the BRAICER cavity a broadband, high-intensity, coherent, far-infrared light source are also discussed.

Acknowledgements

It takes more than one person's effort to put all the necessary equipment, experiments, as well as knowledge together to make this a successful thesis. Among all the people who have helped me with this thesis work, I first would like to thank my thesis advisor Prof. Helmut Wiedemann for suggesting this thesis topic, guiding through the project, and offering a great environment at SUNSHINE for a broad range of graduate training. Next, I would like to thank my colleagues: Dr. Pamela H. Kung, David Bocek, Jim Sebek, Michael Hernandez, and Chitrlada Settakorn for their help, suggestions, and friendships. I also would like to thank Michael Baltay and Ramona Theobald at Stanford Synchrotron Radiation Laboratory for their technical assistance. I am grateful to Profs. Todd I. Smith and Zhi-Xun Shen for their efforts in reading, approving, and making suggestions to this thesis. Special thanks also go to Prof. P. L. Richards at University of California at Berkeley for his useful introduction to techniques of far-infrared experimentation. Finally, I would like to thank my wife Chih-chun, my parents, as well as my brothers and sister for their firm support through the whole thesis work.

Contents

List of Tables

List of Figures

Chapter 1

Introduction

The progress in the development of new high-intensity light sources has always played an important role in helping the progress in the study of various phenomena in science. Not only do these new light sources widen the roads of study by providing powerful and effective tools to speed up existing experiments and increase the accuracy of measurements, but they also open up brand new avenues of study in areas where human beings have never explored before because of the limitations of old low-intensity light sources. In the past, many light-producing processes such as laser and synchrotron radiation have been studied and used as powerful light sources in different spectral regimes from near infrared light to hard x-rays. These new light sources have enabled many new directions of research in science, such as non-linear optics and x-ray surface science, which can not be done by traditional low-intensity light sources.

However, in the far-infrared regime, no high-intensity light sources are generally available so far, and the conventional blackbody-type sources such as mercury arc lamps are still the most widely used as light sources. These low-intensity sources have become the major limitation of applications in this regime. Since the usable signal level is limited by the sources' low intensity, methods to reduce the effect of thermal

noises such as using liquid helium to cool down detectors' temperature and averaging over large numbers of measurements have to be employed in order to increase the accuracy of measured data. These methods significantly increase the complexity of experimental apparatus as well as the time required to prepare and run experiments. Yet the improvement in accuracy sometimes is not effective. Hence, the need for high-intensity light sources in the far-infrared regime is obvious. Although there are new developments in free-electron and chemical lasers targeting at this regime, new ways to produce broadband, high-intensity, coherent light covering this regime still need to be explored because of the spectroscopic nature of many applications.

On the other hand, the reduction of longitudinal phase space volume, especially the electron bunch length, of electron sources has become an interesting direction in the development of accelerators. New techniques are becoming available to produce electron bunch lengths in the subpicosecond range. When such short electron bunches radiate, the emitted light is coherent, and its spectrum covers most part of the far-infrared regime. Since there are typically 10^8–10^{11} electrons in these bunches, the radiated intensity can be expected to be significantly higher than that from the conventional low-intensity lamps in the far-infrared regime.

Therefore, the production of subpicosecond electron bunches provides a new direction in the generation of broadband, high-intensity, coherent, far-infrared light. This thesis has explored a new way using stimulated transition radiation emitted from the subpicosecond electron bunches generated at the Stanford SUNSHINE facility to produce high-intensity, coherent, far-infrared radiation. This chapter introduces the coherent radiation emitted from an electron bunch and provides the background knowledge for the central part of the thesis. The chapter also describes the subpicosecond bunch length generation and compression scheme used at the Stanford SUNSHINE facility, where all the experiments in this thesis are performed.

As described in the second chapter, a new autocorrelation method using a far-infrared Michelson interferometer has been developed as part of this thesis to characterize the spectrum of coherent transition radiation emitted from electron bunches and, furthermore, to measure the electron bunch length. The experimental results have verified the production of subpicosecond electron pulses at SUNSHINE. As the first frequency-resolved subpicosecond bunch length measuring system, this method has been demonstrated at SUNSHINE as a convenient, simple, compact, and transportable electron beam instrument with much higher resolving power than any existing time-resolved method. The possibility of extending this method to measure the three-dimensional bunch distribution is also discussed.

In the final chapter, a newly invented device named the BRAICER cavity is introduced which circulates coherent transition radiation emitted from previous electron bunches and coincides these light pulses with subsequent incoming bunches to stimulate more radiated energy from the electrons. The detuning measurement of this cavity confirms the observation of stimulated coherent transition radiation for the first time and proved the principle of this new idea of producing high-intensity far-infrared radiation through the stimulation of coherent transition radiation. Following the experimental verification of this idea, new ways of using stimulated coherent transition radiation emitted from subpicosecond electron bunches as broadband, high-intensity, far-infrared light sources are proposed. Not only will this new far-infrared light source provide broadband, high-intensity radiation for existing applications, its subpicosecond time structure will also facilitate new designs of pump-probe applications in the far-infrared regime.

1.1 Coherent Radiation from an Electron Bunch

Since the radiation emitted from subpicosecond electron bunches provides a promising source for high-intensity, far-infrared radiation, it is worth taking a closer look at a bunch of electrons radiate. The spectral field variations for different radiating processes involving only a single electron such as synchrotron and transition radiation have been very well studied. When a bunch of N electrons participate in a radiating process, the total emitted field at the observation point is the sum of the single-electron field emitted from each electron in the bunch with an appropriate phase factor associated with that electron.

Therefore, according to the emitted wavelength compared to the length of the electron bunch, the radiated spectrum can be divided into to two parts. For wavelengths shorter than the bunch length, fields emitted from all electrons in the bunch are at random phases, and they add up incoherently. Hence, the total intensity is only proportional to N, the number of electrons in the bunch. This is called the incoherent part. On the other hand, for wavelengths longer than the bunch length, fields emitted from all electrons are at about the same phase, and they add up coherently. Hence, the total intensity is proportional to N^2. This is called the coherent part. It is clear that the coherent part has N times more intensity than its incoherent counterpart. This coherent enhancement due to electron bunching was first predicted by Motz[1]. The difference in intensity is about 8–11 orders of magnitude in typical accelerators. Therefore, if the bunch length is in the subpicosecond range, the corresponding high-intensity coherent part of the radiated spectrum is in the far-infrared regime.

1.1.1 The Theoretical Perspective

The theoretical derivation of coherent radiation emitted from bunched electron beam has been carried out by Nodvick and Saxon[2]. To show the theory, let us first assume the following geometry that $\mathbf{R} \equiv R\,\hat{\mathbf{n}}$ is the position vector of length R from the observation point to the center of the bunch which contains N monoenergetic electrons, and $\mathbf{r}_j$ is the position vector from the center of the bunch to the jth electron[1]. Hence, the vector from the jth electron to the observation point is

$$\mathbf{x}_j \equiv x_j\hat{\mathbf{n}}_j = \mathbf{R} + \mathbf{r}_j, \tag{1.1}$$

where $\hat{\mathbf{n}}_j$ is the unit vector directed from the jth electron to the observation point. The total electric field from the bunch measured at the observation point at frequency ν is, therefore, the sum of the electric field emitted from the jth electron with the phase factor $e^{i\mathbf{k}_j\cdot\mathbf{x}_j}$, i.e.,

$$
\begin{aligned}
\mathbf{E}_{\text{total}}(\nu) &= \sum_{j=1}^{N} \mathbf{E}_j(\nu)e^{i\mathbf{k}_j\cdot\mathbf{x}_j} \\
&= \sum_{j=1}^{N} \mathbf{E}_j(\nu)e^{2\pi i(\nu/c)\hat{\mathbf{n}}_j\cdot\mathbf{r}_j}\, e^{2\pi i(\nu/c)\hat{\mathbf{n}}_j\cdot\mathbf{R}},
\end{aligned}
\tag{1.2}
$$

where $\mathbf{k}_j = 2\pi(\nu/c)\hat{\mathbf{n}}_j$ is the wave vector of the electric field from the jth electron. Using far-field approximation (i.e., $R \gg r_j$), we have $\hat{\mathbf{n}}_j \approx \hat{\mathbf{n}}$ and $\mathbf{E}_j(\nu) \approx \mathbf{E}_e(\nu)$ for all the electrons in the bunch, where $\mathbf{E}_e(\nu)$ is the single-electron field emitted from an electron at the bunch center at frequency ν. The radiated total intensity is proportional to the square of the absolute value of the total electric field

$$
\begin{aligned}
I_{\text{total}}(\nu) &\propto \left|\mathbf{E}_{\text{total}}(\nu)\right|^2 \\
&\approx \left|\sum_{j=1}^{N} \mathbf{E}_e(\nu)e^{2\pi i(\nu/c)\hat{\mathbf{n}}\cdot\mathbf{r}_j}\right|^2
\end{aligned}
$$

---

[1]In this thesis, the notation $\hat{\mathbf{a}}$ is used to represent a unit vector, i.e., $|\hat{\mathbf{a}}| = 1$.

$$= \sum_{j=1}^{N} E_{\mathrm e}(\nu)e^{2\pi i(\nu/c)\hat{\mathbf{n}}\cdot\mathbf{r}_j} \sum_{k=1}^{N} E_{\mathrm e}^{*}(\nu)e^{-2\pi i(\nu/c)\hat{\mathbf{n}}\cdot\mathbf{r}_k}$$

$$= \sum_{j=1}^{N} |E_{\mathrm e}(\nu)|^2 + \sum_{\substack{j,k=1 \\ j\neq k}}^{N} |E_{\mathrm e}(\nu)|^2 \, e^{2\pi i(\nu/c)(\mathbf{r}_j-\mathbf{r}_k)\cdot\hat{\mathbf{n}}}. \qquad (1.3)$$

If we denote $I_{\mathrm e}(\nu)$ as the single-electron intensity emitted at frequency ν with the relation $I_{\mathrm e}(\nu) \propto |E_{\mathrm e}(\nu)|^2$, then the total intensity becomes

$$I_{\mathrm{total}}(\nu) = \sum_{j=1}^{N} I_{\mathrm e}(\nu) + \sum_{\substack{j,k=1 \\ j\neq k}}^{N} I_{\mathrm e}(\nu)e^{2\pi i(\nu/c)(\mathbf{r}_j-\mathbf{r}_k)\cdot\hat{\mathbf{n}}}. \qquad (1.4)$$

This can be separated into the incoherent contribution

$$\begin{aligned} I_{\mathrm{inc}}(\nu) &= \sum_{j=1}^{N} I_{\mathrm e}(\nu) \\ &= N I_{\mathrm e}(\nu) \end{aligned} \qquad (1.5)$$

and the coherent one

$$\begin{aligned} I_{\mathrm{coh}}(\nu) &= \sum_{\substack{j,k=1 \\ j\neq k}}^{N} I_{\mathrm e}(\nu)e^{2\pi i(\nu/c)(\mathbf{r}_j-\mathbf{r}_k)\cdot\hat{\mathbf{n}}} \\ &= I_{\mathrm e}(\nu) \sum_{\substack{j,k=1 \\ j\neq k}}^{N} e^{2\pi i(\nu/c)(\mathbf{r}_j-\mathbf{r}_k)\cdot\hat{\mathbf{n}}}. \end{aligned} \qquad (1.6)$$

Since there is typically a very large number of electrons (say, 10^8 or larger) distributed in a typically small volume in space (say, $1\,\mathrm{mm}^3$ or smaller), a continuous probability function can be used to approximate the electron distribution in the bunch. Let us assume that the number of electrons in the volume element $\mathrm{d}^3 r$ centered at the position vector $\mathbf{r}$ originating from the bunch center is $NS(\mathbf{r})\mathrm{d}^3 r$, where $S(\mathbf{r})$ is the probability of finding electrons at $\mathbf{r}$ satisfying

$$\int S(\mathbf{r})\,\mathrm{d}^3 r = 1. \qquad (1.7)$$

Therefore, the discrete summation in Eq. (1.6) can be approximated by an integral

$$
\begin{aligned}
I_{\text{coh}}(\nu) &\approx I_e(\nu)N(N-1)\int d^3r \int d^3r'\, e^{2\pi i(\nu/c)(\mathbf{r}-\mathbf{r}')\cdot\hat{\mathbf{n}}}S(\mathbf{r})S(\mathbf{r}') \\
&= I_e(\nu)N(N-1)\left|\int d^3r\, e^{2\pi i(\nu/c)\mathbf{r}\cdot\hat{\mathbf{n}}}S(\mathbf{r})\right|^2 \\
&\equiv I_e(\nu)N(N-1)f(\nu;\hat{\mathbf{n}}),
\end{aligned}
\tag{1.8}
$$

where the bunch form factor $f(\nu;\hat{\mathbf{n}})$ is defined as[2]

$$
f(\nu;\hat{\mathbf{n}}) = \left|\int d^3r\, e^{2\pi i(\nu/c)\mathbf{r}\cdot\hat{\mathbf{n}}}S(\mathbf{r})\right|^2.
\tag{1.9}
$$

Hence, the total intensity detected at the observation point emitted from an electron bunch is expressed as the sum of coherent and incoherent contribution

$$
\begin{aligned}
I_{\text{total}}(\nu) &= I_{\text{inc}}(\nu) + I_{\text{coh}}(\nu) \\
&= I_e(\nu)\,N[1 + (N-1)f(\nu;\hat{\mathbf{n}})].
\end{aligned}
\tag{1.10}
$$

The incoherent contribution $I_{\text{inc}}(\nu)$ is only proportional to the number of electrons in the bunch, N, while the coherent contribution $I_{\text{coh}}(\nu)$ is proportional to N^2. The later contribution can be N times larger than the former one at frequencies where the form factor $f(\nu;\hat{\mathbf{n}})$ is close to unity.

1.1.2   The Bunch Form Factor

At this point, it is worth examining the form factor $f(\nu;\hat{\mathbf{n}})$ closely. It is easy to show that $0 \leq f(\nu;\hat{\mathbf{n}}) \leq 1$ for all frequencies. In the low frequency (long wavelength) limit, where $\nu \to 0$ ($\lambda = c/\nu \to \infty$), the form factor $f(\nu;\hat{\mathbf{n}})$ approaches unity. Therefore, the total intensity $I_{\text{total}}(\nu)$ is dominated by the coherent part $I_{\text{coh}}(\nu)$ and, hence, is proportional to N^2. On the other hand, in the high frequency (short wavelength)

---

[2]Although the form factor can be expressed as a two-variable function, i.e., $f(\nu,\hat{\mathbf{n}})$, we rather treat $\hat{\mathbf{n}}$ as a parameter here (separated by a semi-colon) than a variable (separated by a comma) because in most experiments the observation points are fixed, so are the corresponding $\hat{\mathbf{n}}$'s.

limit, where $\nu \to \infty$ ($\lambda \to 0$), the bunch form factor $f(\nu; \hat{n})$ vanishes. Thus, $I_{\text{total}}(\nu)$ is dominated by the incoherent contribution $I_{\text{inc}}(\nu)$ and is only proportional to N. In between, the intensity $I_{\text{total}}(\nu)$ is determined by the Fourier transform of the three-dimensional bunch distribution.

In order to simplify the bunch from factor, let us choose the following Cartesian coordinate system with the origin at the bunch center, $\hat{n}$ in the xz plane, the direction of electron-beam propagation as $\hat{z}$, the direction of $(\hat{z} \times \hat{n}) \times \hat{z}$ as $\hat{x}$, and the direction of $\hat{z} \times \hat{n}$ as $\hat{y}$. Hence, the vectors $\hat{n}$ and $\mathbf{r}$ can be expressed as[3]

$$\hat{n} = \sin\theta\,\hat{x} + \cos\theta\,\hat{z} \tag{1.11}$$

$$\mathbf{r} = x\,\hat{x} + y\,\hat{y} + z\,\hat{z}, \tag{1.12}$$

where θ is the angle between $\hat{n}$ and $\hat{z}$. Let us also assume that the transverse bunch distribution and the longitudinal one are separable, i.e.,

$$S(\mathbf{r}) = S(x, y, z) \equiv g(x, y)h(z). \tag{1.13}$$

The form factor in Eq. (1.9) can then be written as

$$
\begin{aligned}
f(\nu; \theta) &= \left| \int d^3r\, e^{2\pi i(\nu/c)\mathbf{r}\cdot\hat{n}} S(\mathbf{r}) \right|^2_{\hat{n}\cdot\hat{z}=\cos\theta} \\
&= \left| \int_{-\infty}^{+\infty} dy \int_{-\infty}^{+\infty} dx\, g(x,y) e^{2\pi i(\nu/c)x\sin\theta} \int_{-\infty}^{+\infty} dz\, h(z) e^{2\pi i(\nu/c)z\cos\theta} \right|^2.
\end{aligned} \tag{1.14}
$$

---

[3]As a consequence of this definition, the coordinate system changes with the orientation of $\hat{n}$, which is fine here since the following discussions do not depend on the choice of $\hat{n}$. However, this definition may not be desirable in situations that there is a preferable coordinate system other than this one. Under such restriction, one can define $\hat{n}$ and $\mathbf{r}$ with respect to the preferable system as

$$\hat{n} = \sin\theta\cos\psi\,\hat{x} + \sin\theta\sin\psi\,\hat{y} + \cos\theta\,\hat{z}$$
$$\mathbf{r} = x\,\hat{x} + y\,\hat{y} + z\,\hat{z},$$

where θ is the angle between $\hat{n}$ and $\hat{z}$ (i.e., $\cos\theta = \hat{n}\cdot\hat{z}$), and ψ is the angle between $\hat{x}$ and the projection of $\hat{n}$ on the xy plane [i.e., $\cos\psi = (\hat{n} - \cos\theta\,\hat{z})\cdot\hat{x}/\sin\theta = \hat{n}\cdot\hat{x}/\sin\theta$].

1.1.2.1 On-Axis Observation

The bunch form factor will have the simplest expression if the bunch has azimuthal symmetry about the direction of electron-beam propagation $\hat{z}$, and the observation point is chosen in this direction (i.e., $\theta = 0$; on-axis observation). Under these assumptions, the contribution from the transverse bunch distribution $g(x, y)$ becomes unity for all frequencies because $\int_{-\infty}^{+\infty} dx \int_{-\infty}^{+\infty} dy\, g(x, y) = 1$, and the form factor is only determined by the Fourier transform of the longitudinal bunch distribution $h(z)$. Hence, we have

$$f(\nu; \theta = 0) = \left| \int dz\, e^{2\pi i (\nu/c) z} h(z) \right|^2 . \tag{1.15}$$

For example, if the bunch is symmetric about $\hat{z}$ with rectangular longitudinal distribution of length $2\sigma_z$, i.e.,

$$h(z) = \begin{cases} 1/(2\sigma_z) & \text{for } |z| \leq \sigma_z \\ 0 & \text{otherwise} \end{cases} , \tag{1.16}$$

then the corresponding form factor, from Eq. (1.15), is

$$f(\nu; \theta = 0) = \left[\frac{\sin(2\pi\nu\sigma_z/c)}{2\pi\nu\sigma_z/c} \right]^2 . \tag{1.17}$$

As another example, for a similar bunch with Gaussian longitudinal distribution of equivalent length $\sqrt{2\pi}\, \sigma_z$, that is,[4]

$$h(z) = \frac{1}{\sqrt{2\pi}\, \sigma_z}\, e^{-z^2/2\sigma_z^2}, \tag{1.18}$$

---

[4]The equivalent width of a one-dimensional distribution function $f(x)$ is defined as the width of an "equivalent" rectangular distribution which has the same height as the maximum of $f(x)$, i.e.,

$$w_{\text{eq}} \equiv \frac{\int_{-\infty}^{+\infty} f(x)dx}{\displaystyle\max_{x \in (-\infty, +\infty)} f(x)}.$$

If $f(x)$ is a normalized bunch distribution, i.e., $\int_{-\infty}^{+\infty} f(x)dx = 1$, then we have $w_{\text{eq}} = [\max_{x \in (-\infty, +\infty)} f(x)]^{-1}$. For a higher-dimensional distribution function, the equivalent width can be defined in a similar way.

the form factor is also Gaussian

$$f(\nu; \theta = 0) = e^{-(2\pi\nu\sigma_z/c)^2}. \tag{1.19}$$

1.1.2.2 Off-Axis Observation

As indicated by Eq. (1.14), the form factor will no longer remain its simplest form as shown in Eq. (1.15) when the observation point is chosen off-axis, i.e., $\theta = \cos^{-1}(\hat{n} \cdot \hat{z}) \neq 0$. The transverse bunch distribution will contribute to the form factor even for an azimuthally symmetric bunch. Furthermore, the longitudinal distribution will have less effect on the form factor at larger angles θ due to the decrease in effective longitudinal length $\sigma_z \sin \theta$. If the bunch has azimuthal symmetry, the form factor can sometimes be simplified through the choice of a cylindrical coordinate system. Assuming that (ρ, ϕ) is the polar coordinate system defined on the xy plane with $x = \rho \cos \phi$ and $y = \rho \sin \phi$, then the transverse contribution in Eq. (1.14) can be expressed as a Bessel transform

$$\left| \int_{-\infty}^{+\infty} dy \int_{-\infty}^{+\infty} dx \, g(x,y) e^{2\pi i(\nu/c)x\sin\theta} \right|^2$$
$$= \left| \int_0^{2\pi} d\phi \int_0^{+\infty} \rho d\rho \, g(\rho) e^{2\pi i(\nu/c)\rho\cos\phi\sin\theta} \right|^2$$
$$= 4\pi^2 \left[\int_0^{+\infty} g(\rho) J_0(2\pi\nu\rho\sin\theta/c)\rho d\rho \right]^2, \tag{1.20}$$

where J_0 is the zeroth order Bessel function. Two facts also have been used in the derivation: the transverse bunch distribution g is only a function of ρ [i.e., $g(x,y) = g(\rho)$], and the identity $2\pi J_0(u) = \int_0^{2\pi} e^{iu\cos\phi}d\phi$. In the case of a cylindrical bunch distribution of length $2\sigma_z$ and radius σ_ρ with the transverse distribution defined by

$$g(\rho) = \begin{cases} 1/(\pi\sigma_\rho^2) & \text{for } 0 \leq \rho \leq \sigma_\rho \\ 0 & \text{otherwise} \end{cases} \tag{1.21}$$

and the longitudinal one by Eq. (1.16), the bunch form factor at frequency ν and observation angle θ is

$$f(\nu;\theta) = \left[\frac{2J_1(2\pi\nu\sigma_\rho\sin\theta/c)}{2\pi\nu\sigma_\rho\sin\theta/c}\frac{\sin(2\pi\nu\sigma_z\cos\theta/c)}{2\pi\nu\sigma_z\cos\theta/c}\right]^2 , \qquad (1.22)$$

where J_1 is the first order Bessel function. On the other hand, for a Gaussian bunch distribution of equivalent length $\sqrt{2\pi}\,\sigma_z$ and equivalent diameter $\sqrt{2\pi}\,\sigma_\rho$ with

$$g(x,y) = \frac{1}{\sqrt{2\pi}\,\sigma_\rho}\,e^{-(x^2+y^2)/2\sigma_\rho^2} \qquad (1.23)$$

as the transverse distribution and Eq. (1.18) as the longitudinal one, after carrying out the integrations in the Cartesian coordinate system, the form factor becomes

$$f(\nu;\theta) = e^{-(2\pi\nu\sigma_\rho\sin\theta/c)^2}\,e^{-(2\pi\nu\sigma_z\cos\theta/c)^2}. \qquad (1.24)$$

The "apparent" equivalent length when observed at angle θ becomes $\sqrt{2\pi}\,(\sigma_z\cos\theta + \sigma_\rho\sin\theta)$ in an analogy to Eq. (1.18).

1.1.3 The Form Factor and the Degree of Coherence

It is interesting to point out that the form factor $f(\nu;\theta)$ is indeed related to the spectral degree of coherence of the emitted radiation at frequency ν and observation angle θ. From the coherence theory in optics, the complex degree of coherence for an extended light source can be expressed in the form of diffraction calculation through the van Citter-Zernike theorem[3]. When the electron bunch radiates, the radiation is actually emitted from this three-dimensional extended source; in addition, the derivation of the bunch form factor as shown in Eq. (1.9) is equivalent to the calculation of diffraction effect for a three-dimensional weighted "aperture". Hence, the form factor represents the spectral degree of coherence of the three-dimensional extended light source, which is the emitting electron bunch. Through the following discussion, it

will become clear how this form factor is related to the spectral degrees of temporal and spatial coherence.

In the case of on-axis observation, the form factor $f(\nu; \theta = 0)$ is indeed the spectral degree of temporal coherence of the emitted radiation at frequency ν. For frequencies whose corresponding wavelengths are much longer than the bunch length, the form factor is near unity, and the radiation is temporally coherent (the degree of coherence approaches unity). However, for frequencies with wavelengths much shorter than the bunch length, the form factor approaches zero, and the radiation is temporally incoherent (the degree of coherence approaches zero). The degree of temporal coherence at different frequencies is determined by the longitudinal (or equivalently, temporal) distribution of the bunch.

On the other hand, the transverse contribution of the form factor for an off-axis observation as shown in Eq. (1.20) is indeed the spectral degree of spatial coherence of the emitted radiation at frequency ν and observation angle θ. To simplify the discussion, let us assume that the bunch length is much shorter than the transverse beam size (i.e., $\sigma_z \ll \sigma_\rho$ or $\sigma_z/\sigma_\rho \to 0$), so the variation of the form factor is determined by the transverse contribution. For frequencies with corresponding wavelengths much longer than the effective transverse bunch size (e.g., $\sigma_\rho \sin \theta$), the form factor is near unity, and the radiation is spatially coherent. However, for frequencies with shorter wavelengths than the effective bunch size, the form factor approaches zero, and the radiation is spatially incoherent. The degree of spatial coherence at different frequencies and observation angles is determined by the transverse distribution of the bunch. Therefore, it can be concluded that the bunch form factor as expressed in Eq. (1.9) is the spectral degree of "three-dimensional" (temporal and spatial) coherence of the emitted radiation from the three-dimensional electron bunch.

1.1.4 An Example: Coherent Synchrotron Radiation

From the theory of coherent radiation stated above, we know that both coherent and incoherent radiation is emitted for any electron bunch length. However, in existing storage rings, only the incoherent part of synchrotron radiation has been observed; in contrast, none of the coherent part of the radiation has been detected because it is suppressed by the surrounding metallic vacuum chamber which dimension happened to be comparable to or smaller than the electron bunch length. However, if the bunch length can be reduced to values shorter than the vacuum chamber dimension, coherent synchrotron radiation should be observable. To demonstrate this, let us look at an example of coherent synchrotron radiation with the shielding effect of the metallic surroundings[4].

1.1.4.1 Method of Calculation

In order to calculate the radiated spectrum of coherent synchrotron radiation with the shielding effect of the metallic beam pipe, it is necessary to start with an expression for single-electron synchrotron radiation with such effect [i.e., a suitable $I_e(\nu)$ for Eq. (1.10)]. Although expressions for synchrotron radiation emitted by an electron in free space can be found in many references, they do not include the shielding effect from the metallic boundary. However, Nodvick and Saxon gave an expression for synchrotron radiation which has included this effect and is used in the following calculation[2]. Let us assume that if an electron of velocity v follows a circular orbit of radius ρ in the mid-plane of two infinite parallel metallic plates separated by a distance a, then the total emitted synchrotron radiation power in the frequency interval from $n\nu_0$ to $(n+1)\nu_0$ is found to be[5][2, Eq. (A1)]

$$P_e(\nu) = \left(\frac{8\pi^2\nu e^2}{a}\right) \sum_{j=1,3,5,\ldots}^{j<na\beta/\pi\rho} \left[\beta^2 {J_n'}^2(\gamma_{nj}\rho) + \frac{(j\pi\rho/a)^2}{\gamma_{nj}^2\rho^2} J_n^2(\gamma_{nj}\rho)\right], \qquad (1.25)$$

---

[5]In this thesis, we will assume the CGS system as the default unit system.

where $J_n(x)$ and $J'_n(x)$ are the nth order Bessel function and its derivative, ν_0 is the revolution frequency of the circular motion with $\nu_0 = v/2\pi\rho$, n is the largest integer satisfying $n\nu_0 \leq \nu$, $\beta \equiv v/c$ with c the speed of light, and

$$\gamma_{nj}\rho = \sqrt{(n\beta)^2 - (j\pi\rho/a)^2} \ . \tag{1.26}$$

Since the orders of Bessel functions involved in the caculation are typically large numbers ($n \sim \rho\nu/c$, typically thousands or larger), it is important to calculate $J_n(x)$ and $J'_n(x)$ of large integral orders in an efficient way. The standard backward recursive method becomes impractical because of the large numbers of recursive substitutions and the machine underflow problem at large integral orders. Fortunately, the uniform asymptotic expansions of Bessel functions provide powerful and efficient solutions for this problem[5]:

$$J_n(nz) = \left(\frac{4\zeta}{1-z^2}\right)^{1/4}\left[\frac{\text{Ai}(n^{2/3}\zeta)}{n^{1/3}}\sum_{k=0}^{\infty}\frac{a_k(\zeta)}{n^{2k}} + \frac{\text{Ai}'(n^{2/3}\zeta)}{n^{5/3}}\sum_{k=0}^{\infty}\frac{b_k(\zeta)}{n^{2k}}\right] \tag{1.27}$$

$$J'_n(nz) = \frac{2}{z}\left(\frac{1-z^2}{4\zeta}\right)^{1/4}\left[\frac{\text{Ai}(n^{2/3}\zeta)}{n^{4/3}}\sum_{k=0}^{\infty}\frac{c_k(\zeta)}{n^{2k}} + \frac{\text{Ai}'(n^{2/3}\zeta)}{n^{2/3}}\sum_{k=0}^{\infty}\frac{d_k(\zeta)}{n^{2k}}\right], \tag{1.28}$$

where ζ satisfies

$$\frac{2}{3}\zeta^{3/2} = \ln\frac{1+\sqrt{1-z^2}}{z} - \sqrt{1-z^2} \quad \text{for } |z| < 1, \tag{1.29}$$

and $\text{Ai}(x)$ and $\text{Ai}'(x)$ are Airy functions. Some of the coefficients $a_k(\zeta)$, $b_k(\zeta)$, $c_k(\zeta)$, and $d_k(\zeta)$ are listed below and others can be found in Ref. [5]:

$$a_0 = 1,$$

$$a_1 = \frac{1}{1152}\left[(81t^2 - 462t^4 + 385t^6) - \frac{7}{\zeta^{3/2}}(3t - 5t^3) - \frac{455}{4\zeta^3}\right],$$

$$b_0 = \frac{1}{48}\left[\frac{-2}{\zeta^{1/2}}(3t - 5t^3) - \frac{5}{\zeta^2}\right],$$

$$c_0 = \frac{1}{48}\left[-2\zeta^{1/2}(-9t + 7t^3) + \frac{7}{\zeta}\right],$$

Table 1.1: Basic conditions for coherent synchrotron radiation calculations. The bunch length 2σ is defined in Eq. (1.16) for the rectangular distribution and in Eq. (1.18) for the Gaussian one.

Parameter	Notation	Value
Bunch length	$2\sigma_z$	$30\,\mu$m $(0.1\,$ps$)$
Electrons per bunch	N	10^9
Electron energy	$\mathcal{E}$	$40\,$MeV
Magnetic field	B	$1.9\,$kG

$$d_0 = 1,$$
$$d_1 = \frac{1}{1152}\left[(-135t^2 + 594t^4 - 455t^6) + \frac{5}{\zeta^{3/2}}(-9t + 7t^3) + \frac{385}{4\zeta^3}\right],$$

where $t \equiv (1 - z^2)^{-1/2}$.

The total radiated coherent synchrotron power at frequency ν from an electron bunch is calculated using the conditions listed in Table 1.1, Eqs. (1.10), (1.25), and the relations

$$P_e(\nu) \propto I_e(\nu)$$

$$\mathcal{E} = \frac{mc^2}{\sqrt{1 - \beta^2}} \equiv \gamma mc^2$$

$$\rho = \frac{\beta \mathcal{E}}{eB} \approx \frac{\beta \times \mathcal{E}[\text{MeV}]}{29.98 \times B[\text{kG}]}\ [\text{m}],$$

where e is the electronic charge, m is the electronic mass, γ is the Lorentz factor, and the units of the quantities are listed in the associated square brackets[6]. In the results, the calculated power is normalized to that emitted from a single electron bunch in each pass and is converted to spectral photon flux (in photons/sec/100% Bandwidth) using the following relation

$$\frac{\mathrm{d}F(\nu)}{\mathrm{d}\nu/\nu} = \frac{P_{\text{total}}(\nu)}{h\nu_0},$$

where $F(\nu)$ is the photon flux (in photons/sec) at frequency ν, and h is Planck's constant. To emphasize the contribution from the longitudinal bunch distribution,
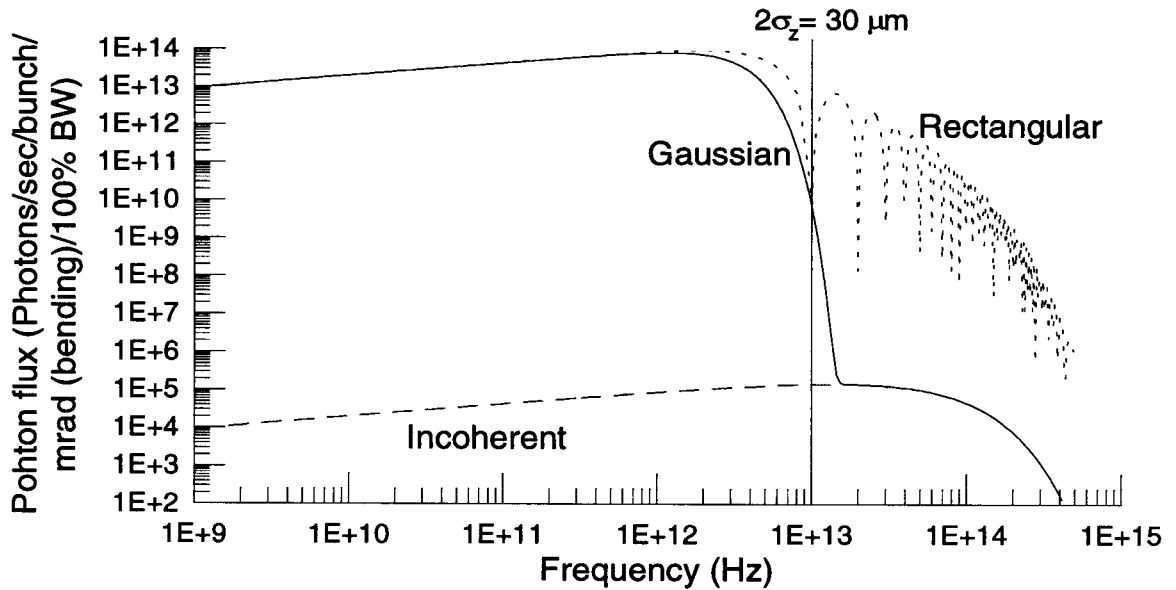
Figure 1.1: Coherent synchrotron radiation emitted from rectangular (dotted) and Gaussian (solid line) bunches without the shielding effect from the metallic beam pipe. The vertical line indicates the bunch length $2\sigma_z$ set in the calculations. The spectrum for the incoherent contribution is also shown as the dashed line.

on-axis observation of the cylindrically symmetric electron beam is assumed in these calculations.

1.1.4.2 Results

The calculated spectral photon flux emitted from rectangular and Gaussian bunches without the shielding effect from the metallic beam pipe is shown in Fig. 1.1. For wavelengths longer than the bunch length (coherent part), the radiated spectra for both distributions are coherent. However, for wavelengths shorter than the bunch length (incoherent part), the spectra change from coherent to incoherent, and the rate of change is determined by the Fourier transform of the bunch distribution. The Gaussian bunch has steeper change between the coherent and incoherent part, while the rectangular bunch has more high frequency lobes extending from the coherent
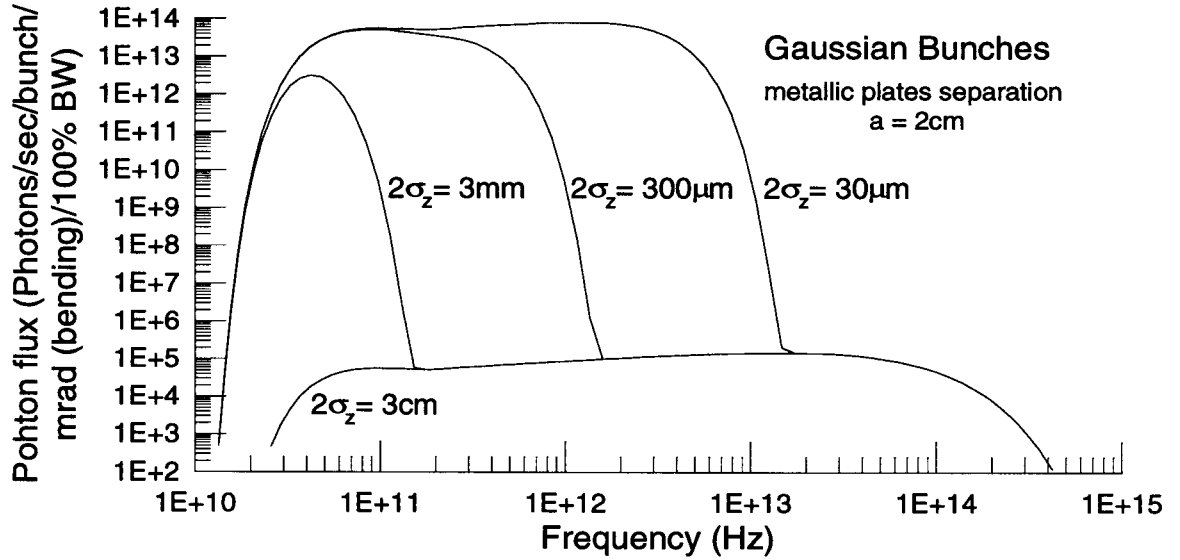
Figure 1.2: Coherent synchrotron radiation emitted from Gaussian bunches of different lengths with the shielding effect due to the metallic beam pipe.

part into the incoherent one. The ratio of the coherent contribution to the incoherent one in the coherent part is proportional to the number of electrons in the bunch (i.e., 10^9 in this example).

To demonstrate the shielding effect of the metallic beam pipe, the calculated spectra for Gaussian bunches of different lengths for a pipe size of $a = 2\,\mathrm{cm}$ are shown in Fig. 1.2. All radiation with wavelengths longer than the vacuum pipe dimension is suppressed by the shielding effect of the vacuum chamber. When the bunch length is longer than the vacuum pipe dimension, the coherent contribution is shielded by the vacuum chamber, and the whole spectrum is identical to that of the incoherent contribution at wavelengths shorter than the pipe dimension. This is what would be expected in existing storage rings. As the bunch length is reduced, the coherent radiation begins to show up at wavelengths shorter than the pipe dimension. Therefore, to observe coherent radiation emitted from an electron bunch, it is necessary to make the bunch length shorter than the beam pipe dimension.
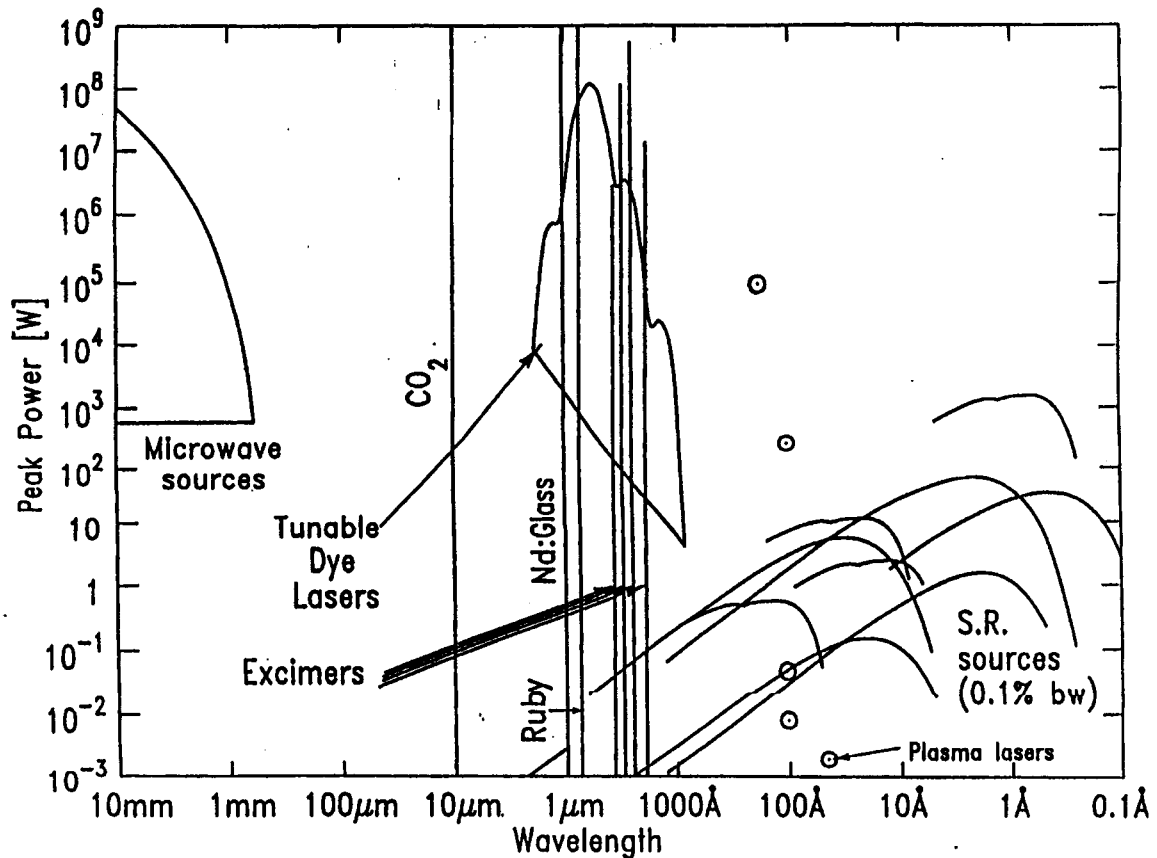
Figure 1.3: Existing typical high-power light sources in different spectral regimes. The data for plasma lasers are shown as ⊙. Newly developed free-electron lasers in the far-infrared regime listed in Table 1.2 are not shown here.

The high intensity of coherent synchrotron radiation emitted from subpicosecond electron bunches as demonstrated above shows a new and promising direction in the development of high-power, far-infrared light source. As a reference, the existing high-power light sources such as lasers and synchrotron radiation sources in different spectral regimes are shown in Fig. 1.3[7]. Lasers, synchrotron radiation sources, and microwave sources have covered most part of the spectrum from microwaves to hard x-rays. What are not shown in the figure are newly developed free-electron lasers in the far-infrared regime, which are listed in Table 1.2. Although these free-electron

Table 1.2: Peak power of newly developed free-electron lasers in the far-infrared regime. Data source: the FEL Virtual Library at the World Wide Web URL http://sbfel3.ucsb.edu/www/vl_fel.html.

Free-electron laser	Wavelength tuning range	Peak power
UCSB mm-FEL[8]	338 μm–2.5 mm	1–15 kW
UCSB μm-FEL[8]	63–338 μm	1–6 kW
Stanford Firefly[9]	15–65 μm	100–500 kW
Stanford STI[9]	3–15 μm	0.67–2.86 MW
CLIO FEL[10]	3–40 μm	a few MW (100 MW max)
FELIX Infrared FEL[11]	5–110 μm	20 MW max

lasers have wide wavelength tuning ranges, they are narrowband in nature. Therefore, from millimeter waves to far-infrared light (wavelength longer than 10 μm) there is basically no high-power *broadband* light source available. The calculated spectral peak power of coherent synchrotron radiation from the 0.1-ps electron bunch described in Table 1.1 is shown in Fig. 1.4. The spectral power from a 2000 K blackbody radiator is also shown in the figure for comparison, which is expressed as the power emitted from unit area in unit bandwidth[12, Sec. 13.2]

$$\frac{\mathrm{d}^2 P}{\mathrm{d}A(\mathrm{d}\nu/\nu)} = \frac{2\pi h\nu^4}{c^2} \frac{1}{e^{h\nu/kT} - 1},\qquad(1.30)$$

where k is the Boltzmann constant, and T is the absolute temperature of the radiator. The peak power of coherent synchrotron radiation is at least 6 orders of magnitude higher than that of blackbody radiation in the far-infrared regime. When compared to other high-power light sources in Fig. 1.3, coherent synchrotron radiation is located at about the middle of the vertical range and basically fills the gap (cf., the curve for the rectangular bunch distribution in Fig. 1.4) between microwave sources and CO_2 lasers. If one calculates the simple-minded "peak" power from the ratio of the total radiation energy (cf., Fig. 1.4) to bunch duration (0.1 ps), this would give a peak power of 1.74 MW/mrad for the Gaussian bunch distribution and 3.50 MW/mrad for the rectangular one! Hence, coherent synchrotron radiation, in this example, shows

Wavelength

10 mm   1 mm   100 μm   10 μm   1 μm

Coherent synchrotron radiation

Rectangular

Gaussian

T = 2000 K
Black body radiation

Coherent synchrotron radiation peak power (W/mrad bending)

Black body radiation power (W/cm²)

Frequency (Hz)
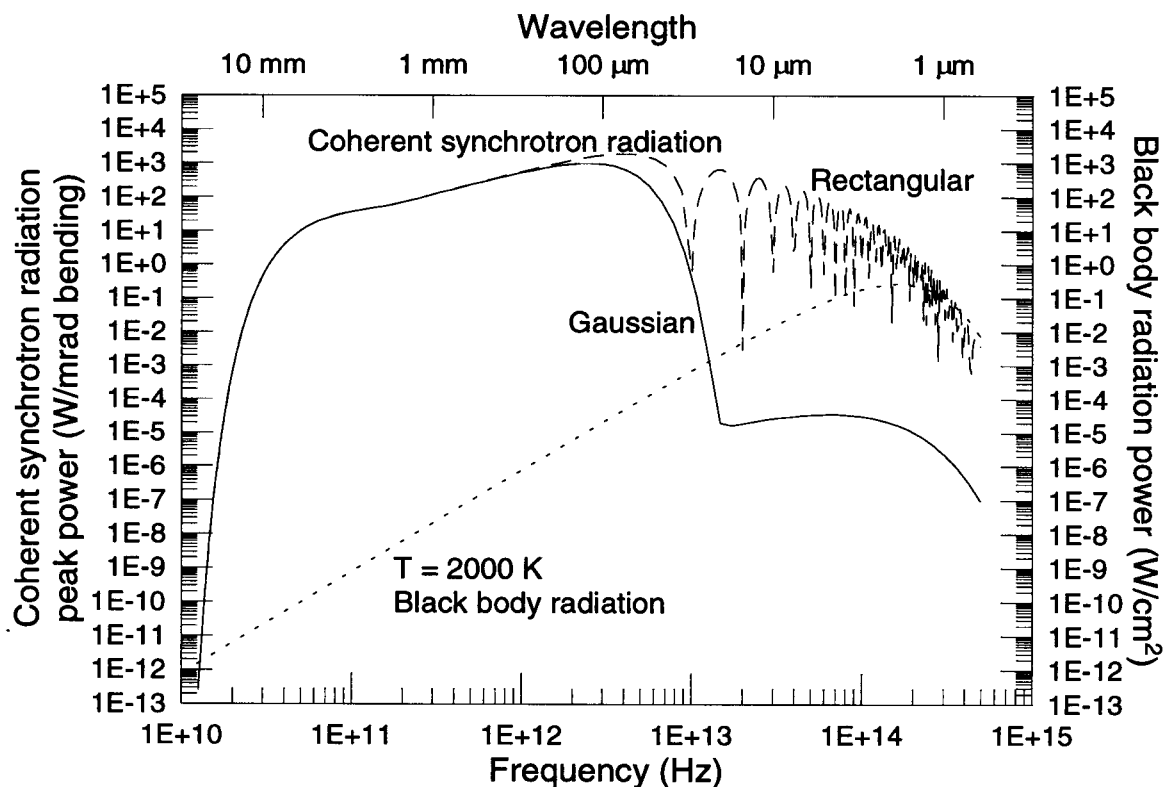
Figure 1.4: Calculated spectral peak power of coherent synchrotron radiation and black body radiation in 0.1% bandwidth. The peak power of coherent synchrotron radiation is normalized to the bending angle [in W/mrad (bending)], while the power of blackbody radiation is normalized to the radiating area (in W/cm²). The total energy radiated from one Gaussian electron bunch is 0.174 μJ/mrad (bending) and form the rectangular one, 0.350 μJ/mrad (bending).

an excellent candidacy as a simple, high-power, broadband, far-infrared light source.

1.2   The Stanford SUNSHINE Facility

In order to study the production of high-intensity, coherent, far-infrared radiation through different radiating processes form subpicosecond electron bunches and the

Table 1.3: Typical SUNSHINE operating conditions. The electron bunch length will be determined in the second chapter.

RF parameters		*Electron parameters*	
RF frequency	2856 MHz	Bunch length	< 1 ps
Repetition rate	10 pulses/sec	Electrons per bunch	10^8–10^9
Pulse duration	$\sim 1\,\mu$s	Electron energy	30 MeV
Bunches per RF pulse	~ 3000	Bunch spacing	350 ps (10.5 cm)

physics of subpicosecond electron beam, an electron facility named SUNSHINE (Stanford UNiversity SHort INtense Electron source) has been designed and built on campus of Stanford University since 1991[13]. With a specially designed electron gun[14] and a matched magnetic compressor, SUNSHINE is capable of producing subpicosecond electron bunch train[15]. The typical operating conditions of SUNSHINE are listed in Table 1.3. At a repetition rate of 10 Hz, SUNSHINE produces 1-μs-long electron macro-pulses which contains around 3000 electron bunches with 10^8–10^9 electrons in each bunch. The bunches are separated by 10.5 cm (350 ps) distance and are accelerated up to 30 MeV. This thesis uses these electron bunches to explore a new way to produce high-intensity, broadband, far-infrared radiation. The detail of the production of subpicosecond electron bunches at SUNSHINE is elaborated in Ref. [15]. Only the principle of the bunch generation and compression system will be discussed here.

1.2.1   Bunch Generation and Compression System

The bunch generation and compression system used at SUNSHINE, as shown in Fig. 1.5, consists of two major components: a 1½-cell thermionic RF gun and an alpha magnet with energy filters[15–17]. The RF gun operating at 2856 MHz produces 2.5-MeV/c electron bunches in which the electrons are distributed along a thin line in the energy-time phase space with higher energy electrons located at earlier time and lower

Thermionic
dispenser
cathode

1-1/2 cell RF gun

RF input port

Alpha
magnet

Electrons

30 MeV Linear accelerator

Energy selectors
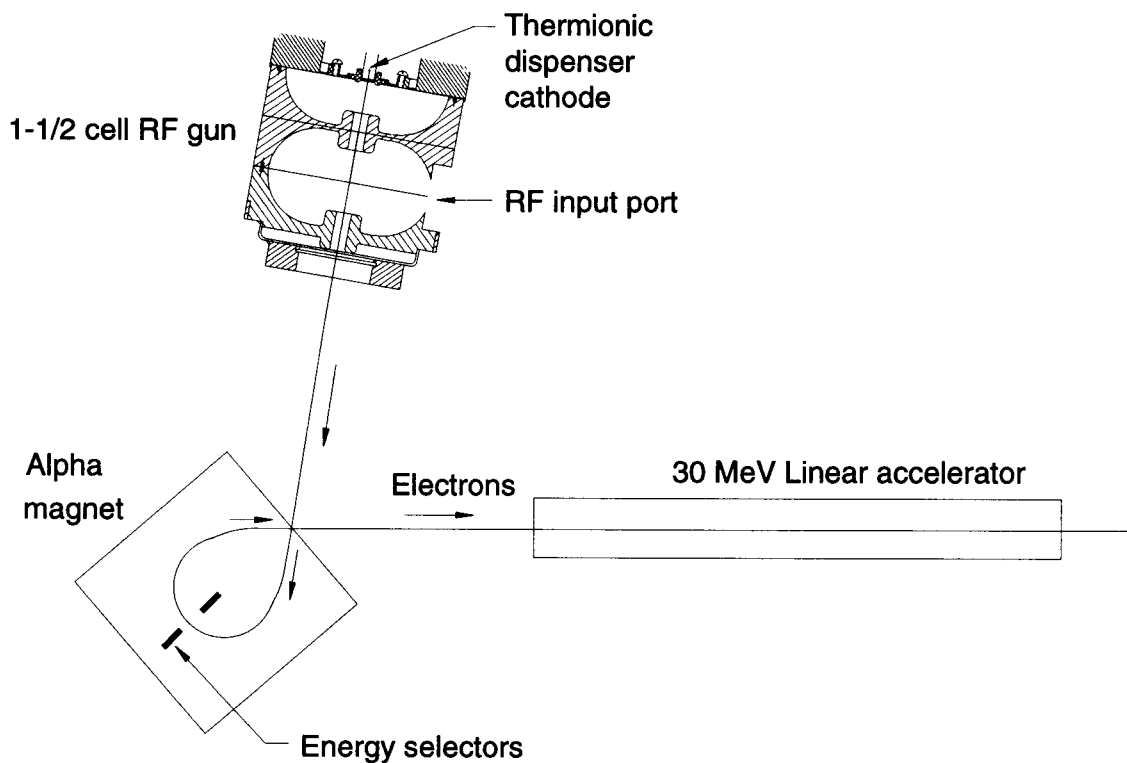
Figure 1.5: Schematic diagram of the bunch generation and compression system used at SUNSHINE.

energy electrons, later time. These energy-time correlated bunches are then steered into the alpha magnet for compression. The magnet will guide the electrons in the magnet along α-shaped paths with higher energy electrons following longer paths and lower energy electrons, shorter paths; hence, the earlier electrons in the bunch, which have higher energy, will spend more time in the magnet by following longer paths while the later electrons, less time. By correctly setting the magnet's strength, it is possible to compress part of the electron bunch into sub-picosecond duration. This optimally compressed part is then selected by energy filters located in the magnet and transported through a 30-MeV linear accelerator and a beam transport line to the radiation source point. When transporting the electron bunch, the velocity spread in the bunch can cause significant bunch lengthening (compared to the bunch length);
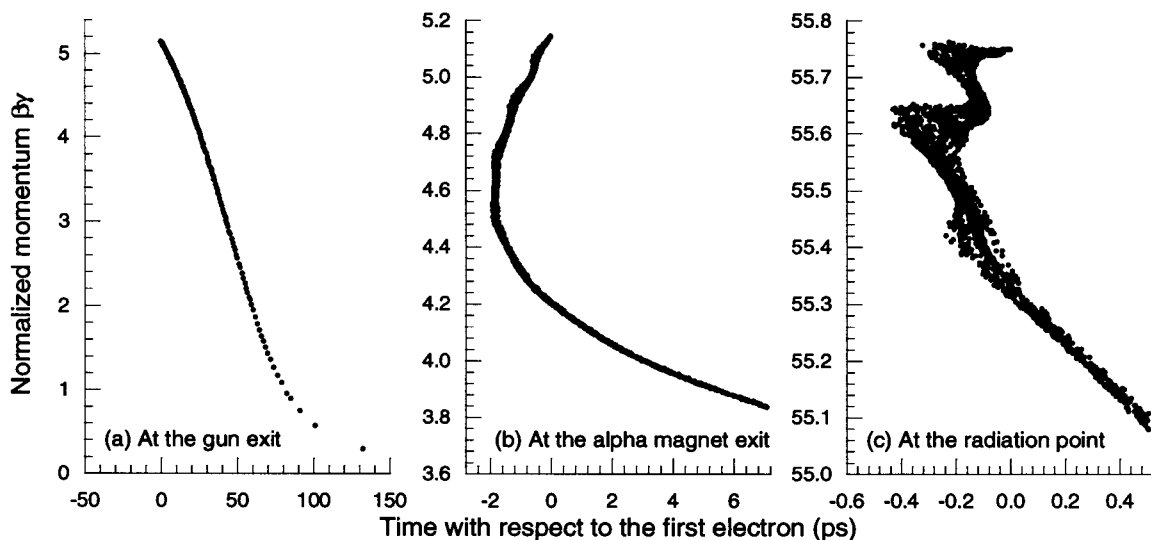
Figure 1.6: Principle of bunch compression at SUNSHINE. The electron energy-time distributions at (a) the exit of the gun, (b) the exit of α-magnet, and (c) radiation source point are shown.

therefore, it is necessary to compensate for this effect by overcompressing the bunch so that the minimum bunch length is reached at the source point.

This principle of bunch compression is demonstrated in Fig. 1.6[15]. At the exit of the gun, the electrons are distributed within a thin line in the energy-time phase space with a negative slope [cf., Fig. 1.6(a)]. Instead of compressing the bunch into the minimum bunch length right at the exit of the alpha magnet, an overcompression is applied to compensate for the bunch lengthening due to the velocity spread in the bunch when transporting it to the radiation source point. The overcompression will turn the line into a distribution of positive slope at the exit of the magnet as shown in Fig. 1.6(b). After transporting the beam farther downstream at the radiating source point, where the electrons radiate, part of the bunch (for example, $55.30 \lesssim \beta\gamma \lesssim 55.76$) reaches its minimum length ($\Delta t \approx 0.48\,\mathrm{ps}$) as an up-right distribution shown in Fig. 1.6(c). By adjusting the energy filters in the alpha magnet to allow only this part through the system, an electron bunch of subpicosecond duration can be

achieved.

1.2.2   The Detector for Coherent Radiation

To detect the far-infrared radiation emitted from subpicosecond electron bunches produced at SUNSHINE, a room-temperature bolometer is used because the radiation from the electron bunches is intense enough to produce a decent signal with a very good signal-to-noise ratio (typically, a few hundreds) [16–18]. This bolometer consists of a Molectron P1-65 LiTaO$_3$ pyroelectric detector of 5 mm diameter and a pre-amplifier. The detector's sensitivity is uniform over a spectral range from ultraviolet light to millimeter waves covering the full range of coherent radiation. The coherent far-infrared radiation is absorbed by the pyroelectric crystal in the detector, and produces a thermal expansion in the crystal. The expansion changes the intrinsic electric polarization and, thus, changes the electrical property of the crystal. This change is proportional to the rate of change of the incident radiation and is amplified by the following electronic circuits. The electronic bandwidth of the detector can be selected from 20 Hz up to 70 MHz by an appropriate external resistor. This bolometer's electronic bandwidth is set to around 20 Hz to measure the total radiated energy in each 1-μs-long macropulse with a responsivity of *pre-amplification* $\times$ 1.21 V/mJ, which has been calibrated against a Scientech thermopile power meter. By measuring the voltage signal of the bolometer, the radiated photon energy in each macropulse can be obtained. It is worth noticing that the measured bolometer signals shown in this thesis are normalized to a unit gain of pre-amplification. So the energy measured in the macro-pulse can be obtained simply from the ratio of the "quoted" bolometer signal to the unit-gain responsivity 1.21 V/mJ.

1.3 Observations of Coherent Synchrotron Radiation

The prediction of coherent synchrotron radiation came straight out of the theory when the appropriate phase contributions from electrons in the bunch are considered; however, the observation of this coherent radiation did not come directly out of experiments when people first tried to study it.

1.3.1 Previous Observations

Historically, storage rings became natural places for experiments to observe coherent synchrotron radiation because of the circular motion of the electron beams in these accelerators and the concern of electron energy loss through coherent emission of synchrotron radiation. Since the metallic vacuum pipes surrounding the electron beam suppresses any radiation of wavelengths longer than the pipe dimensions, all attempts to observe coherent synchrotron radiation from storage rings have failed because the electron bunch lengths were unfortunately longer than the vacuum pipe dimensions. Moreover, the Gaussian electron bunch distribution in storage rings made the observation of partially coherent radiation of wavelengths somewhat shorter than the bunch lengths impossible since the intensity drops down very quickly for wavelengths shorter than the bunch lengths (cf., Fig. 1.1). Only incoherent synchrotron radiation was observed and verified against theory. This unfortunate circumstance, however, brought a relief to these storage rings since the electrons only loose energy through incoherent synchrotron radiation.

On the other hand, the advance in accelerator technology makes it possible to produce electron bunch lengths of a few picoseconds (millimeters) long with "steep-edged" distributions which, like rectangular distribution, have slower-dropping "tail"
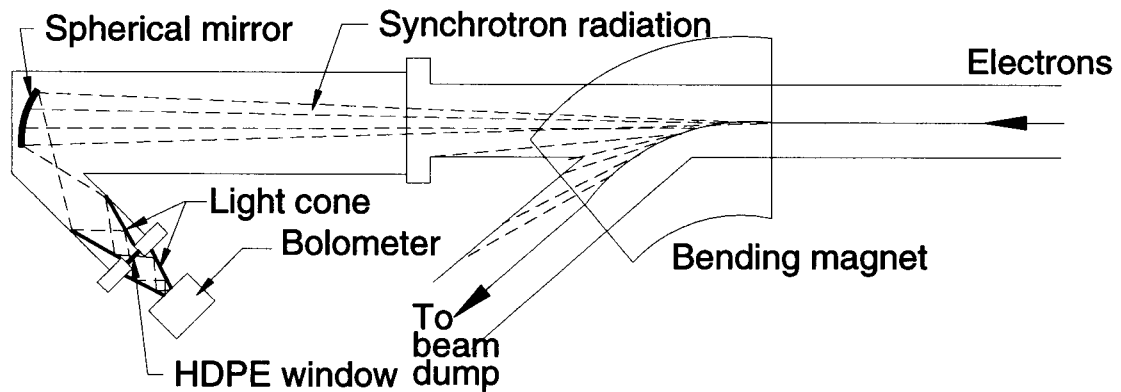
Figure 1.7: Schematic layout for the observation of coherent synchrotron radiation at SUNSHINE.

spectra at wavelengths shorter than the bunch lengths (cf., Fig. 1.1). Since the bunch lengths in linear accelerators are comparable to or shorter than the vacuum pipe dimensions, the observation of coherent synchrotron radiation becomes possible. In 1989, Nakazato *et al.* made the first observation of coherent synchrotron radiation from 2.5-mm-long (8.3-ps-long) bunches of 180-MeV electrons produced at the Tohoku Linac[19], and later in 1991 Blum *et al.* also observed coherent synchrotron radiation from 2-mm-long (6.7-ps-long) electron bunches of 300 MeV energy at the Cornell Linac[20]. Both experiments have observed coherent radiation in the millimeter-wavelength regime and confirmed the quadratic dependence of radiation intensity on electron charges in the bunch. However, no absolute measurement of intensity or energy for coherent synchrotron radiation was reported in either paper.

1.3.2 The Observation at SUNSHINE

Equipped with an advanced electron bunch generation and compression system, SUNSHINE is capable of producing subpicosecond electron bunches and intense coherent radiation from these bunches in the far-infrared regime. At SUNSHINE, coherent

synchrotron radiation is generated when 30-MeV electron bunches are deflected by a
2.2-kG dipole magnet shown in Fig. 1.7[16]. This coherent radiation is collected by
a 100-mm-diameter spherical mirror located 1.3 m away from the source point. The
angular acceptance for the radiation is limited to 40 mrad by the mirror diameter.
The radiation focused by the mirror is deflected into a copper condensing cone[21],
which then channels the radiation through a 1.25-mm-thick high-density polyethylene
(HDPE) window of 19 mm diameter into a room-temperature bolometer. Since the
diameter of the pyroelectric detector is only 5 mm, an additional copper condensing
cone is installed between the HDPE window and the bolometer to direct all radiation
through the window onto the detector surface.

1.3.2.1   Quadratic Dependence on the Electron Current

Theoretically, the coherent radiation intensity is expected to scale with the square of
the number of electrons in the bunch. To verify this, a good way to change the beam
current without affecting the bunch length is important and has to be investigated.
A direct way to reduce the beam current would be to use mechanical scrapers in
the beam line; unfortunately, they are not available at SUNSHINE. Changing the
cathode heating power in the RF gun would be a neutral way to vary the beam
current, but this also affects the momentum distribution of the electrons at the gun
exit because of the change of the beam loading in the gun. Since the bunch length
is determined by a combination of electron momentum distribution at the gun exit
and compression in the alpha magnet, the resulting bunch length is changed when
the cathode heating has changed. Therefore, the only practical way to vary the beam
intensity at SUNSHINE is to use the high energy filter in the alpha magnet to scrape
off the high-energy part of the beam while keeping the low energy filter fixed. Since
the alpha magnet strength is adjusted to compress most of the high-energy electrons
into a short bunch, this method seems to have the least effect on the bunch length.
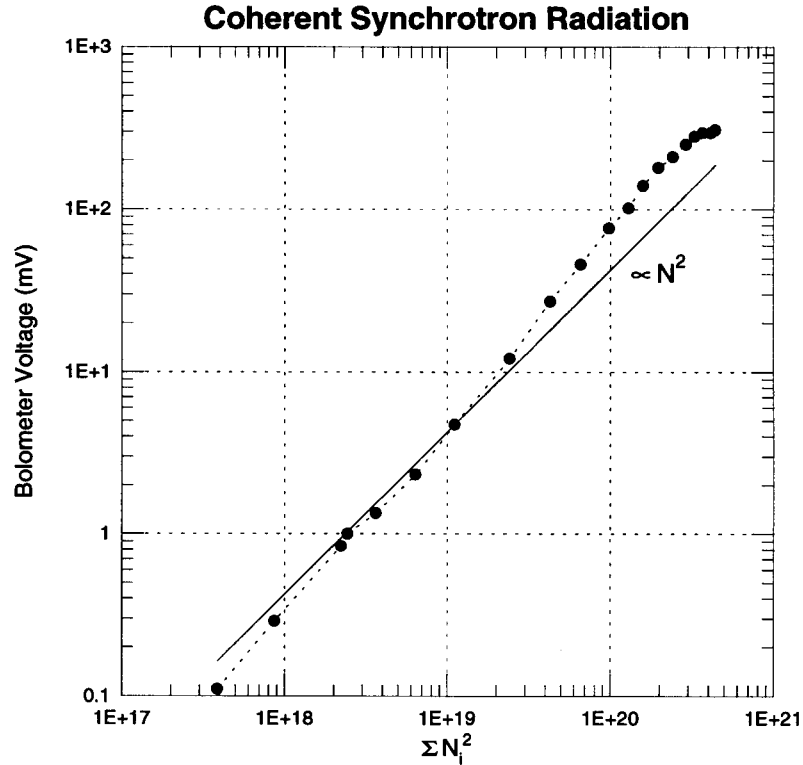
Figure 1.8: Bolometer signal of coherent synchrotron radiation as a function of electron beam current.

The energy of the collected coherent synchrotron radiation from each macro-pulse is measured with the bolometer as a function of the electron beam current. The current distribution across the macro-pulse is measured through a pulse transformer surrounding an insulated section of beam pipe. No means are available at SUNSHINE to measure both the radiation intensity and the beam current signal from individual electron bunches. Since the transformer can not resolve individual bunches and the current signal is not uniform across the macro-pulse, the signal is dissected into about 400 slices in time through a LeCroy digital oscilloscope, and the sum of the squares of the number of electrons in each each slice is then calculated (denoted as $\sum N_i^2$) to approximate the sum of the squares of the number of electrons in each bunch, which is expected from the ideal case. The measured bolometer signal as a function of $\sum N_i^2$ is

shown in Fig. 1.8[16]. The coherent radiation intensity shows the expected quadratic dependence on the electron charges over 3 orders of magnitude. Small deviations from the ideal quadratic scaling are due to unavoidable variations of bunch length for different segments of the momentum spectrum selected by the method of changing the electron beam current.

1.3.2.2 Total Energy Measurement

The total collected energy of coherent synchrotron radiation from each macro-pulse is measured as[16]

262 μJ per macro-pulse

with an rms electron intensity of 4.6×10^8 electrons per bunch. This measurement has excluded the possibility of the contribution from other sources such as wake field and ionization radiation. To compare this result with theory, a few factors which are significantly different from ideal calculations have to be taken into account[16]:

1. As the electrons are passing through the dipole magnet, the emitted radiation changes direction and sweeps across the mirror. These rays of different angles are accepted differently by the collecting optics.

2. As the electrons enter the magnet, the field increases from zero to its nominal strength over a distance of 40 mm (equal to the pole gap). This fringe field contributes significantly to the production of radiation.

3. The opening angle of coherent synchrotron radiation is a function of photon frequency and changes with the magnetic field. This affects the collection efficiency for different frequencies as well as different source points in the magnet.

4. The HDPE window has a 87% trasmission efficiency in the far-infrared regime.

5. The bunch length and beam current changes along the macro-pulse due to a vary-ing RF field level in the gun caused by beam loading. Through the measurement of momentum distribution in the macro-pulse, the effect of beam loading on the bunch length can be studied in simulations of electron bunch production, and the bunch length variation across a macro-pulse can be derived from these sim-ulations[15,16]. Simulations show that the bunch length varies from 1.2 ps down to 0.2 ps in different parts of a macro-pulse.

When these factors are considered in the theoretical calculation described in Sec. 1.1.4 with the assumption of a Gaussian bunch distribution, the calculated total energy from a macro-pulse accepted by the collecting optics with a resulting overall 47% collection efficiency is[15,16]

$$217 \, \mu\text{J per macro-pulse.}$$

This calculated result agrees with the measured one within a 17% difference. Calcula-tions further indicate that the total radiation intensity is equivalent to that emitted in 40 mrad of bending angle from 2856 identical Gaussian electron bunches with equiva-lent bunch length of 0.475 ps and beam intensity of 4.6×10^8 electrons in each bunch. Each bunch radiates a total energy of about $0.168 \, \mu\text{J}$, and about $0.076 \, \mu\text{J}$ of the radiated energy is accepted by the collecting optics.

Chapter 2

Coherent Transition Radiation

As described in the previous chapter, the experimental results of coherent synchrotron radiation emitted from subpicosecond electron bunches agree very well with theoretical calculations. This provides a promising direction of using the coherent radiation from subpicosecond electron bunches to develop a new high-intensity, far-infrared light source. However, the way to produce coherent synchrotron radiation dose not offer an easy and clean way to collect and manipulate the emitted radiation for applications using this radiation. As the electrons are moving along a curved path in the dipole magnet, the emitted radiation changes its direction and sweeps across the collecting optics along this path. This long curved emitting path extents the radiation source size and increases the complexity of the optics for efficient light collection. Besides, in order to have enough deflection strength on the electron beam, the size of the dipole magnet used to generate the radiation can not be made compact. All these undesirable features put drawbacks on the applicability of coherent synchrotron radiation as an easy-to-use light source.

On the other hand, coherent transition radiation, which will be discussed in this chapter, has some advantages over coherent synchrotron radiation in the respect of being a "user-friendly" light source. As the electron bunch moves from vacuum

into matter or vice versa, coherent transition radiation is emitted from the point of incidence. Since the radiation has a very well defined geometry of emission, the light collection and manipulation optics becomes very simple. Furthermore, the device to generate this radiation is simple and compact—for example, a metal foil held by a metal ring. These features make coherent transition radiation an attractive light source.

This chapter introduces coherent transition radiation emitted from subpicosecond electron bunches and discusses the properties of this radiation. In order to characterize the spectrum of coherent transition radiation, a new autocorrelation method based on a far-infrared Michelson interferometer has been developed at SUNSHINE. Using this method, the spectrum of the coherent radiation emitted from subpicosecond electron bunches is measured for the first time. This method also yields an interesting byproduct: a new subpicosecond bunch-length measuring system. Through the characterization of the spectrum of coherent transition radiation and the measurement of the electron bunch length, the production of subpicosecond electron bunches at SUNSHINE was confirmed, and the possibility of using coherent transition radiation as a high-intensity far-infrared light source is verified. This provides the foundation for the next chapter.

Not only does this autocorrelation method have a great value to this thesis, but it also plays an important role in the field of accelerator physics by providing a new and effective way to measure subpicosecond electron bunch lengths in accelerators. Due to the requirements for the next-generation particle colliders and light sources, the reduction of electron bunch length has become an interesting aspect in the development of particle accelerators. Its progress greatly affects the design of next-generation synchrotron light sources, future linear colliders, free-electron lasers, and high-intensity coherent far-infrared light sources. These proposed future machines demand femtosecond electron bunch lengths which can not be measured with any existing instrument,
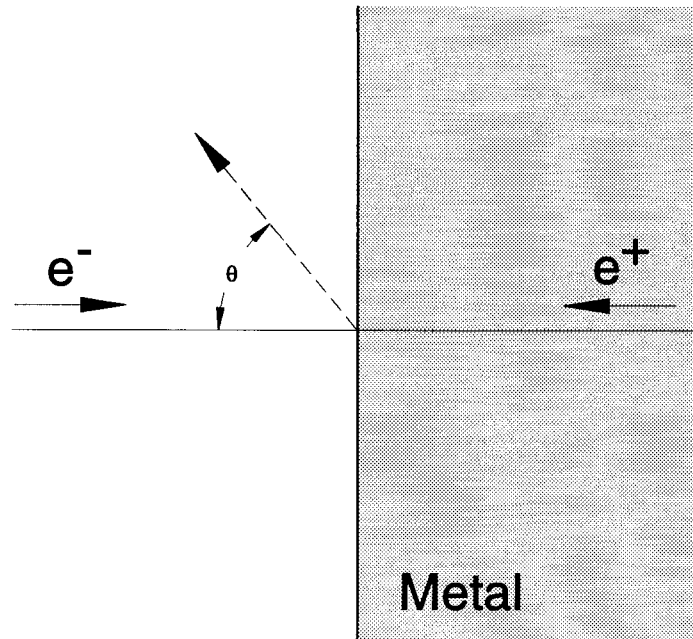
Figure 2.1: Transition radiation for the case of a perfect conductor. This case can be viewed as the electron collides with its positive image charge. The arrow with a dashed line indicates the direction of the emitted radiation.

for example, a streak camera. Hence, a bunch-length measuring system capable of characterizing subpicosecond pulses such as this autocorrelation method will provide a powerful tool in support of these developments.

2.1 Transition Radiation

Transition radiation is generated when an electron passes the interface of two media of different dielectric constants. The sudden transition in the dielectric constants of the media along the electron's path causes a discontinuity in the electric field at the interface. This discontinuity makes the electron radiate at the medium boundary, and the radiation is called *transition radiation*. This phenomenon was first predicted

by Ginsburg and Frank in 1946[22].

2.1.1 A Simple Picture

To understand this process, let us first consider a special case. As shown in Fig. 2.1, an electron of velocity v moves from vacuum into a perfect conductor in a direction normal to the interface. Since the metal is a perfect conductor, a positive image charge of the electron with equal charge located at the same distance as the electron from the metal-vacuum interface but on the opposite side to the electron can be introduced to simulate the required boundary conditions without the presence of the metal. As referred as *method of images*[23, Sec. 2.1], this method reduces the problem from a complicated boundary-value problem into a simpler two-charged-particle collision problem.

Hence, the solution to the radiation emitted during collisions can be directly applied to this transition radiation problem. The energy radiated per unit angular frequency ($\omega \equiv 2\pi\nu$) per unit solid angle by N particles during the collision can be expressed as[23, extended from Eq. (15.1)]

$$\frac{\mathrm{d}^2\mathcal{E}}{\mathrm{d}\omega\mathrm{d}\Omega} = \frac{1}{4\pi^2 c}\left|\sum_{j=1}^{N}\int\frac{\mathrm{d}}{\mathrm{d}t}\left[\frac{q_j\,\hat{\mathbf{n}}\times(\hat{\mathbf{n}}\times\boldsymbol{\beta}_j)}{1-\hat{\mathbf{n}}\cdot\boldsymbol{\beta}_j}\right]e^{i\omega[t-\hat{\mathbf{n}}\cdot\mathbf{r}_j(t)/c]}\,\mathrm{d}t\right|^2 , \qquad (2.1)$$

where $\hat{\mathbf{n}}$ is the unit vector of the direction of the radiation, q_j is the charge of the jth particle, $\boldsymbol{\beta}_j$ is the vector in the direction of the jth particle's motion with velocity v_j and $|\boldsymbol{\beta}_j| = \beta_j \equiv v_j/c$, c is the speed of light, and $\mathbf{r}_j(t)$ is the position vector of the jth particle at time t. Let us suppose that the frequencies ω of the radiation that we are interested in are much smaller than $1/\tau$, where τ is the duration of the collision. In this limit ($\omega\tau \ll 1$, or $\omega \to 0$), the exponential factor in Eq. (2.1) is equal to unity, and the integrand is a perfect differential. The radiation at these low frequencies only

depends on the initial and final velocities; hence, we have

$$\lim_{\omega \to 0} \frac{\mathrm{d}^2\mathcal{E}}{\mathrm{d}\omega \mathrm{d}\Omega} = \frac{1}{4\pi^2 c} \left| \sum_{j=1}^{N} \int_{\beta_j^{(\mathrm{initial})}}^{\beta_j^{(\mathrm{final})}} \mathrm{d} \left[\frac{q_j \, \hat{\mathbf{n}} \times (\hat{\mathbf{n}} \times \beta_j)}{1 - \hat{\mathbf{n}} \cdot \beta_j} \right] \right|^2, \qquad (2.2)$$

where $\beta_j^{(\mathrm{initial})}$ and $\beta_j^{(\mathrm{final})}$ are the initial and final β's for the jth particle.

For the system shown in Fig. 2.1, we have two particles: one electron of charge $q_1 = -|e|$ with $\beta_1^{(\mathrm{initial})} = \beta$ and one image positron of charge $q_2 = +|e|$ with $\beta_2^{(\mathrm{initial})} = -\beta$, where e is the electronic charge. For both particles, $\beta^{(\mathrm{final})} = 0$. Applying these conditions to Eq. (2.2), we have

$$\begin{aligned} \lim_{\omega \to 0} \frac{\mathrm{d}^2\mathcal{E}}{\mathrm{d}\omega \mathrm{d}\Omega} &= \frac{1}{4\pi^2 c} \left| -\frac{-|e| \, \hat{\mathbf{n}} \times (\hat{\mathbf{n}} \times \beta)}{1 - \hat{\mathbf{n}} \cdot \beta} - \frac{+|e| \, \hat{\mathbf{n}} \times (\hat{\mathbf{n}} \times [-\beta])}{1 - \hat{\mathbf{n}} \cdot [-\beta]} \right|^2 \\ &= \frac{e^2}{4\pi^2 c} \left| \frac{\hat{\mathbf{n}} \times (\hat{\mathbf{n}} \times \beta)}{1 - \hat{\mathbf{n}} \cdot \beta} + \frac{\hat{\mathbf{n}} \times (\hat{\mathbf{n}} \times \beta)}{1 + \hat{\mathbf{n}} \cdot \beta} \right|^2 \\ &= \frac{e^2}{4\pi^2 c} \left| \frac{2 \, \hat{\mathbf{n}} \times (\hat{\mathbf{n}} \times \beta)}{(1 - \hat{\mathbf{n}} \cdot \beta)(1 + \hat{\mathbf{n}} \cdot \beta)} \right|^2. \end{aligned} \qquad (2.3)$$

By denoting θ as the angle between $\hat{\mathbf{n}}$ and $-\beta$ [i.e., $\cos\theta = \hat{\mathbf{n}} \cdot (-\beta)$], we can derive the spectral energy density per solid angle for transition radiation as

$$\frac{\mathrm{d}^2\mathcal{E}}{\mathrm{d}\omega \mathrm{d}\Omega} = \frac{e^2}{\pi^2 c} \frac{\beta^2 \sin^2 \theta}{(1 - \beta^2 \cos^2 \theta)^2}. \qquad (2.4)$$

Since the collision time τ is very short, this expression is valid for, but not limited to, frequencies in the far-infrared regime.

On the other hand, when an electron emerges from a perfect conductor into vacuum, the problem can be treated as if the electron and its positive image charge were created at the metal-vacuum interface. Both charges are accelerated form rest to velocity v and traveling in opposite directions. By substituting appropriate initial and final β's into Eq. (2.2) for both particles, the angular spectral energy density can be derived and shares the same formalism as described in Eq. (2.4) with the previous case. Finally, for the case of oblique incidence, the energy density can be derived from Eq. (2.2) with appropriate geometry for the electron and its image charge. However, the derivation is out of the scope of this thesis.
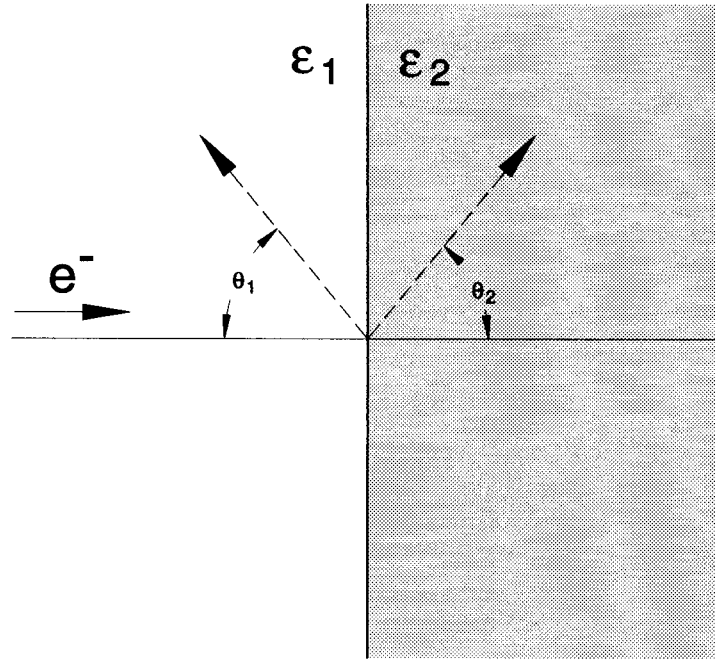
Figure 2.2: Transition radiation for the case of two different dielectric media. The arrows with dashed lines indicate the direction of the emitted radiation in two media.

2.1.2 General Cases

The result of transition radiation using method of images is only valid for the case of perfect or near perfect conductors. To calculate the radiation for the case of normal dielectric materials, one has to solve the Maxwell's equations with appropriate boundary conditions. This problem has been solved before[24], and only results relevant to this thesis are discussed in the following sections.

2.1.2.1 Normal Incidence on a Single Interface

When an electron of velocity v moves from one medium of dielectric constant ε_1 into another of dielectric constant ε_2 in a direction normal to the interface as shown in Fig. 2.2, the angular spectral energy density for backward transition radiation

(radiated into the left-hand half-space in medium 1) is expressed as[24, Sec. 24]

$$\frac{\mathrm{d}^2\mathcal{E}_1}{\mathrm{d}\omega\mathrm{d}\Omega} = \frac{e^2\beta^2\sqrt{\varepsilon_1}\,\sin^2\theta_1\,\cos^2\theta_1}{\pi^2 c}$$

$$\times \left|\frac{(\varepsilon_2 - \varepsilon_1)(1 - \beta^2\varepsilon_1 + \beta\sqrt{\varepsilon_2 - \varepsilon_1\sin^2\theta_1})}{(1 - \beta^2\varepsilon_1\cos^2\theta_1)(1 + \beta\sqrt{\varepsilon_2 - \varepsilon_1\sin^2\theta_1})(\varepsilon_2\cos\theta_1 + \sqrt{\varepsilon_1\varepsilon_2 - \varepsilon_1^2\sin^2\theta_1})}\right|^2,$$

$$(2.5)$$

where β is defined as v/c, and the dielectric constants ε_1 and ε_2 are, in general, complex numbers and functions of frequency. The angular spectral energy density for forward transition radiation (radiated into the right-hand half-space in medium 2) can be obtained from Eq. (2.5) by swapping subscripts (i.e., $1 \rightleftharpoons 2$) and replacing β with $-\beta$. The frequency dependence of the radiation energy density is determined by the frequency dependencies of the complex dielectric constants $\varepsilon_1(\omega)$ and $\varepsilon_2(\omega)$. The radiation is polarized in the direction parallel to the *radiation plane*, which is the plane containing the wave propagation vector and the normal to the interface. The directions of polarization are circularly symmetric about the electron moving direction.

This formula can be applied to any case for which the dielectric constants of the materials are known in the frequency range of importance to the problem. One interesting case is that for a perfect conductor, whose dielectric constant is infinitely large (i.e., $|\varepsilon(\omega)| \rightarrow \infty$, for all frequencies ω). At this limit, Eq. (2.5) reduces to Eq. (2.4). It is worth noticing that "good" conductors such as silver, gold, and aluminum behave almost like perfect conductors in the far-infrared regime. This will be discussed in Sec. 2.1.3.

2.1.2.2 Oblique Incidence on a Plate

Let us consider the most general case for transition radiation. As shown in Fig. 2.3, an electron of velocity v penetrates a plate in vacuum of dielectric constant ε and
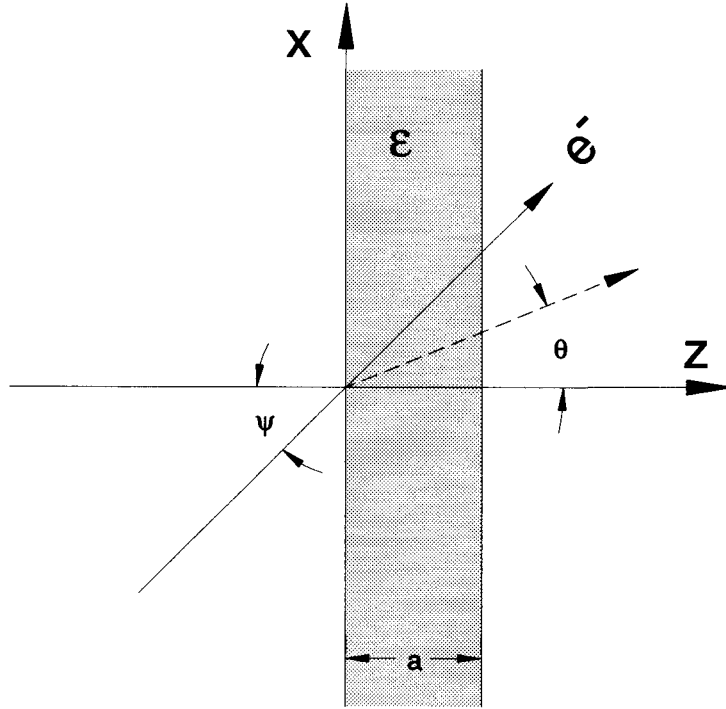
Figure 2.3: Transition radiation for the case of oblique incidence on a plate. The arrow with a dashed line indicates the direction of the total emitted radiation.

thickness a. It moves in the direction at an angle ψ to the normal of the plate surface. The emitted transition radiation no longer has a single component of polarization with respect to the radiation plane; instead, it has components parallel and perpendicular to the plane. Before we show these components, let us choose the following Cartesian coordinate system as shown in Fig. 2.3 with β in the xz plane, where β is the electron motion vector and $|\beta| = \beta \equiv v/c$: the direction normal to the plate surface as $\hat{z}$, the direction of $\hat{z} \times \beta$ as $\hat{y}$, and the direction of $(\hat{z} \times \beta) \times \hat{z}$ as $\hat{x}$. Hence, the vectors β can be expressed as

$$\begin{aligned}
\beta &\equiv \beta_x\,\hat{x} + \beta_y\,\hat{y} + \beta_z\,\hat{z} \\
&= \beta \sin\psi\,\hat{x} + \beta \cos\psi\,\hat{z},
\end{aligned} \tag{2.6}$$

since $\beta_y = 0$.

The parallel component of spectral angular energy density radiated into the right-hand half-space (i,e., the *forward* direction) is[24, Sec. 25]

$$\frac{\mathrm{d}^2 \mathcal{E}_{\text{forward}}^{\|}}{\mathrm{d}\omega \mathrm{d}\Omega} = \frac{e^2 \beta_z^2}{\pi^2 c} \frac{\cos^2 \theta_z}{\sin^2 \theta_z}$$

$$\times \left| \frac{\varepsilon - 1}{[(1 - \beta_x \cos \theta_x)^2 - \beta_z^2 x^2][(1 - \beta_x \cos \theta_x)^2 - \beta_z^2 \cos^2 \theta_z]} \right|^2$$

$$\times \left| \frac{B_\psi^{\|}}{(x + y)^2 e^{-i(\omega a/c)x} - (x - y)^2 e^{i(\omega a/c)x}} \right|^2, \qquad (2.7)$$

where

$$B_\psi^{\|} = (x + y)(1 - \beta_x \cos \theta_x + \beta_z x)$$

$$\times [(1 - \beta_z^2 - \beta_x \cos \theta_x - \beta_z x) \sin^2 \theta_z + \beta_x \beta_z x \cos \theta_x] e^{-i(\omega a/c)x}$$

$$+ (x - y)(1 - \beta_x \cos \theta_x - \beta_z x)$$

$$\times [(1 - \beta_z^2 - \beta_x \cos \theta_x + \beta_z x) \sin^2 \theta_z - \beta_x \beta_z x \cos \theta_x] e^{i(\omega a/c)x}$$

$$- 2x[(1 - \beta_x \cos \theta_x + \beta_z y)(1 - \beta_z^2 - \beta_x \cos \theta_x) \sin^2 \theta_z$$

$$+ \beta_z(\beta_x \cos \theta_x - \sin^2 \theta_z)(\beta_z x^2 + y - \beta_x y \cos \theta_x)] e^{-i(\omega a/v_z)(1 - \beta_x \cos \theta_x)}, \quad (2.8)$$

and

$$x = \sqrt{\varepsilon - \sin^2 \theta_z}, \qquad y = \varepsilon \cos \theta_z. \qquad (2.9)$$

On the other hand, the perpendicular component of spectral angular energy density radiated into the right-hand half-space is expressed as

$$\frac{\mathrm{d}^2 \mathcal{E}_{\text{forward}}^{\perp}}{\mathrm{d}\omega \mathrm{d}\Omega} = \frac{e^2 \beta_x^2 \beta_z^4}{\pi^2 c} \frac{\cos^2 \theta_y \cos^2 \theta_z}{\sin^2 \theta_z}$$

$$\times \left| \frac{\varepsilon - 1}{[(1 - \beta_x \cos \theta_x)^2 - \beta_z^2 x^2][(1 - \beta_x \cos \theta_x)^2 - \beta_z^2 \cos^2 \theta_z]} \right|^2$$

$$\times \left| \frac{B_\psi^{\perp}}{(x + y/\varepsilon)^2 e^{-i(\omega a/c)x} - (x - y/\varepsilon)^2 e^{i(\omega a/c)x}} \right|^2, \qquad (2.10)$$

where

$$B_\psi^{\perp} = (x + \frac{y}{\varepsilon})(1 - \beta_x \cos \theta_x + \beta_z x) e^{-i(\omega a/c)x}$$

$$+ \quad (x - \frac{y}{\varepsilon})(1 - \beta_x \cos\theta_x - \beta_z x)e^{i(\omega a/c)x}$$
$$- \quad 2x(1 - \beta_x \cos\theta_x + \beta_z \cos\theta_z)e^{-i(\omega a/v_z)(1-\beta_x \cos\theta_x)}. \tag{2.11}$$

The oscillatory exponential factors are the interference effects caused by the radiation emitted from both interfaces. When the thickness is reduced to zero ($a \to 0$), all radiation components vanish since the interference is destructive.

The direction of the emitted radiation for forward transition radiation is described by the direction cosines defined with respect to the axes x, y, and z:

$$\cos\theta_x = \sin\theta \cos\phi,$$
$$\cos\theta_y = \sin\theta \sin\phi, \tag{2.12}$$
$$\cos\theta_z = \cos\theta,$$

where θ is the angle between the wave propagation vector and the $+z$ axis, and ϕ is the azimuthal angle defined on the xy plane with respect to the $+x$ axis.

Similarly, the two components of spectral angular energy density for radiation emitted into the left-hand half-space (i.e., the *backward* direction) can be obtained from these equations simply by replacing β with $-\beta$ for all corresponding components. For the direction of backward radiation, the direction cosines are still expressed as Eq. (2.12), however, with respect to the $-x$, y, and $-z$ axes with θ, the angle between the wave propagation vector and the $-z$ axis, and ϕ, the azimuthal angle defined on the xy plane with respect to $-x$ axis.

If the plate is a perfect conductor ($\varepsilon \to \infty$), the two components of the spectral angular energy density for the forward radiation is only emitted from the metal-to-vacuum interface and can be simplified as[24, Sec. 25]

$$\frac{\mathrm{d}^2 \mathcal{E}_{\text{forward}}^{\parallel}}{\mathrm{d}\omega \mathrm{d}\Omega} = \frac{e^2\beta^2 \cos^2\psi}{\pi^2 c} \left[\frac{\sin\theta - \beta\cos\phi\sin\psi}{(1 - \beta\sin\theta\cos\phi\sin\psi)^2 - \beta^2\cos^2\theta\cos^2\psi} \right]^2 \tag{2.13}$$

$$\frac{\mathrm{d}^2 \mathcal{E}_{\text{forward}}^{\perp}}{\mathrm{d}\omega \mathrm{d}\Omega} = \frac{e^2\beta^2 \cos^2\psi}{\pi^2 c} \left[\frac{\beta\cos\theta\sin\phi\sin\psi}{(1 - \beta\sin\theta\cos\phi\sin\psi)^2 - \beta^2\cos^2\theta\cos^2\psi} \right]^2 . \tag{2.14}$$

Similarly, the expressions of energy density for the backward radiation is only emitted by the vacuum-to-metal interface and is derived by replacing β with $-\beta$ in the above equations. For normal incidence ($\psi = 0$), the parallel components reduces to Eq. (2.4), while the perpendicular components vanish for both forward and backward radiation.

2.1.3 Dielectric Constants of Metals

As described in the previous section, the frequency dependency of transition radiation is determined by that of the complex dielectric constants of participating media. Only when the dielectric constants in the frequency range of interest are known theoretically or experimentally, the calculation of transition radiation will become possible. In this thesis, we are interested in radiation in the far-infrared regime emitted from conducting metal foils such as silver, gold, and aluminum placed in vacuum or air ($\varepsilon_{air} \approx 1$). So it is necessary to know the dielectric constants of these well conducting metals in the far-infrared regime.

By assuming that the conduction electrons in metals form a free-electron gas, the Drude model[25,26] gives a very good agreement between the experimental results of reflectance of silver, gold, and aluminum and the theoretical values using the predicted dielectric constants in the far-infrared regime[27–29]. By modeling the conduction electrons as damped harmonic oscillators driven by the external electromagnetic field, the complex dielectric constant at angular frequency ω ($\omega = 2\pi\nu$) is obtained, in CGS unit, as[28,29]

$$\varepsilon(\omega) = 1 - \frac{\Omega_p^2}{\omega(\omega + i/\tau)} + \delta\varepsilon, \tag{2.15}$$

where Ω_p is the plasma frequency, $\delta\varepsilon$ is a small contribution from "bound-electron" absorptions, and τ is the relaxation time, which is related to the damping constant γ by $\tau = 1/\gamma$. Traditionally, the parameters chosen for the Drude model are the dc conductivity $\sigma(0)$ and the relaxation constant τ. The plasma frequency can then be

Table 2.1: Parameters used in the Drude model for the calculation of dielectric constants of silver, gold, and aluminum.

Metal	$\sigma(0)$ (sec^{-1})	τ (sec)
Silver (Ag)	5.41×10^{17}	3.65×10^{-14}
Gold (Au)	3.68×10^{17}	2.46×10^{-14}
Aluminum (Al)	3.18×10^{17}	8.01×10^{-15}
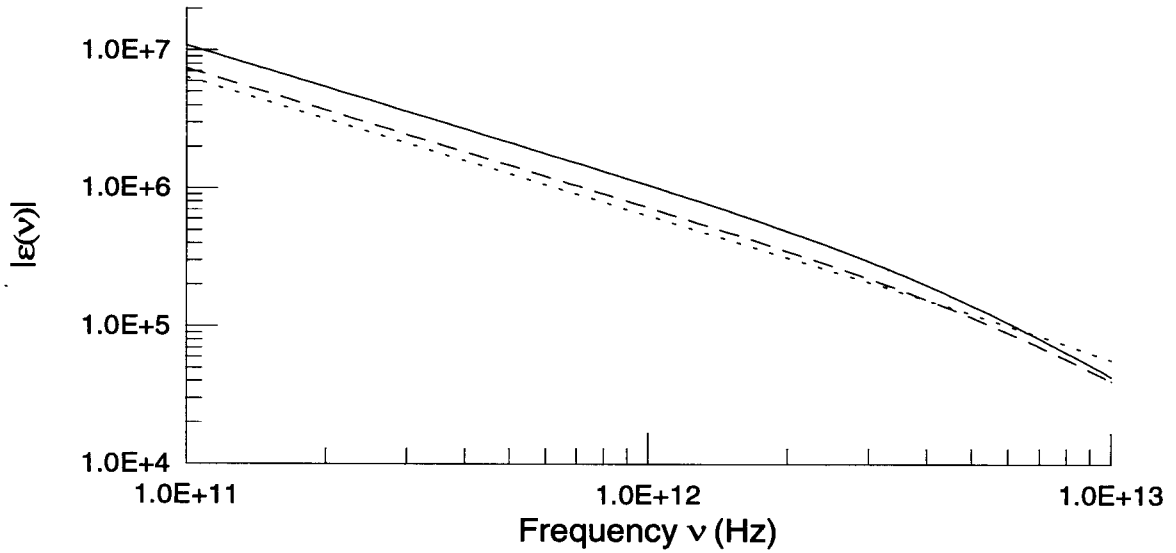
Figure 2.4: The magnitudes of the dielectric constants for silver (solid), gold (dashed), and aluminum (dotted line) for frequencies in the far-infrared regime.

expressed as

$$\Omega_p^2 = 4\pi\sigma(0)/\tau. \tag{2.16}$$

The contribution of $\delta\varepsilon$ is small in the far-infrared regime and is ignored here (i.e., $\delta\varepsilon = 0$). The parameters used to calculate the dielectric constants of silver, gold, and aluminum are listed in Table 2.1[27].

Using the listed parameters, the absolute values of the dielectric constants for the three "good" conducting metals are calculated for frequencies in the far-infrared regime and shown in Fig. 2.4. Since the magnitudes of the dielectric constants for

Figure 2.5: The angular distribution of single-electron transition radiation emitted from a perfect conductor for the case of normal incidence. The electron energies shown here are $\gamma = \sqrt{2}$ (dotted), 5 (dash-dotted), and 10 (solid line).

these good conductors are at least four orders of magnitude above unity in the far-infrared regime, the numerical difference between the energy density calculated for perfect conductors [using Eq. (2.4)] and real conductors [using Eqs. (2.5) and (2.15)] is negligible. Hence, the formulas for the perfect conductor case can be used to simplify the calculations for good conductors without loosing significance.

2.2 Properties of Transition Radiation

We have introduced the formalism for transition radiation emitted from different cases. Since the good conductors such as silver, gold, and aluminum behave like a perfect conductor in the production of transition radiation in the far-infrared regime, we

will, for simplicity, use the formulas for a perfect conductor [i.e., Eqs. (2.4) and (2.13)] to discuss the properties of transition radiation.

2.2.1 The Radiation Pattern

The first property of transition radiation we will explore is the radiation pattern. As expressed in Eq. (2.4) for the normal incident case, the radiation field has a zero at $\theta = 0$ and a maximum of $e^2\gamma^2/(4\pi^2\beta^2 c)$ at $\sin\theta = 1/(\beta\gamma)$, where γ is the Lorentz factor with $\gamma = 1/\sqrt{1 - \beta^2}$. The radiation has azimuthal symmetry, and its θ dependence is shown in Fig. 2.5. For $\gamma \leq \sqrt{2}$, the maximum is located at $\theta = \pi/2$. As the energy of the electron increases (i.e., γ increases), this maximum moves toward the forward direction ($\theta = 0$), and its amplitude increases quadratically with γ. For a relativistic electron ($\gamma \gg 1$), this maximum is located at the angle $\theta \sim 1/\gamma$ with an amplitude of $e^2\gamma^2/4\pi^2 c$. Both forward and backward transition radiation have the same angular distribution.

For the case of oblique incidence, transition radiation in both directions have similar angular distributions as that for the normal incident case. However, the angular distributions of the radiation in both directions have slight asymmetry. As shown in Fig. 2.6, the radiation lobe closer to the z axis (the $\phi > 0$ side) is slightly smaller than that at larger angle side (closer to the x axis or the $\phi < 0$ side) for the oblique incident case when referred to the geometry in Fig. 2.3. The average of these two lobes is about the same height as the lobes for the normal incident case. At larger electron energy this asymmetry is reduced, and the radiation distribution is closer to that for the normal incident case.

The orientations of the radiation lobes are also different in both normal and oblique incident cases. The radiation lobes for the normal incident case are symmetrically distributed around the direction of electron motion (z axis). For the oblique incident case, as described in Eq. (2.13) and shown in Fig. 2.7, the forward radiation lobes
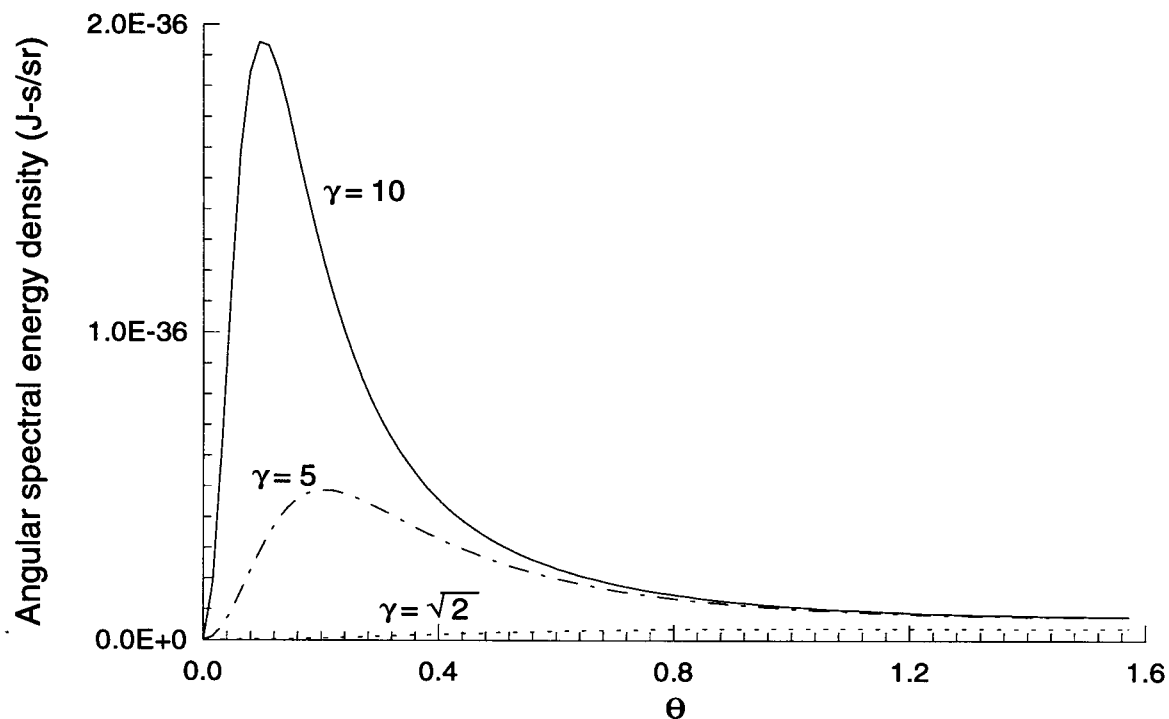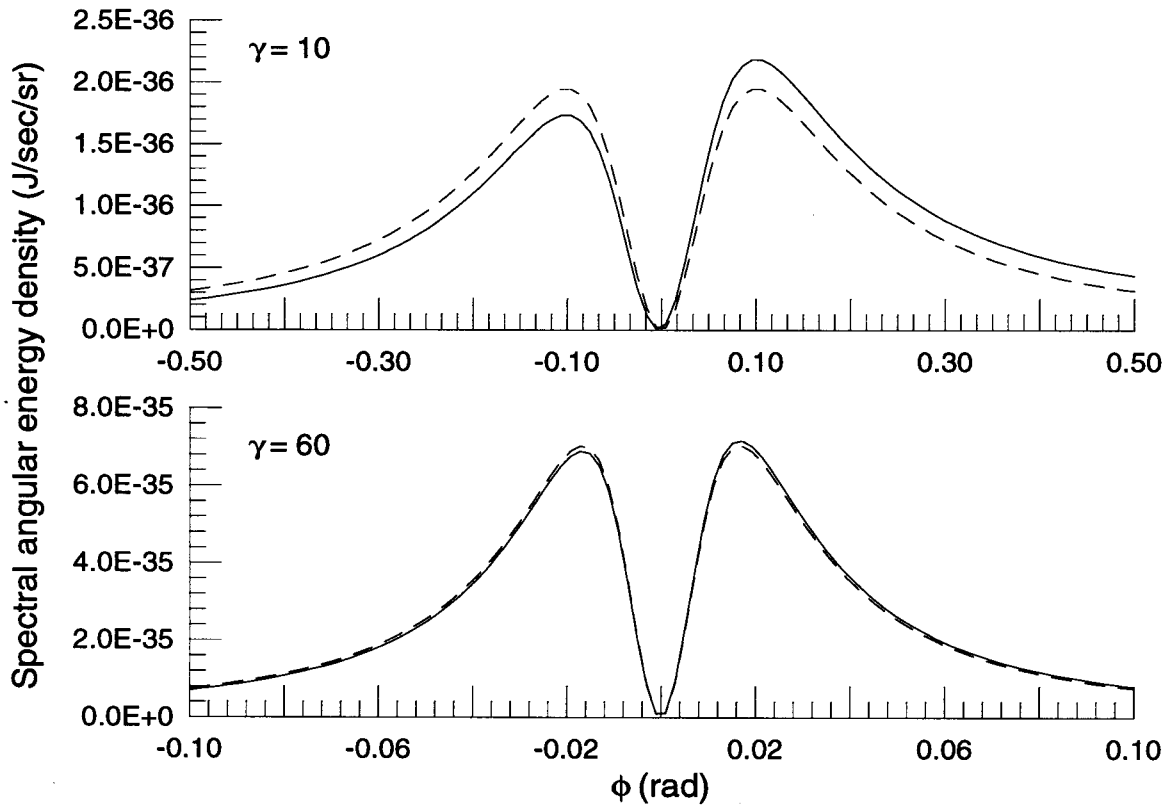
Figure 2.6: The angular distribution of transition radiation emitted from a perfect conductor for the cases of normal ($\psi = 0°$, dashed) and oblique ($\psi = 30°$, solid lines) incidence in the forward direction. The electron energies shown here are $\gamma = 10$ and 60. The angle ϕ is defined with respect to the directions of electron motion, i.e., $\phi = \theta - \psi$ when referred to the geometry in Fig. 2.3. Positive ϕ means the angle is in the counterclockwise side of ψ, while negative ϕ means the angle is in the clockwise side of ψ.

(a) ψ = 0   **(b) ψ = π/6**
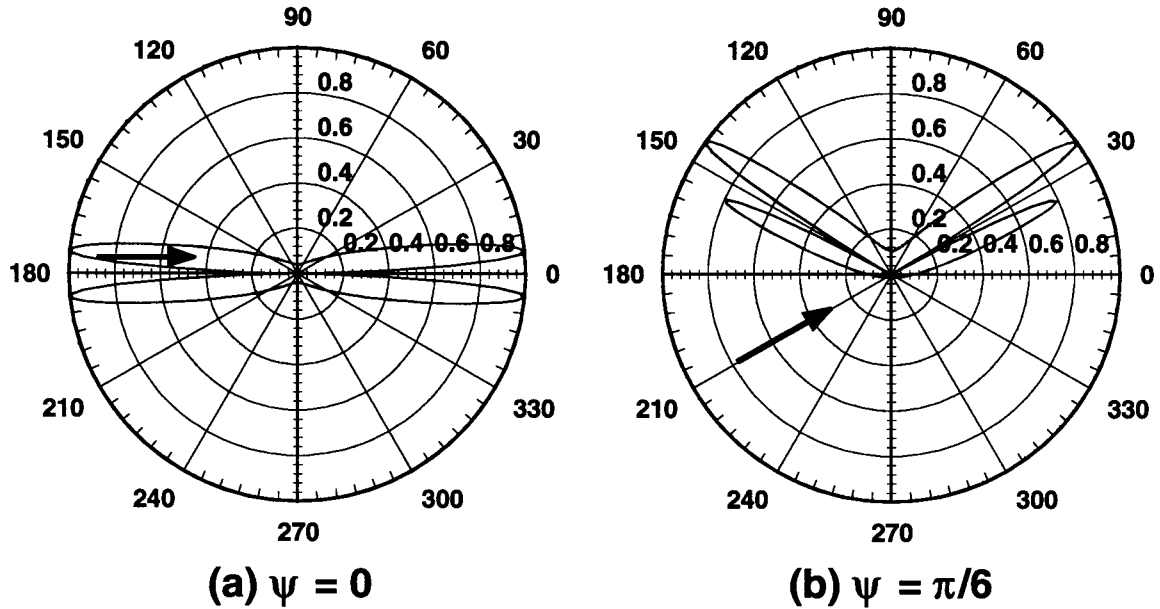
Figure 2.7: The radiation lobes for forward and backward transition radiation in the xz plane for (a) normal ($\psi = 0$) and (b) oblique ($\psi = \pi/6 = 30°$) incidence. The radiation lobes are plotted in a polar coordinate using the angle of radiation (θ in units of degree) and the relative amplitude to the maximum at that angle. The arrows indicate the direction of electron motion expressed as the angle ψ with respect to the $+z$ axis (180° → 0° line). The plate is located on the x axis (270° → 90° line) when referred to the geometry in Fig. 2.3. The electron energy is set to $\gamma = 10$.

are emitted into the direction of electron motion β at an angle ψ to the $+z$ axis; however, the backward radiation lobes in this case are emitted in the direction at an angle $\pi - \psi$ to the $+z$ axis. These directions are the same as those of transmitted (forward) and reflected (backward) waves from the wave incident in the direction of electron motion. The asymmetry of the radiation lobes for oblique incidence is also clear in the figure, which shows that the lobes closer to the z axis (180° → 0° line) are smaller than those closer to the x axis (270° → 90° line) when referred to the geometry in Fig. 2.3.
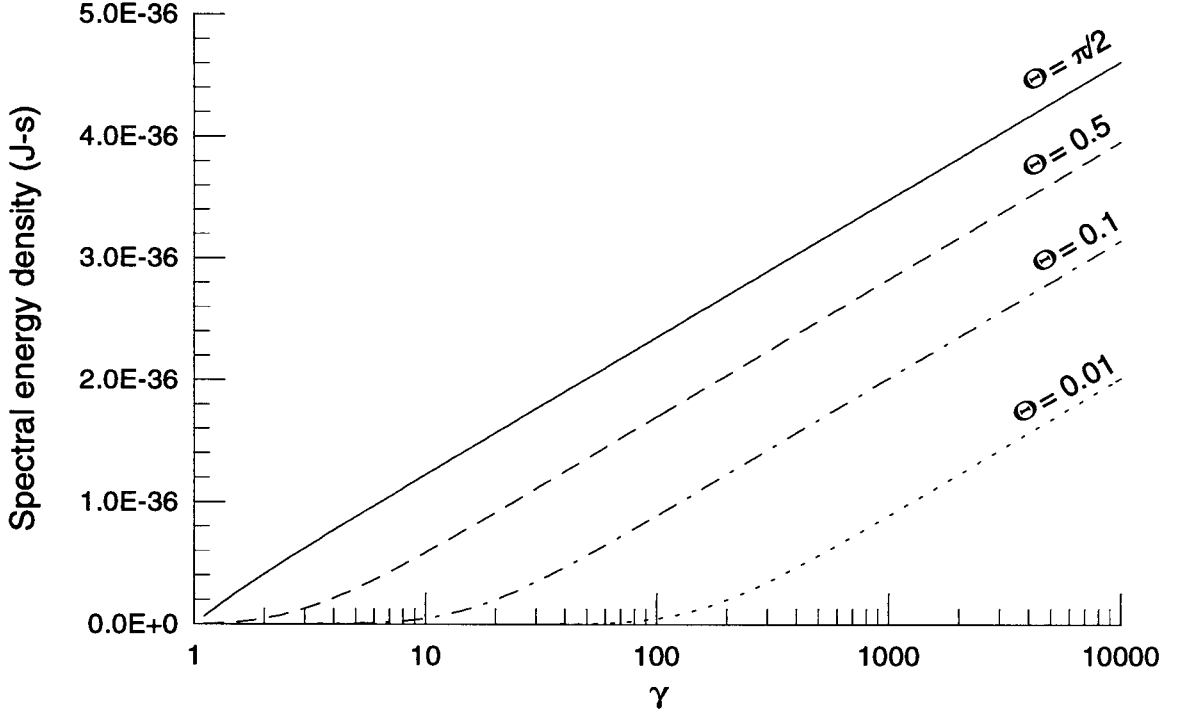
Figure 2.8: Collected transition radiation energy for a single electron as a function of electron energy. Θ is the acceptance angle of the collecting optics.

2.2.2 Collection Efficiency

As described in the previous section, transition radiation from an electron originates at the point of incidence and is radiated into all directions with a special radiation pattern. In this section, we will study the collection efficiency of the radiation with respect to the energy of the electron and the angular acceptance. To simplify the discussion, only the radiation from a perfect conductor for normal incidence will be considered here. Assuming that the angular acceptance of the collecting optics is Θ, the energy collected within that angle can be expressed, using Eq. (2.4), as

$$\int_0^{2\pi} d\phi \int_0^{\Theta} \frac{d^2\mathcal{E}}{d\omega d\Omega} \sin\theta \, d\theta = \frac{e^2}{2\pi\beta c} \frac{1}{1 - \beta^2 \cos^2\Theta}$$

$$\times \left\{ (1 + \beta^2)(1 - \beta^2 \cos^2\Theta) \ln \left[\frac{(1 - \beta\cos\Theta)(1 + \beta)}{(1 + \beta\cos\Theta)(1 - \beta)} \right] \right.$$
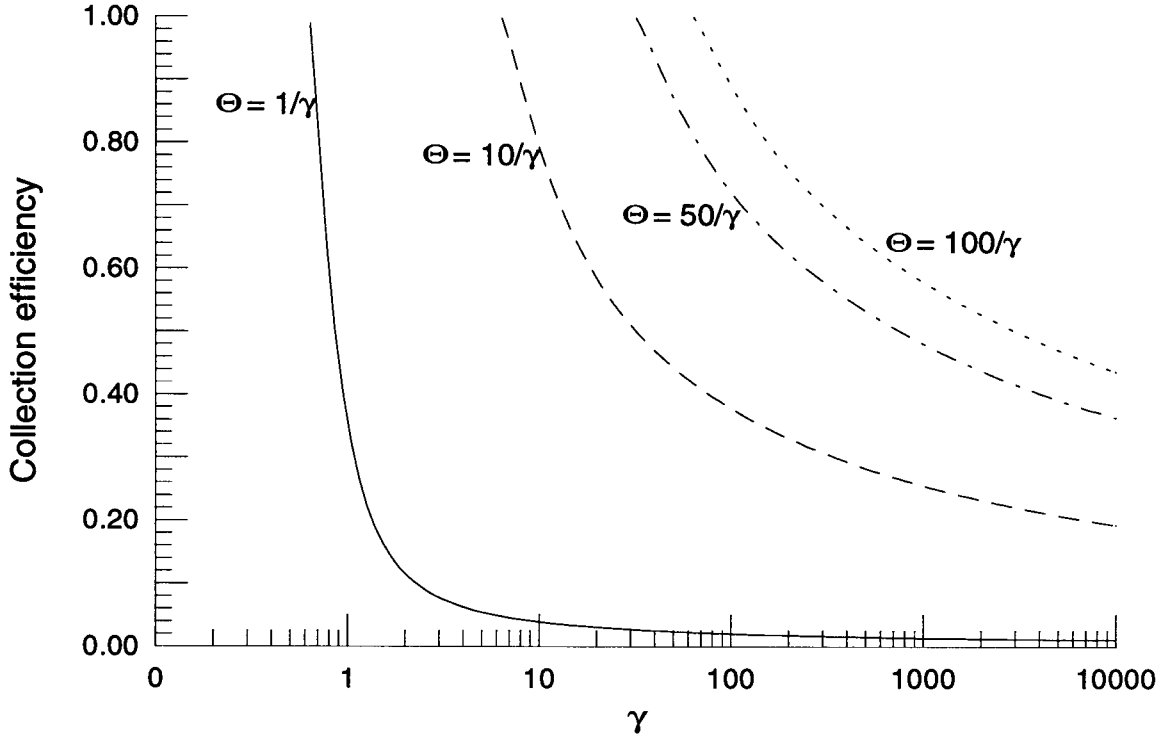
Figure 2.9: Collection efficiency as a function of electron energy γ for acceptance angles Θ as multiples of $1/\gamma$.

$$-2\beta(1-\cos\Theta)(1+\beta^2\cos^2\Theta)\bigg\}. \tag{2.17}$$

Consequently, when the acceptance angle is $\pi/2$, the total energy emitted becomes

$$\frac{\mathrm{d}\mathcal{E}}{\mathrm{d}\omega} = \int_0^{2\pi}\mathrm{d}\phi\int_0^{\pi/2}\frac{\mathrm{d}^2\mathcal{E}}{\mathrm{d}\omega\mathrm{d}\Omega}\sin\theta\,\mathrm{d}\theta$$

$$= \frac{e^2}{2\pi\beta c}\left[(1+\beta^2)\ln\left(\frac{1+\beta}{1-\beta}\right)-2\beta\right], \tag{2.18}$$

which only depends on the energy of the electron. The collection efficiency for the acceptance angle Θ is defined by the ratio of Eq. (2.17) to Eq. (2.18). For a relativistic electron ($\beta\approx 1$ and $\gamma\gg 1$), the energy collected is proportional to $\ln\gamma$ since $\frac{1}{1-\beta}\sim\gamma^2$ at this limit. This logarithmic dependence on electron energy is demonstrated in Fig. 2.8 for different acceptance angles. The dependence starts approximately at $\gamma\sim 1/\Theta$.
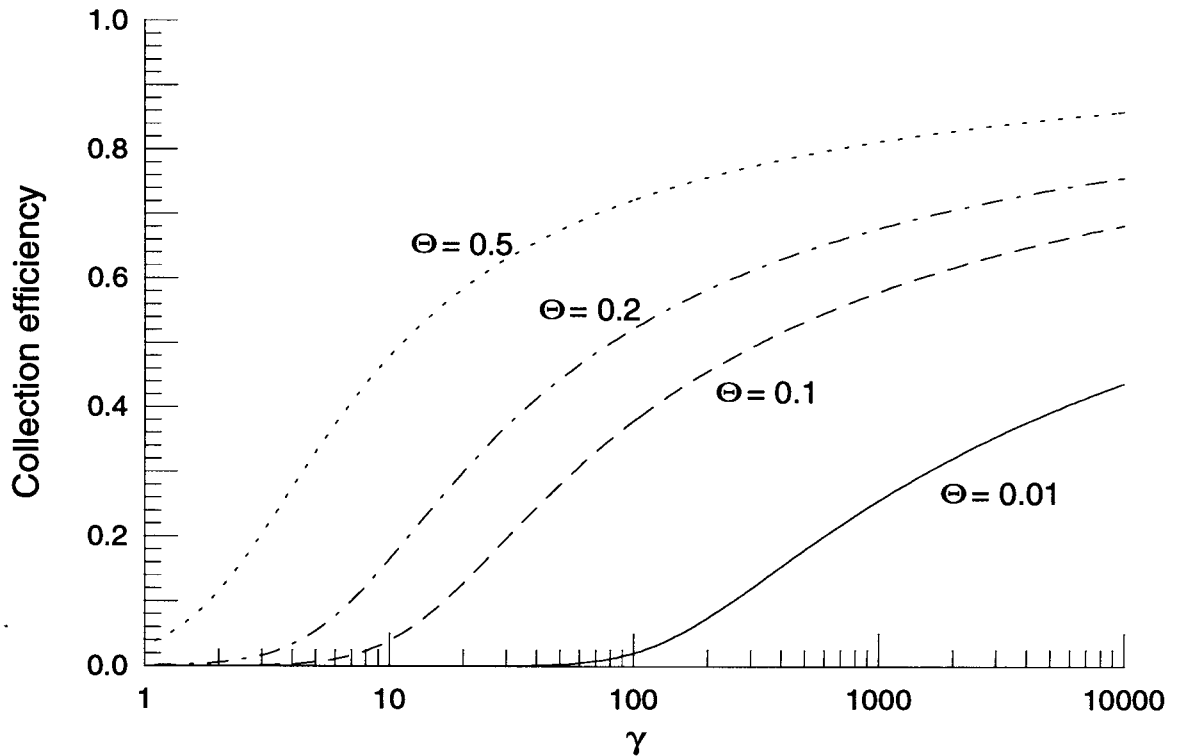
Figure 2.10: Collection efficiency as a function of electron energy γ for fixed acceptance angles Θ.

At first glance of Fig. 2.5, it seems to be reasonable to hypothesize that larger portions of radiation energy will be collimated into the $\Theta = 1/\gamma$ radiation cone at larger electron energy since the maximum energy density increases proportionally to γ^2. However, unlike synchrotron radiation, this collimation of energy into the forward direction at large electron energy is *not* true for transition radiation. Although the maximum increases like γ^2, the width of the cone reduces like $1/\gamma$. As a result, the angular integrated energy within a cone of $\Theta = 1/gamma$ is about a constant portion of the total radiated energy. As shown in Fig. 2.9, the collection efficiency within a $\Theta = 1/\gamma$ cone is about constant ($\sim 2\%$), and most of the energy ($\sim 98\%$) is located outside this cone for large electron energies ($\gamma \gg 10$). For smaller electron energies, the collection efficiency increases because the angle $\Theta = 1/\gamma$ is getting closer to $\pi/2$,
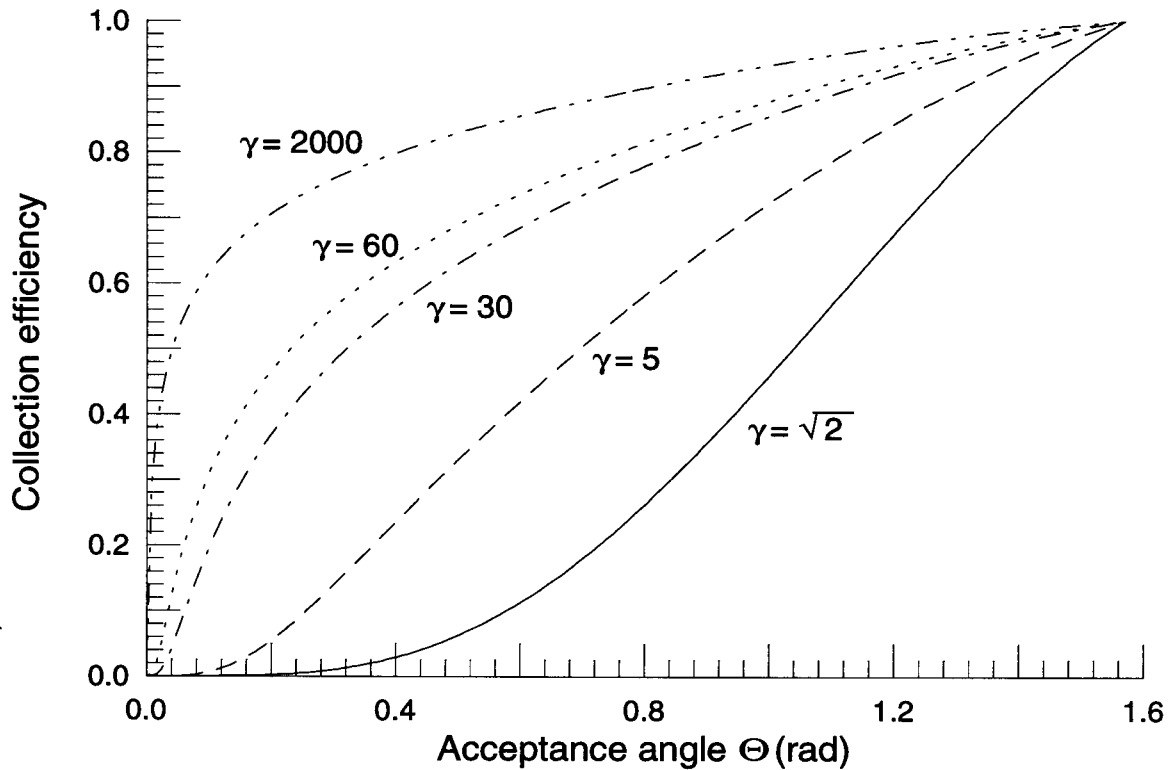
Figure 2.11: Collection efficiency as a function of acceptance angle Θ at different electron energies γ.

not the result of better collimation.

Since the radiated energy of transition radiation is not concentrated within an angle of, say, $1/\gamma$, it is worth investigating the collection efficiency for different acceptance angles and electron energies in order to design effective collection system of the radiation. The collection efficiency as a function of electron energy at fixed acceptance angles is shown in Fig. 2.10. The efficiency is negligible for electron energies γ smaller than about $1/\Theta$, where Θ is the acceptance angle. For γ greater than about $1/\Theta$, the efficiency starts to increase with electron energy, however, at very low rate. For example, for the acceptance angle as large as 0.5 rad, the collection efficiency is about 46% at $\gamma = 10$, 72% at $\gamma = 100$, and 85% at $\gamma = 10000$! On the

other hand, the collection efficiency as a function of acceptance angle for fixed electron energies is shown in Fig. 2.11. The dependence on the acceptance angle varies with electron energy. At smaller energy (say, $\gamma \leq 5$), the efficiency slowly increases with the acceptance angle; however, at larger energy (say, $\gamma \geq 30$), the efficiency first increases quickly as the acceptance angle increases, then slowly steps its way to full 100%. For example, at $\gamma = 60$, the collection efficiency is about 46% at acceptance angle $\Theta = 0.2\,\text{rad}$, 64% at $\Theta = 0.4\,\text{rad}$, 80% at $\Theta = 0.8\,\text{rad}$, and 92% at $\Theta = 1.2\,\text{rad}$.

2.2.3 The Polarization of Transition Radiation

Polarization of transition radiation is an important property of the radiation when considering the superposition of transition radiation from two or more radiation sources. Detailed descriptions of polarization components for normal and oblique incident cases have been discussed in Sec. 2.1.2. However, it would be useful if one can obtain intuition from a simple picture. In this section, we will discuss how to use the simplified picture described in Sec. 2.1.1 to derive the polarization components.

In the two-particle collision model introduced in Sec. 2.1.1 for the case that the electron is moving from vacuum into the conductor, the polarization of the radiating electric field emitted in the direction of $\hat{n}$ is, from Eq. (2.2), in the direction of $q_j\,\hat{n} \times (\hat{n} \times \beta_j^{\text{(initial)}})$ for the jth particle since $\beta_j^{\text{(final)}} = 0$. For the electron, we have $q_1 = -|e|$ and $\beta_1^{\text{(initial)}} = \beta$, and for its image charge, $q_2 = +|e|$ and $\beta_2^{\text{(initial)}} = -\beta$. Hence, the polarization of the radiating electric field is in the direction of $-\hat{n} \times (\hat{n} \times \beta)$ for the case of backward transition radiation. The sum of electric fields in all backward directions will produce an electric field for the deceleration of both charges. On the other hand, in the two-particle creation model in Sec. 2.1.1 for the case that the electron is moving from the conductor into vacuum, the polarization of the radiating electric field emitted in the direction of $\hat{n}$ is, from Eq. (2.2), in the direction of $-q_j\,\hat{n} \times (\hat{n} \times \beta_j^{\text{(final)}})$ for the jth particle since $\beta_j^{\text{(initial)}} = 0$. With appropriate conditions
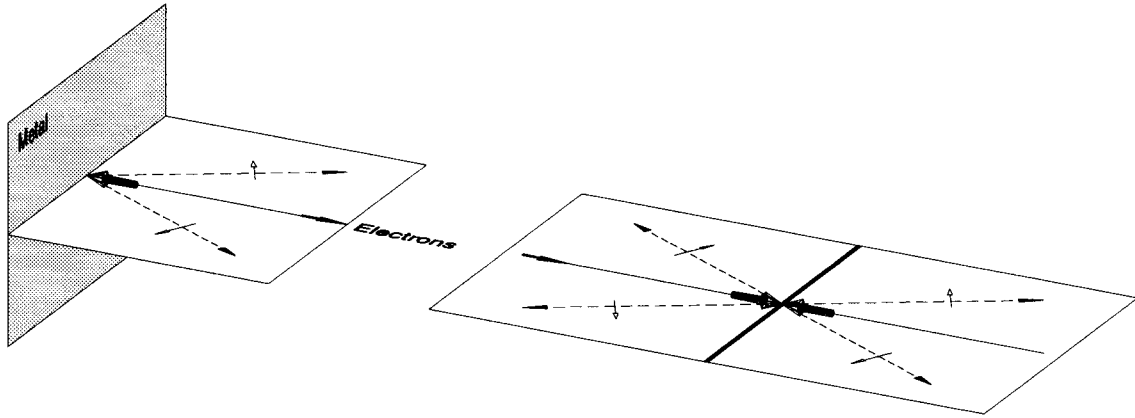
Figure 2.12: The polarization of transition radiation for normal incidence. The arrows with dashed line indicate the direction of the radiating rays. The hollow-headed arrows are the polarization components of the radiation. The three-dimensional solid arrows are the corresponding acceleration/deceleration electric fields acting on the electron. Bold arrows are the direction of the electron motion. Shown in the left is the relation between the radiation plane (white) and the metal surface (shaded). In the right, only the radiation plane is shown, and the metal is shown as a bold line.

for $\beta_j^{(\text{final})}$, the polarization of the radiating electric field is in the direction of $\hat{n} \times (\hat{n} \times \beta)$ for the case of forward transition radiation. The sum of electric fields in all forward directions will produce an electric field for the acceleration of both charges.

The polarization of transition radiation for the case of normal incidence is shown in Fig. 2.12. The radiation has only one component which is parallel to the radiation plane (shown as the white plane) because the acceleration/deceleration electric fields acting on the electron are in the plane. The polarization components for forward and backward transition radiation in the same radiation plane are mirror images of each other. The polarization components for all the radiation planes are symmetric about the axis of incidence (direction of the electron motion) for both forward and backward radiation. On the other hand, the polarization of the radiation for the oblique incident case shown in Fig. 2.13 has two components: parallel and perpendicular to the radiation plane. This is due to the fact that the acceleration/deceleration electric
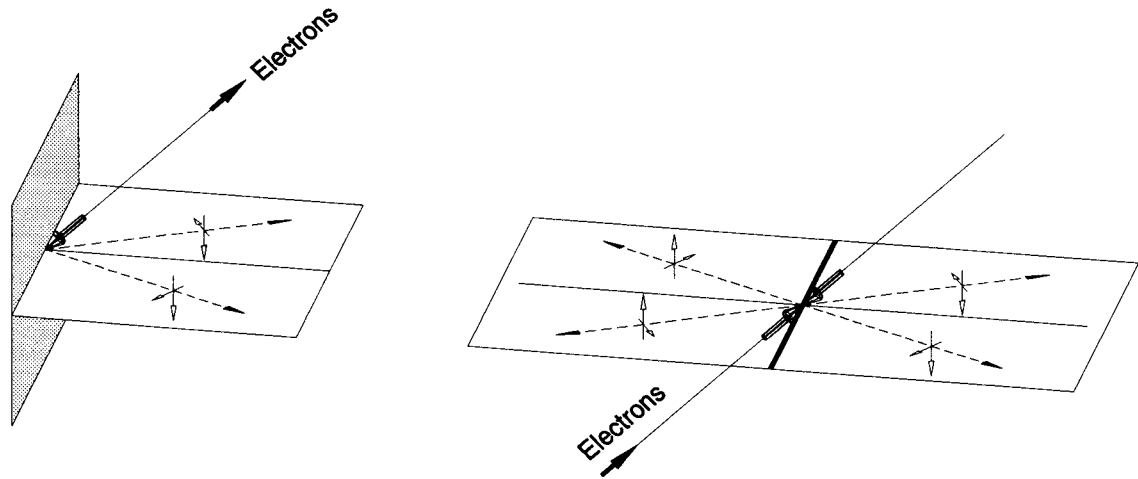
Figure 2.13: The polarization of transition radiation for oblique incidence. All the symbol are the same as those in Fig. 2.12.

fields acting on the electron are not in the plane. The polarization components for forward and backward transition radiation in the same radiation plane are, in this case, symmetric about the point of incidence, instead of mirror images. If the polarization components of all radiation planes are considered, the polarization vectors are actually symmetric about the direction of the electron motion (in the ψ direction as referred to Fig. 2.7) for the forward radiation and about the axis of "reflection" (in the $\pi - \psi$ direction as referred to Fig. 2.7) for the backward one.

2.3 Observation of Coherent Transition Radiation

Unlike synchrotron radiation, the production of transition radiation is not an unavoidable radiating process in accelerators, and there is no concern of electrons loosing energy through the emission of coherent transition radiation in accelerators since particles in accelerators will not encounter such radiating structure. Hence, the study of coherent transition radiation did not become an urgent and major interest in the

past. However, the study of incoherent transition radiation has become one of the major topics in the design of high-energy particle detectors historically[30].

2.3.1 Previous Observations

Ever since Ginsburg and Frank in 1946 predicted the production of transition radiation when charged particles pass through the interface of two media of different dielectric constants, most of the historical experiments were done to characterize incoherent transition radiation in the range from x-rays to visible lights[24]. These experiments showed very good agreement with transition radiation theory. The use of this radiation in different wavelength regimes has also been investigated. In the x-ray regime, transition radiation is used in particle detectors to measure the energy of particles through stacked transition radiators[31,32]. The possibility of using stacked radiators to produce intense x-rays for industrial use has also been studied[33]. In the visible-light regime, optical transition radiation is used to measure the transverse emittance of electron beams[34].

Although there were many theoretical papers and experimental reports on incoherent transition radiation in the past, the observation of coherent transition radiation has not been reported until recently when the accelerator technology became mature enough to produce short electron bunches, and the investigation of coherent radiation of different forms became a new and interesting direction in the field of accelerator physics. Following the success in the observation of coherent synchrotron radiation, coherent transition radiation became the next topic of interest to the groups who have observed coherent synchrotron radiation. In 1991, Happek *et al.* made the first observation of coherent transition radiation from about 2-mm-long electron bunches of 300 MeV energy at the Cornell Electron Storage Ring injector linac[35], and later in 1992 Shibata *et al.* also observed coherent transition radiation from 42-MeV electron
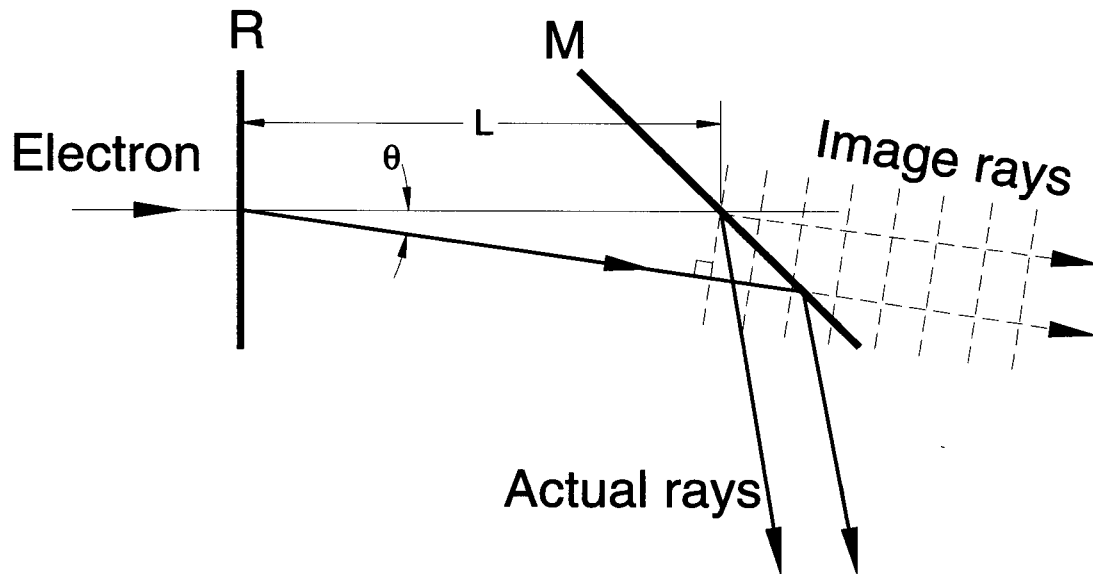
Figure 2.14: The "radiator-mirror" scheme for transition radiation designed to examine the "formation" of transition radiation; however, it actually examines the interference of the radiation from two transition radiators.

bunches at Kyoto University[36]. Both groups generated radiation in the millimeter-wave regime and confirmed the quadratic dependence of intensity on the beam current.

Interestingly, both experiments used the "radiator-mirror" scheme as shown in Fig. 2.14 to examine the "formation" of forward transition radiation. Introduced by early Russian theoreticians in the theory of transition radiation, "formation length" is the distance measured along the particle trajectory for which the phase difference between the forward transition radiation field and the particle self-field is just equal to one radian[31,32,34,37]. If one measures the total intensity (radiation field plus particle field) along the particle trajectory at a distance L away from the radiator, the interference term of the two fields will become negligible (i.e., two fields are incoherent) when L is much greater then the formation length Z_f defined as

$$Z_f = \frac{\beta c}{\omega(1 - \beta \cos \theta)},$$

(2.19)

where θ is the angle of the radiation with respect to the particle's direction. This only describes the interference of the radiation and the particle field; however, it does not imply any sort of distance necessary for transition radiation to be "formed." Researchers first designed this "radiator-mirror" scheme in the hope to use the mirror placed downstream of the radiator to obstruct the formation of transition radiation and reflect it for the observation of this formation process. This later was understood as the interference between the forward transition radiation emitted by the upstream radiator and the backward one emitted from the mirror. As shown in Fig. 2.14, the phase difference between the radiation emitted from the mirror (M) and the radiation emitted from the radiator (R) and, later, reflected by the mirror due to the optical path difference is

$$
\begin{aligned}
\phi &= \omega \left(\frac{L}{\beta c} - \frac{L \cos \theta}{c} \right) \\
&= \frac{\omega L (1 - \beta \cos \theta)}{\beta c} \\
&\equiv \frac{L}{Z},
\end{aligned} \tag{2.20}
$$

where L is the distance between the radiator and the mirror, θ is the angle between the radiation and the electron motion, and Z has the same expression as the formation length Z_f in Eq. (2.19). The coincidence of Z in this derivation and the formation length Z_f is due to the relative velocity between the radiation (traveling with speed c) and the particle (moving with speed $v = \beta c$). The total intensity measured from this scheme is the coherent sum of the two radiated electric fields

$$
\begin{aligned}
I &\propto \left| E_{\text{TR}}^{(\text{M})} + E_{\text{TR}}^{(\text{R})} \right|^2 \\
&= |E_{\text{TR}}|^2 |1 - e^{i\phi}|^2 \\
&= 2|E_{\text{TR}}|^2 \left[1 - \cos \left(\frac{L}{Z} \right) \right],
\end{aligned} \tag{2.21}
$$

where the minus sign for $E_{\text{TR}}^{(\text{R})}$ is the additional π phase shift due to reflection from the mirror. This is what the two groups have observed. No measurement on the
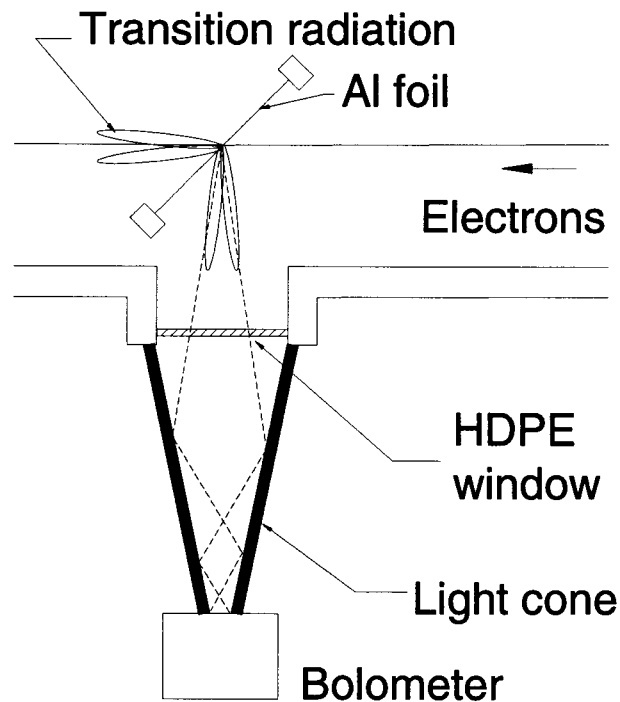
Figure 2.15: Experimental setup for coherent transition radiation measurements.

radiation emitted from a *single* radiator has been done in these experiments. In the experiments conducted at SUNSHINE discussed in the following section, this confusion was avoided by simply observing backward transition radiation.

2.3.2 Observation at SUNSHINE

After the observation of coherent synchrotron radiation at SUNSHINE which confirmed the generation of subpicosecond electron bunches, a more detailed study of backward coherent transition radiation emitted from a single radiator and the possibility to use this light generating process as a high-intensity far-infrared light source has been conducted here at Stanford University. Coherent transition radiation is generated when the 30-MeV electron beam of subpicosecond bunch length passes through

Coherent transition radiation
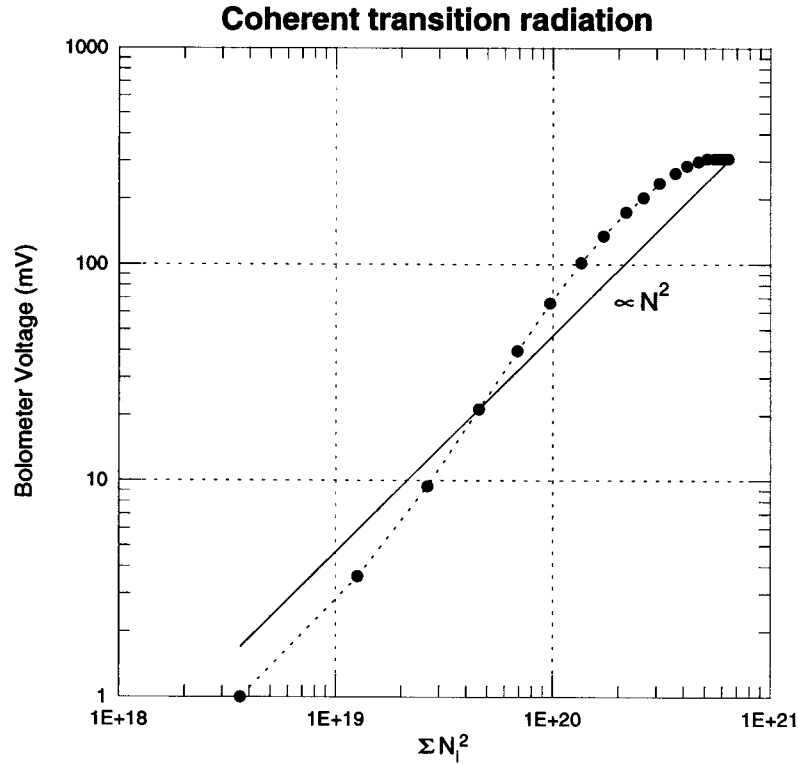
Figure 2.16: Bolometer signal of coherent transition radiation as a function of electron beam current.

a 25.4-μm-thick aluminum (Al) foil of 20 mm diameter shown in Fig. 2.15[16]. This foil supported by a copper ring using the drumhead stretching technique is oriented at a 45° angle to the beam direction so that backward transition radiation is emitted at a right angle to the electron direction and is extracted from vacuum into air through a 1.25-mm-thick high-density polyethylene (HDPE) window of 19 mm diameter and 87% transmission in the far-infrared regime. Adjacent to the downstream side of the aluminum foil is a screen coated with zinc sulfide (ZnS) to monitor and optimize the electron beam size as well as its position. This additional monitoring foil will not affect the measurement of backward transition radiation emitted from the radiator foil. A room-temperature pyroelectric bolometer collects the radiation emitted through the window and a copper light cone with an acceptance angle of $\Theta = 113$ mrad.

2.3.2.1   Quadratic Dependence on the Electron Current

In an analogy to coherent synchrotron radiation, the intensity of coherent transition radiation would be expected to scale with the square of the number of electrons in the bunch. This is verified by measuring the energy of the collected backward coherent transition radiation from each macro-pulse with the bolometer as a function of the electron beam current. As discussed in Sec. 1.3.2.1, the electron current is varied by closing the high energy filter in the alpha magnet to scrape off some electrons while keeping the low energy filter fixed. In this way, the effect on the electron bunch length is minimized. With the same reason described in Sec. 1.3.2.1, the measured bolometer signal is shown in Fig. 2.16[16] as a function of $\sum N_i^2$, which gives the closest approximation to the sum of the square of the number of electrons in each bunch. The measured intensity shows the expected quadratic dependence on the electron charges for almost 3 orders of magnitude. Small deviations from the ideal quadratic scaling are due to unavoidable variations of bunch length by the method of changing the electron beam current described in Sec. 1.3.2.1.

2.3.2.2   Total Energy Measurement

The total collected energy of coherent transition radiation from each macro-pulse is measured as[16]

$$382 \, \mu J \text{ per macro-pulse}$$

with an rms electron intensity of 3.08×10^8 electrons per bunch. This measurement has excluded the possibility of contributions from other sources such as wake fields, ionization radiation, and synchrotron radiation from upstream steering magnets[16]. In order to compare this result with theory, three factors have to be considered: the 87% transmission efficiency of the HDPE window, 36% collection efficiency through 113 mrad acceptance angle [cf., Eqs. (2.17), (2.18), and Fig. 2.11], and the varying

bunch length across the macro-pulse described in Sec. 1.3.2.2. When these factors are taken into account in the theoretical calculation and using Eqs. (1.10), (2.7), (2.10), and (2.15) with Table 2.1, and the assumption of Gaussian electron bunch distribution, the calculated total energy from a macro-pulse accepted by the bolometer with an overall 31% (= 36% × 87%) collection efficiency is[16]

$$487 \, \mu J \text{ per macro-pulse.}$$

This calculated result agrees with the measured one within a 22% difference. Calculations further indicates that the total radiation intensity is equivalent to that emitted from 2856 identical Gaussian electron bunches with equivalent bunch length of 0.483 ps and beam intensity of 3.08×10^8 electrons in each bunch. Each bunch radiates a total energy of about $0.544 \, \mu J$, and about $0.171 \, \mu J$ of the radiated energy is accepted by the bolometer through the HDPE window and the light cone.

2.4 Spectral Characterization and Bunch-length Measurements

The characterization of coherent transition radiation is closely related to the measurement of the electron bunch distribution, or equivalently the "bunch-length" measurement. Since the spectrum of coherent radiation from any radiating process is determined by both the Fourier transform of the bunch distribution and the intrinsic single-electron spectrum of the radiating process, the measurement of bunch distribution plays a very important role in the characterization of coherent radiation. Especially for transition radiation, the single-electron spectrum has no frequency dependence in the far-infrared regime. The spectrum of coherent transition radiation, hence, can be characterized by the bunch-length measurement. On the other hand, if the spectrum of coherent transition radiation is measured, the bunch distribution

can also be deduced from this frequency information.

2.4.1 Time-domain versus Frequency-domain Measurement

To measure the electron bunch length, it is intuitive to use a time-resolved method, which resolves the beam-generated signal in the time domain. However, when the bunch length is in the sub-picosecond regime, it is beyond the resolution of time-resolved methods developed so far. In addition, the complexity and the cost of hardware for fast time-resolved methods such as a streak camera increase to a great extent as the resolution approaches one picosecond. Therefore, it is necessary to develop a new bunch-length measuring technique with femtosecond resolving power.

As an alternative, a frequency-resolved technique extracts the frequency content of a beam-generated signal. From this frequency information, the particle distribution can be deduced. Unlike time-resolved techniques, it does not require fast processing speed and complex hardware. Since the necessary broad bandwidth required for short pulses can be achieved by optical methods, a subpicosecond time resolution can be obtained. This is a well-known technique in the characterization of femtosecond laser pulses[38] and has been suggested for subpicosecond bunch-length measurements[39]. The method utilizes a far-infrared Michelson interferometer to measure coherent transition radiation emitted at wavelengths longer than or equal to the bunch length via optical autocorrelation. The bunch length can be determined by analyzing the measured frequency information.

At the SUNSHINE facility, we have developed a new bunch-length measuring system based on this frequency-resolved method. Using subpicosecond electron pulses generated at SUNSHINE[16,17], we have verified this technique[17,18] and developed it into a simple, low-cost instrument for subpicosecond bunch-length measurement[40]. In the following sections, we will describe the principle of this autocorrelation technique, analysis and interpretation of bunch-length measurements, and experimental

results. Through this frequency-resolved bunch-length measurement, the spectrum of coherent transition radiation is characterized, which provides the foundation for the study of stimulated coherent transition radiation.

2.4.2   Remarks on the Bunch Form Factor

As described in Sec. 1.1.2, the most effective way to measure the longitudinal bunch distribution is through the measurement of coherent radiation emitted in the forward direction[1]. In this direction, the transverse bunch distribution does not contribute to the bunch form factor for an azimuthally symmetric beam. However, it is worth noticing that transition radiation does not produce radiation in the forward direction ($\theta = 0$). Hence, in order to use transition radiation to measure the bunch length, observing the radiation in an off-axis direction ($\theta \neq 0$) is necessary. In the case of an off-axis observation, the transverse bunch distribution will contribute to the form factor even for a transversely symmetric beam.

Minimizing transverse contribution is important for clean sub-picosecond bunch-length measurements. For example, for a Gaussian bunch distribution with equivalent length $\sqrt{2\pi}\,\sigma_z$ and equivalent diameter $\sqrt{2\pi}\,\sigma_\rho$ defined in Eqs. (1.18) and (1.23), the off-axis bunch form factor $f(\nu;\theta)$ in Eq. (1.24) shows an apparent equivalent length of $\sqrt{2\pi}\,(\sigma_z \cos\theta + \sigma_\rho \sin\theta)$ when the bunch is observed at an angle θ. In the forward direction ($\theta = 0$), the transverse contribution vanishes, and the equivalent length reduces to $\sqrt{2\pi}\,\sigma_z$. However, for large angles or big transverse beam sizes, the transverse contribution will result in an apparent bunch length measurement $[\sqrt{2\pi}\,(\sigma_z \cos\theta + \sigma_\rho \sin\theta)]$ that is longer than the actual one ($\sqrt{2\pi}\,\sigma_z$). This transverse

---

[1]The forward direction, here, refers to the direction of the axis of symmetry for the radiation. For a general oblique incident case as shown in Fig. 2.3, the forward direction is defined as the direction of electron motion (in the direction of ψ) for forward transition radiation, and the direction of "reflection" (in the direction of $\pi - \psi$) for backward transition radiation. In the following discussions, the angle θ is defined with respect to this forward direction.

contribution, however, can be ignored if the condition

$$\sigma_\rho \sin\theta \ll \sigma_z \cos\theta$$

or, equivalently,

$$\sigma_\rho \tan\theta \ll \sigma_z \qquad (2.22)$$

is satisfied. On the other hand, for a cylindrical slug of beam with radius σ_ρ and length $2\sigma_z$ defined in Eqs. (1.16) and (1.21), the transverse contribution can be ignored if the first lobe of $J_1(x)/x$ from the transverse contribution in Eq. (1.22) contains most part of $\sin(x)/x$ from the longitudinal contribution in the same equation. This condition can be expressed as

$$\nu_{\text{long}}^{(1)} = \frac{c}{2\sigma_z \cos\theta} \ll \nu_{\text{tran}}^{(1)} = \frac{c\alpha}{2\pi\sigma_\rho \sin\theta},$$

where $\nu_{\text{long}}^{(1)}$ is the frequency at the first zero of $\sin(x)/x$, and $\nu_{\text{tran}}^{(1)}$ is the frequency at the first zero of $J_1(x)/x$ with $J_1(\alpha \approx 3.8317) = 0$. It can be further simplified as

$$\pi\sigma_\rho \tan\theta/3.8317 \ll \sigma_z. \qquad (2.23)$$

Both conditions in Eqs. (2.22) and (2.23) show that small transverse beam size at the radiation source point is essential in reducing the transverse contribution. Such condition is assumed in the following analysis and is automatically obtained when the beam conditions are optimized in experiments. Hence, good focusing to produce small transverse beam size and a reasonable angular acceptance for the detector is crucial for accurate sub-picosecond bunch-length measurements.
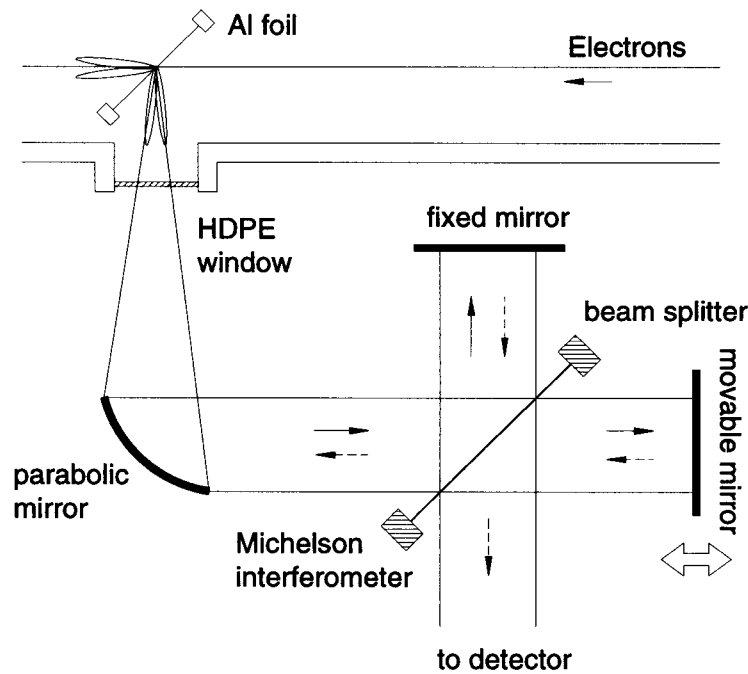
Figure 2.17: Schematic diagram of a Michelson interferometer designed for bunch-length measurement.

2.5 Autocorrelation Bunch-length Measuring Method

As a frequency-resolved method, this method uses a far-infrared Michelson interferometer to measure the spectrum of coherent transition radiation via optical autocorrelation. Coherent transition radiation emitted by electron pulses carries the information of bunch distribution in its frequency content. By analyzing the frequency information, the bunch length can be derived.

2.5.1 Michelson Interferometer

Since the spectrum of coherent transition radiation emitted by subpicosecond electron bunches is in the far-infrared regime, a far-infrared Michelson interferometer is used

to measure the spectrum via optical autocorrelation, and the bunch length can be deduced from the autocorrelation measurement. A Michelson interferometer used to measure the bunch length is shown schematically in Fig. 2.17. It consists of a beam splitter, a fixed and a movable mirror, and a detector. When light enters the Michelson interferometer, the beam splitter splits its amplitude into two mirror arms. As these two rays are reflected from the mirrors, they are recombined at the beam splitter and sent into the detector.

2.5.1.1 Working Principle

To see how this interferometer can be used to measure the bunch length, let us first assume the beam splitter is "ideal". An ideal beam splitter has constant amplitude reflection (R) and transmission (T) coefficients over all frequencies, which satisfy $|R|^2 = |T|^2 = 1/2$. As shown in Fig. 2.17, for an incoming light pulse of electric field E with intensity proportional to $|E|^2$, the light pulse split by the beam splitter and reflected by the fixed mirror has a field amplitude of $T(RE)$ when it reaches the detector; on the other hand, the light pulse reflected by the movable mirror has an amplitude of $R(TE)$ at the detector. Note that perfect reflection on the mirrors is assumed. At zero optical path difference, the pulses completely overlap at the detector, and the total intensity reaches the maximum $|R(TE) + T(RE)|^2 = 4|RT|^2|E|^2 = |E|^2$. All the incident energy goes into the detector. As the path difference increases but is still shorter than the bunch length, the two pulses overlap partially, and the total intensity decreases. Part of the incident energy now goes back to the source. When the path difference of two arms is larger than the bunch length, the two pulses are totally separated in time, and the resulting intensity at the detector is $|R(TE)|^2 + |T(RE)|^2 = 2|RT|^2|E|^2 = |E|^2/2$. Only half of the incident energy goes into the detector, while the other half goes back to the source. The intensity is constant over all path differences greater than the bunch length and is

called the *baseline*. The variation of intensity about the baseline as a function of optical path difference is defined as the *interferogram*. Therefore, the width of the peak in the interferogram can be used to estimate the bunch length.

2.5.1.2 Energy Conservation in the Interferometer

Since the interferometer does not produce radiation, the conservation of radiation energy is important. This energy conservation requirement, as we will see, implies a very important property of the beam splitter. To show this, let us assume the amplitude reflection and transmission coefficients at frequency ν are two complex quantities, i.e.,

$$R = |R|e^{i\theta_R} \tag{2.24}$$

$$T = |T|e^{i\theta_T}. \tag{2.25}$$

A lossless beam splitter will split the incident radiation energy into a reflected and a transmitted part, and energy conservation requires

$$|R|^2 + |T|^2 = 1. \tag{2.26}$$

As shown in Fig. 2.17 and stated in the previous section, the intensity going into the detector at zero path difference is $|R(TE) + T(RE)|^2$, while the intensity going back to the source at this point is $|T(TE) + R(RE)|^2$. The sum of these two intensity has to be equal to that of the incident radiation $|E|^2$; hence, it implies that

$$|2RT|^2 + |R^2 + T^2| = 1. \tag{2.27}$$

By expanding the above equation and using Eqs. (2.24), (2.25), and (2.26), we have

$$
\begin{aligned}
1 &= 4|R|^2|T|^2 + |R|^4 + |T|^4 + 2\operatorname{Re}(RT^*)^2 \\
&= 2|R|^2|T|^2 + (|R|^2 + |T|^2)^2 + 2\operatorname{Re}\left[|R|^2|T|^2 e^{2i(\theta_R - \theta_T)}\right] \\
&= 1 + 2|R|^2|T|^2\left[1 + \cos 2(\theta_R - \theta_T)\right].
\end{aligned}
\tag{2.28}
$$

Solving this equation, we obtain the following condition for energy conservation

$$\cos 2(\theta_R - \theta_T) = -1. \tag{2.29}$$

Therefore, the energy conservation requires that the angular difference between R and T should be an odd integral multiple of $\pi/2$, i.e.,

$$\theta_R - \theta_T = \frac{\pi}{2}(2m + 1), \tag{2.30}$$

where m is an integer.

On the other hand, if the beam splitter's amplitude reflection and transmission coefficients expressed in Eqs. (2.24) and (2.25) have the angular relation described in Eq. (2.30) at angular frequency $\omega = 2\pi\nu$, the sum of the intensity going into the detector and the source at path difference δ becomes

$$
\begin{aligned}
&\left| T(RE) + R(TE)e^{-i\omega\delta/c} \right|^2 + \left| R(RE) + T(TE)e^{-i\omega\delta/c} \right|^2 \\
&= 2|R|^2|T|^2|E|^2[1 + \cos(\omega\delta/c)] + |R|^4|E|^2 + |T|^4|E|^2 \\
&\quad + 2|R|^2|T|^2|E|^2 \cos(2\theta_R - 2\theta_T + \omega\delta/c) \\
&= (|R|^2 + |T|^2)^2|E|^2 + 2|R|^2|T|^2|E|^2\{\cos(\omega\delta/c) + \cos[(2m+1)\pi + \omega\delta/c]\} \\
&= |E|^2, \tag{2.31}
\end{aligned}
$$

where m is an integer. This is equal to the incident radiation energy. Hence, the angular requirement on the amplitude reflection and transmission coefficients of the beam splitter in Eq. (2.30) is a sufficient and necessary condition for energy conservation in the interferometer. This condition is met in the Michelson interferometer with a realistic beam splitter as will be discussed in Sec. 2.5.2.

2.5.1.3 The Interferogram and the Form Factor

The interferogram is obtained by measuring the detector signal as a function of the path difference in the two arms. The measured energy of the recombined radiation

pulses at the detector can be expressed in the time domain with an additional time delay δ/c for the movable arm as

$$
\begin{aligned}
I(\delta) &\propto \int_{-\infty}^{+\infty} \left| TRE(t) + RTE(t + \frac{\delta}{c}) \right|^2 dt \\
&= 2|RT|^2 \operatorname{Re} \int_{-\infty}^{+\infty} E(t)E^*(t + \frac{\delta}{c})dt + 2|RT|^2 \int_{-\infty}^{+\infty} |E(t)|^2 \, dt, \quad (2.32)
\end{aligned}
$$

where δ is the optical path difference and c the speed of light. Alternatively, a similar expression can be obtained in the frequency domain by adding an extra phase difference $e^{-i\omega\delta/c}$ to the radiation from the movable arm at angular frequency $\omega = 2\pi\nu$. Thus, the total energy measured at the detector is expressed as

$$
\begin{aligned}
I(\delta) &\propto \int_{-\infty}^{+\infty} \left| TR\tilde{E}(\omega) + RT\tilde{E}(\omega)e^{-i\omega\delta/c} \right|^2 d\omega \\
&= 2\operatorname{Re} \int_{-\infty}^{+\infty} |RT|^2 |\tilde{E}(\omega)|^2 e^{-i\omega\delta/c} d\omega + 2 \int_{-\infty}^{+\infty} |RT|^2 |\tilde{E}(\omega)|^2 d\omega, \quad (2.33)
\end{aligned}
$$

Although the two expressions for $I(\delta)$ in Eqs. (2.32) and (2.33) look different, they are related by the Fourier transform

$$
\tilde{E}(\omega) = \frac{1}{\sqrt{2\pi}} \int_{-\infty}^{+\infty} E(t)e^{i\omega t}dt. \quad (2.34)
$$

The baseline is defined as the intensity at $\delta \to \pm\infty$, where the two pulses are totally separated; hence, we have

$$
I_\infty \propto \begin{cases} 2|RT|^2 \int_{-\infty}^{+\infty} |E(t)|^2 dt & \text{(time domain)}, \\ 2 \int_{-\infty}^{+\infty} |RT|^2 |\tilde{E}(\omega)|^2 d\omega & \text{(frequency domain)}. \end{cases} \quad (2.35)
$$

By definition, the interferogram can be written as

$$
\begin{aligned}
S(\delta) &= I(\delta) - I_\infty \\
&\propto \begin{cases} 2|RT|^2 \operatorname{Re} \int_{-\infty}^{+\infty} E(t)E^*(t + \frac{\delta}{c})dt & \text{(time domain)}, \\ 2\operatorname{Re} \int_{-\infty}^{+\infty} |RT|^2 |\tilde{E}(\omega)|^2 e^{-i\omega\delta/c} d\omega & \text{(frequency domain)}. \end{cases} \quad (2.36)
\end{aligned}
$$

Therefore, the interferogram $S(\delta)$ is the autocorrelation of the incident light pulse (cf., the time domain part), and its Fourier transform is the power spectrum of the pulse (cf., the frequency domain part). Solving for $|\tilde{E}(\omega)|^2$ in Eq. (2.36) yields

$$|\tilde{E}(\omega)|^2 \propto \frac{1}{4\pi c |RT|^2} \int_{-\infty}^{+\infty} S(\delta) e^{i\omega\delta/c} \mathrm{d}\delta, \tag{2.37}$$

where $|\tilde{E}(\omega)|^2 = |\tilde{E}(-\omega)|^2$ since $E(t)$ is a real function. Using Eq. (1.10) and the relation $I_{\text{total}}(\nu) \propto |\tilde{E}(2\pi\nu))|^2$, the bunch form factor can be obtained from

$$f(\nu; \hat{n}) \propto \frac{1}{N-1} \left[\frac{1}{4\pi c |RT|^2 N I_e(\nu)} \int_{-\infty}^{+\infty} S(\delta) e^{i2\pi\nu\delta/c} \mathrm{d}\delta - 1 \right], \tag{2.38}$$

Hence, the interferogram contains the frequency spectrum of coherent transition radiation and can be used to derive the bunch length.

2.5.1.4 Examples

To demonstrate how the width of the interferogram can be used to derive the bunch length, let us consider the following examples with an ideal beam splitter in the Michelson interferometer. The transverse bunch contribution is also assumed to be negligible when compared to the longitudinal bunch contribution. From the time domain part of Eq. (2.36), the interferogram is proportional to the autocorrelation of the shape of the light pulse, which is the same as the longitudinal bunch distribution. Hence, the interferogram is directly related to the autocorrelation of the longitudinal bunch distribution.

For example, for a rectangular bunch of length $2\sigma_z$ with the longitudinal bunch distribution defined as Eq. (1.16), the interferogram can be expressed as

$$
\begin{aligned}
S(\delta) \;\propto\; & \int_{-\infty}^{+\infty} h(z) h^*(z + \delta) \mathrm{d}z \\
= \; & \begin{cases} \left(\int_{-\sigma_z}^{\sigma_z} - \int_0^\delta \right) \left(\frac{1}{2\sigma_z} \right)^2 \mathrm{d}z & \text{for } |\delta| \le \sigma_z \\ 0 & \text{otherwise} \end{cases}
\end{aligned}
$$
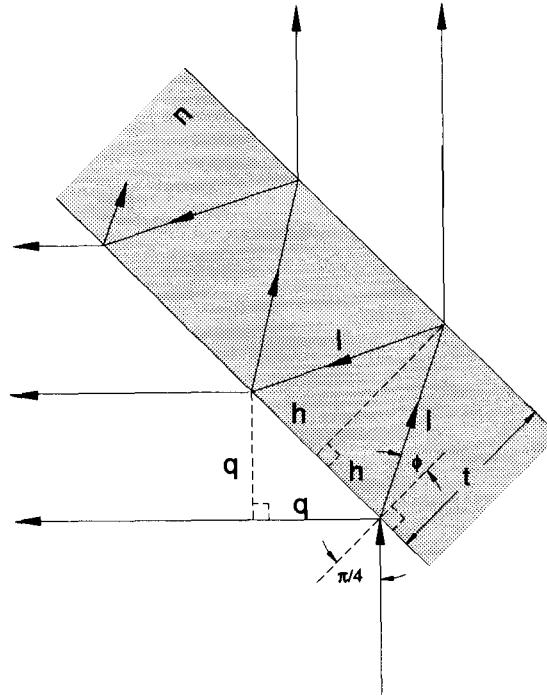
Figure 2.18: The interference of the Mylar beam splitter.

$$= \begin{cases} \dfrac{1}{2\sigma_z}\left(1 - \dfrac{|\delta|}{2\sigma_z}\right) & \text{for } |\delta| \leq \sigma_z \\ 0 & \text{otherwise} \end{cases} \qquad (2.39)$$

The full width at half maximum (FWHM) of the interferogram is calculated as $2\sigma_z$. Hence, the bunch length is equal to the FWHM of the interferogram for a rectangular bunch distribution. As the second example, for a Gaussian bunch distribution of equivalent bunch length $\sqrt{2\pi}\,\sigma_z$ with longitudinal bunch distribution defined by Eq. (1.18), the interferogram becomes

$$\begin{aligned} S(\delta) &\propto \int_{-\infty}^{+\infty} h(z)h^*(z+\delta)\mathrm{d}z \\ &= \frac{1}{2\pi\sigma_z^2}\int_{-\infty}^{+\infty} e^{-[z^2+(z+\delta)^2]/2\sigma_z^2}\,\mathrm{d}z \\ &= \frac{1}{2\sqrt{\pi}}e^{-\delta/4\sigma_z^2}. \end{aligned} \qquad (2.40)$$

The FWHM of this Gaussian interferogram is $4\sqrt{\ln 2}\,\sigma_z$. Therefore, the equivalent bunch length for a Gaussian bunch distribution is $\sqrt{\pi/8\ln 2} \approx 0.7527$ times the interferogram FWHM. Thus, the two examples give the following results:

$$\frac{\text{Equivalent Bunch Length}}{\text{Interferogram FWHM}} = \begin{cases} 1, & \text{for a rectangular bunch} \\ 0.7527, & \text{for a Gaussian bunch} \end{cases} . \qquad (2.41)$$

2.5.2 Beam-splitter Interference Effects

So far, the above discussions are based on the assumption that the reflectance and transmittance of the beam splitter is constant for all frequencies. Unfortunately, suitable beam splitters used in the far-infrared regime (a Mylar foil in our design) do not provide constant and equal reflectance and transmittance for all frequencies. This departure from an ideal beam splitter is caused by the interference of light reflected from both surfaces of the beam splitter shown in Fig. 2.18, which is equivalent to thin-film interference in optics[12, Sec. 9.7] with multiple reflection and transmission.

According to the design of the Michelson interferometer in Fig. 2.17, the beam splitter, which is a Mylar foil of thickness t and refractive index n, is mounted at a $45°$ angle to the direction of incoming light as shown in Fig. 2.18. The phase difference between the two adjacent parallel reflecting (or similarly, transmitting) rays due to the difference in optical path at angular frequency $\omega = 2\pi\nu$, when referred to the geometry in Fig. 2.18, is expressed as

$$\begin{aligned} \psi &= \omega\left(\frac{2l}{c/n} - \frac{q}{c}\right) \\ &= (2nl - q)\frac{\omega}{c}, \end{aligned} \qquad (2.42)$$

where c is the speed of light in vacuum. Snell's law gives for this geometry

$$n\sin\phi = \frac{1}{\sqrt{2}}, \qquad (2.43)$$

and solving for l and q in terms of t, we have[41]

$$l = nq$$
$$q = t \left(n^2 - \frac{1}{2} \right)^{-1/2}.$$

Hence, the phase factor for the optical path difference becomes

$$
\begin{aligned}
e^{i\psi} &= e^{i2t(\omega/c)\sqrt{n^2 - (1/2)}} \\
&= e^{i4\pi t\sigma\sqrt{n^2 - (1/2)}},
\end{aligned}
\tag{2.44}
$$

where $\sigma \equiv 1/\lambda = \nu/c$ is the wavenumber at frequency ν (and wavelength λ).

The total amplitude reflection coefficient for the foil with multiple reflection is expressed as[42]

$$R = r_1 + t_2 r_2 t_1 e^{i\psi} + t_2 r_2^3 t_1 e^{i\psi} + t_2 r_2^5 t_1 e^{i\psi} + \cdots, \tag{2.45}$$

where ψ is defined in Eq. (2.44), r_1 and t_1 are the amplitude reflection and transmission coefficients of the air-to-Mylar interface at an incident angle of $45°$, and r_2 and t_2 are the amplitude reflection and transmission coefficients of the Mylar-to-air interface at an incident angle ϕ defined in Eq. (2.43). The four quantities r_1, t_1, r_2, and t_2 are related by the Stokes relations[12, Sec. 4.5]:

$$r_2 = -r_1 \tag{2.46}$$

$$t_1 t_2 = 1 - r_1^2. \tag{2.47}$$

Using Stokes relations and summing over the infinite power series, the total amplitude reflection coefficient becomes

$$R = -|r_1| \frac{1 - e^{i\psi}}{1 - r_1^2 e^{i\psi}}. \tag{2.48}$$

The total phase of the reflected wave can be expressed, from the polar form of Eq. (2.48), as

$$\theta_R = \pi - \tan^{-1} \left[\frac{(1 - r_1^2)\cos(\psi/2)}{(1 + r_1^2)\sin(\psi/2)} \right]. \tag{2.49}$$

No absorption in the foil is assumed, and the refractive index is assumed to be constant ($n = 1.85$) over all frequencies of interest[41]. Similarly, the total amplitude transmission coefficient for the same condition is[42]

$$
\begin{aligned}
T &= t_2 t_1 e^{i\psi/2} + t_2 r_2^2 t_1 e^{i3\psi/2} + t_2 r_2^4 t_1 e^{i5\psi/2} + \cdots \\
&= (1 - r_1^2) \frac{e^{i\psi/2}}{1 - r_1^2 e^{i\psi}}.
\end{aligned}
\tag{2.50}
$$

Hence, the total phase of the transmitted wave is expressed as

$$
\theta_T = \tan^{-1} \left[\frac{(1 + r_1^2) \sin(\psi/2)}{(1 - r_1^2) \cos(\psi/2)} \right].
\tag{2.51}
$$

The phase difference between R and T, using the relation $\tan^{-1} A + \tan^{-1}(1/A) = (2m + 1)\pi/2$ for m as an integer, can be obtained from Eqs. (2.49) and (2.51) as

$$
\begin{aligned}
\theta_R - \theta_T &= \pi - \tan^{-1} \left[\frac{(1 - r_1^2) \cos(\psi/2)}{(1 + r_1^2) \sin(\psi/2)} \right] - \tan^{-1} \left[\frac{(1 + r_1^2) \sin(\psi/2)}{(1 - r_1^2) \cos(\psi/2)} \right] \\
&= \pi - (2m + 1)\frac{\pi}{2} \\
&= [2(-m) + 1]\frac{\pi}{2},
\end{aligned}
\tag{2.52}
$$

where m is an integer. Hence, the phase difference between R and T is an odd integral multiple of $\pi/2$ for all frequencies. In addition, it is straight forward to show $|R|^2 + |T|^2 = 1$ for all frequencies. This result is consistent with energy conservation in the interferometer as required from the discussions in Sec. 2.5.1.2.

It is worth noticing that r_1 is different for parallel and perpendicular polarization components; however, the above results are valid for both components. The corresponding r_1's for parallel and perpendicular polarization at a 45° incident angle, using Eq. (2.43), are[12, Sec. 4.3]

$$
r_1^{\parallel} = \frac{n^2 - \sqrt{2n^2 - 1}}{n^2 + \sqrt{2n^2 - 1}}
\tag{2.53}
$$

$$
r_1^{\perp} = \frac{1 - \sqrt{2n^2 - 1}}{1 + \sqrt{2n^2 - 1}},
\tag{2.54}
$$
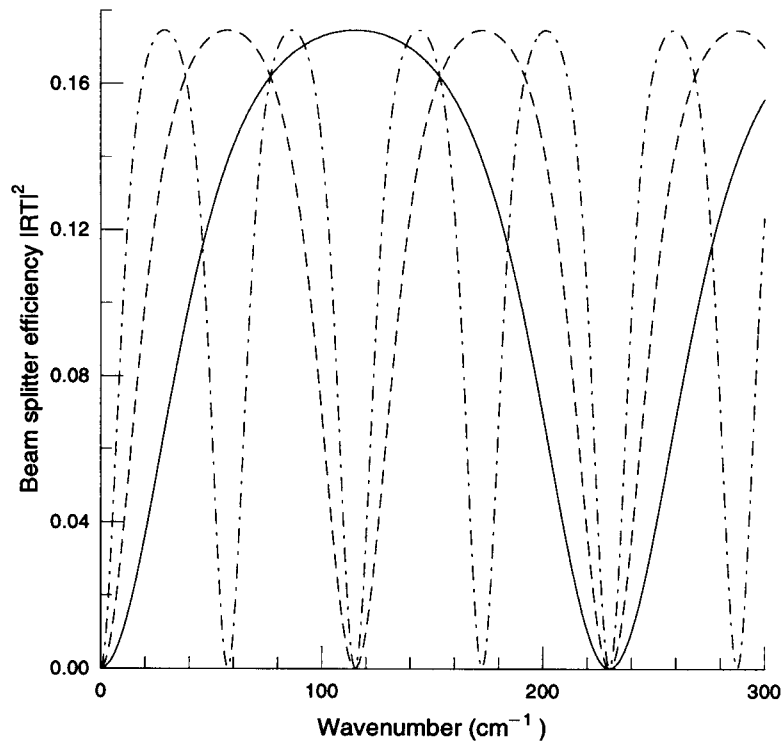
Figure 2.19: The efficiency of a Mylar beam splitter as a function of frequency for different thicknesses: 12.7 (solid), 25.4 (dashed), and 50.8 μm (dash-dotted line) for unpolarized light.

respectively. Hence, it is necessary to consider the effects of corresponding R and T (i.e., $R^{\parallel}$, $R^{\perp}$, $T^{\parallel}$ and $T^{\perp}$) for both polarization components of the light.

The efficiency of the beam splitter defined as $|RT|^2$ is shown in Fig. 2.19 for some typical thicknesses for unpolarized light [i.e., $(|R^{\parallel}T^{\parallel}|^2 + |R^{\perp}T^{\perp}|^2)/2$ is shown]. Unlike the ideal beam splitter, the efficiency is not constant over all frequencies and becomes zero at certain frequencies where light reflected from both surfaces of the beam splitter interferes destructively. Equations in the time domain such as Eq. (2.32) are no longer valid for the case of varying efficiency and need to be replaced by appropriate convolution integrals; however, equations in the frequency domain like Eq. (2.33) still hold. The width of the interferogram can not be directly used for bunch-length estimation as discussed in the previous section unless the correction for interference

effects on the interferogram are included.

2.5.3   Bunch-length Analysis

Although the interference effects on the interferogram caused by the complex reflec-
tion and transmission coefficients of the beam splitter do not seem to have simple
analytical forms, these effects can be included numerically for known bunch distri-
butions, and the bunch length can be derived from this analysis. Both Gaussian
and rectangular bunch distributions are currently used in this study. While most real
bunch distributions are neither Gaussian nor rectangular, the bunch lengths estimated
from the two distributions will give reasonable bounds for the real one.

The beam-splitter-affected interferogram can be obtained numerically by using the
spectrum of a known bunch distribution and Eqs. (2.33), (2.48), and (2.50). Some
numerical results of the beam-splitter interference effects for a rectangular bunch
distribution are shown in Fig. 2.20. For an ideal beam splitter, the interferogram
is non-negative and has the expected triangular peak with its FWHM equal to the
bunch length [cf., Fig. 2.20(a)]. For Mylar beam splitters, negative valleys appear in
the interferograms, which are due to suppression of the low frequency area by the first
zero of the beam-splitter efficiency. These valleys move closer to the main peak as
the beam-splitter thickness (t) decreases [cf., Fig. 2.20(b)–(d)]. For very thin beam
splitters [thinner than about half the equivalent bunch length (l_b)], they merge with
the main peak and make the peak narrower [cf., Fig. 2.20(d)]. The effects are similar
for a Gaussian distribution.

Detailed results on how the FWHM values in the interferogram change with the
equivalent bunch length for both Gaussian and rectangular distributions are shown
in Fig. 2.21 for different Mylar beam-splitter thicknesses. The raggedness of the lines
for the rectangular distribution is due to the high-frequency lobes of the sinc func-
tion. In contrast, the Gaussian distribution has a smoother variation of the frequency
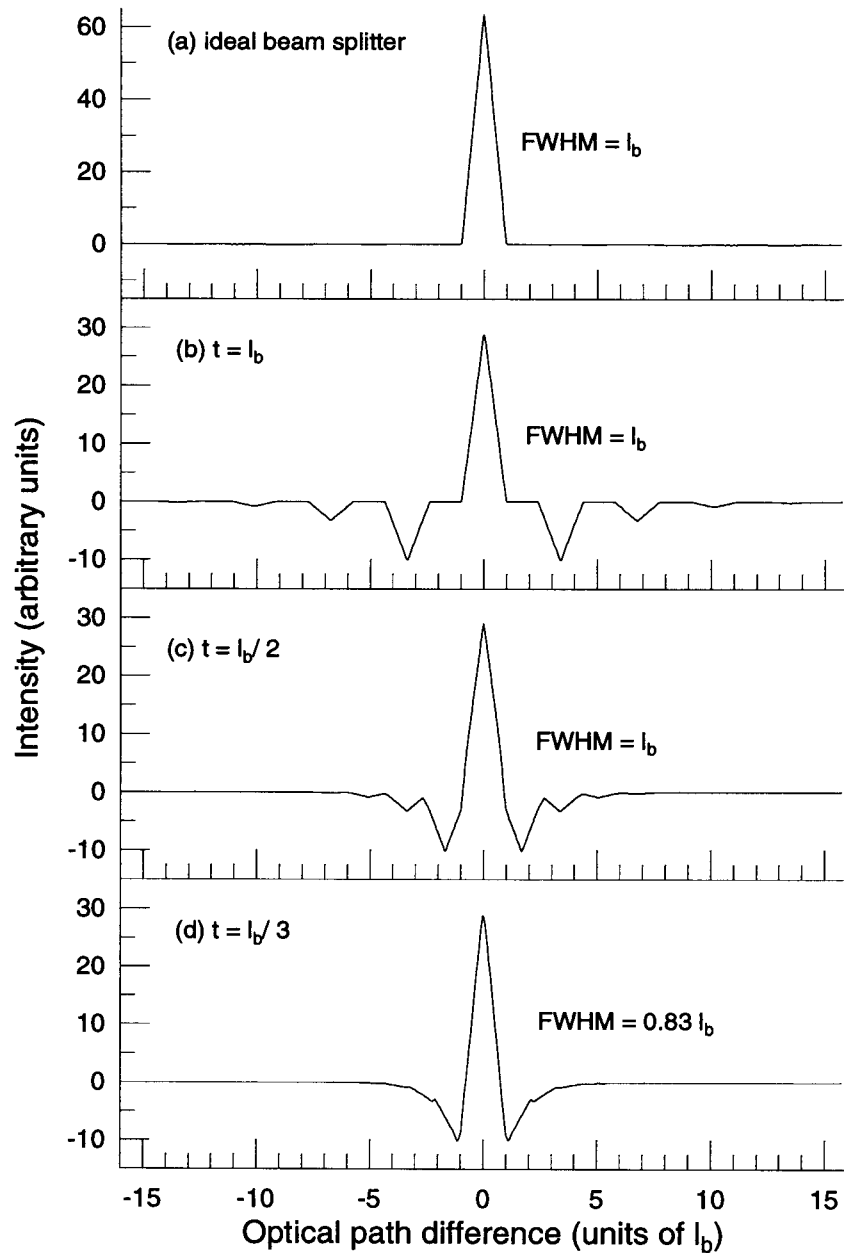
Figure 2.20: The simulation of the beam-splitter interference effects on a rectangular bunch distribution with different beam splitters: (a) an ideal beam splitter and Mylar beam splitters of thicknesses (t) (b) equal to, (c) half, and (d) one third of the equivalent bunch length (l_b).
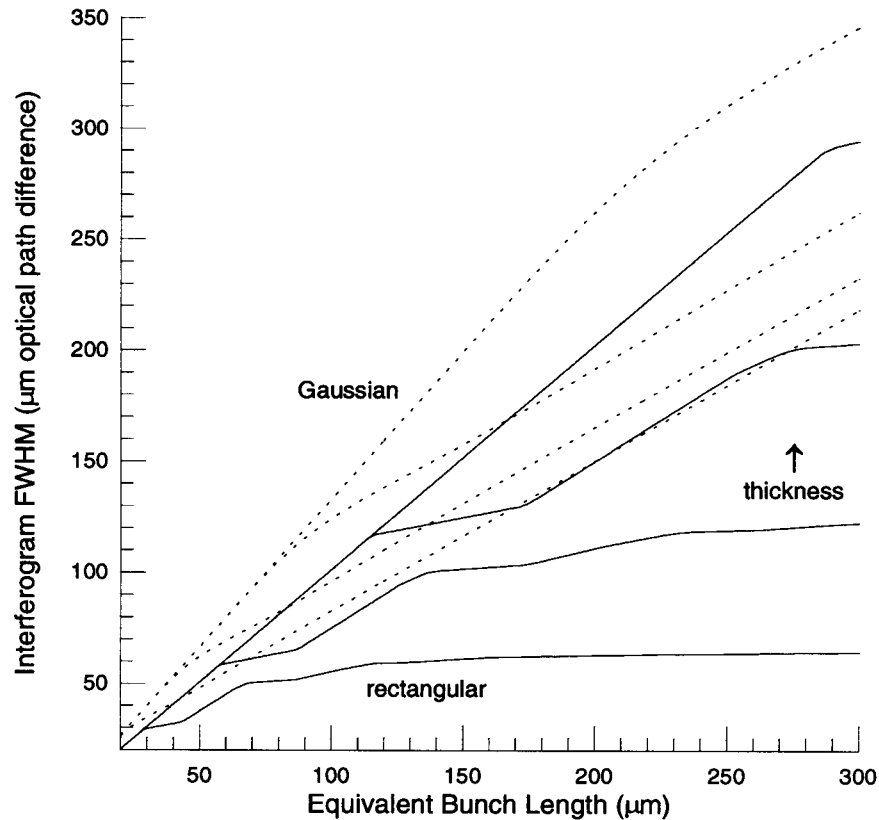
Figure 2.21: Interferogram FWHM's as functions of equivalent bunch lengths of both Gaussian (dotted) and rectangular (solid lines) bunch distributions for different Mylar beam-splitter thicknesses: 12.7, 25.4, 50.8, and 127 μm. Within the same distribution, the lines are shown from the bottom to the top in the increasing order of thickness.

spectrum, and the resulting slopes of the lines are smoother. When the equivalent bunch length is shorter than about twice the beam-splitter thickness, the valleys in the interferogram are separated from the main peak, and the relation between the interferogram FWHM and the equivalent bunch length is the same as that for the ideal beam splitter in Eq. (2.41). The slopes of the lines become unity for the rectangular distribution and about 1/0.75 for the Gaussian one. As the equivalent bunch length becomes greater than about twice the beam-splitter thickness, the valleys cut into the main peak and narrow its width. This peak-narrowing effect reduces the slopes of the lines for the rectangular distribution at longer bunch lengths and, hence, makes the

interferogram width less sensitive to the bunch-length change and increases the estimated range of the bunch length. Therefore, a Mylar beam splitter with a thickness matched to the expected range of the bunch length is important for effective bunch-length measurement. As indicated in Fig. 2.21, thicker beam splitters are preferable for bunch-length measurement. However, the absorption of thicker beam splitters will, at some point, reduce the signal level and pose a constraint on the selection of the thickness. Once the beam splitter is chosen, the bunch length can be derived from the measured interferogram width with the help of Fig. 2.21.

2.6 Bunch-length Measurements

As discussed in previous sections, the theoretical part of this new bunch-length measuring method shows promise of being a useful particle beam instrument in accelerators. To verify this theory, such an interferometer, as shown in Fig. 2.17, has been assembled and tested at the SUNSHINE facility to characterize its subpicosecond electron bunches.

2.6.1 Experimental Setup

For this experiment, the SUNSHINE facility was operated to produce 1-μs-long electron macro-pulses at 10 Hz containing a train of about 3000 electron bunches at an energy of 30 MeV. Each bunch had about 3.5×10^7 electrons. The bunch length is to be determined by this autocorrelation method. As shown in Fig. 2.17, transition radiation is generated when the electrons pass through a 25.4-μm-thick aluminum (Al) foil. The foil supported by a copper ring using the drumhead stretching technique is oriented at a 45° angle to the beam direction so that backward transition radiation is emitted in the direction normal to the beam path and can easily be extracted from the evacuated beam line into air via a 1-mm-thick high-density polyethylene (HDPE)

window of 19 mm diameter. Since backward transition radiation is emitted at the aluminum surface, the focal point of an off-axis paraboloidal mirror is aligned with this surface to convert the divergent radiation into parallel light without introducing extra optical path difference at different angles to the extracted light pulse. The parallel light then enters a far-infrared Michelson interferometer.

The interferometer consists of a Mylar beam splitter supported by an aluminum ring using the drumhead stretching technique, a fixed and a movable first-surface mirror, and a room-temperature detector. The beam splitter is mounted at a 45° angle to the direction of incident parallel light. There are four beam splitter thicknesses used in the experiment: 12.7, 25.4, 50.8, and 127 μm mounted on different aluminum rings exchangeable in the experiment. The movable mirror is moved by a Newport 850-B linear actuator, which is controlled by a Newport PMC200-P motion controller and commanded by a 486-based PC through a GPIB interface. The detector described in Sec. 1.2.2 is attached to a copper light-cone[21], which funnels the light into the detector. The detector signal is digitized into the computer through a National Instrument AT-MIO-16F-5 data acquisition board. With the computer interfaces, the autocorrelation measurements are performed automatically through the program under the LabVIEW control environment implemented on the computer.

2.6.2 Results

It has been confirmed in the previous experiment[16] discussed in Sec. 2.3.2.1 that backward transition radiation emitted by the electron pulses generated at SUNSHINE is coherent. Therefore, the spectrum measured by the autocorrelation method contains the information of the bunch distribution and can be used to derive the bunch length. By recording the detector signal as a function of the position of the movable mirror via the computer program, a typical 16-mm-long autocorrelation scan with 10-μm mirror step size using a 12.7-μm-thick beam splitter was measured as shown
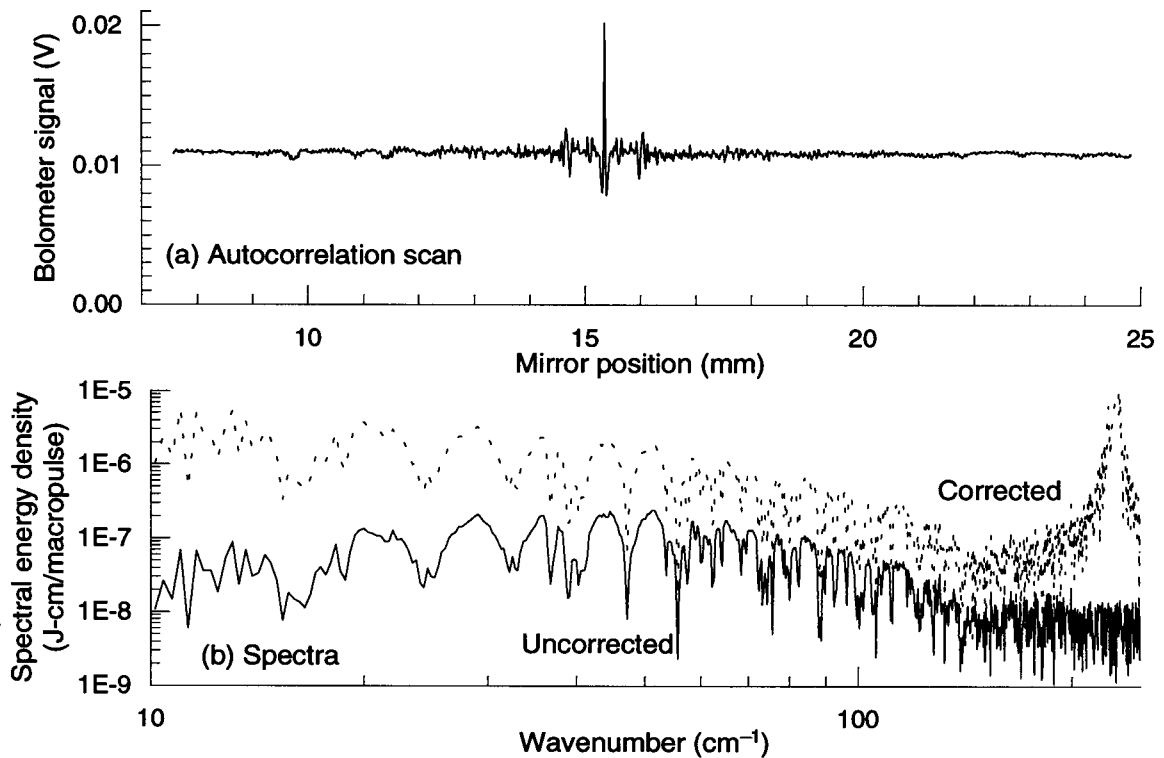
Figure 2.22: Typical 16-mm-long autocorrelation scan and derived spectra for the radiation from subpicosecond electron pulses. The autocorrelation scan is shown in (a). The raw spectrum and the one corrected for the Mylar beamsplitter efficiency are shown in (b). The spectral resolution is $0.3125\,\mathrm{cm}^{-1}$.

in Fig. 2.22 for the characterization of the spectrum of coherent transition radiation. The raw (uncorrected) spectrum as calculated with Eq. (2.37) from this interferogram and the spectrum after correction for the Mylar beamsplitter efficiency are also shown in the same figure. The total 16-mm mirror movement corresponding to 32-mm optical path difference results in a spectral resolution of $0.3125\,\mathrm{cm}^{-1}$. Below $10\,\mathrm{cm}^{-1}$, the spectra are believed to be contaminated by slow drifts of machine parameters during the half-hour measurement. The whole raw spectrum is well contained within the frequency range up to the second zero of the beamsplitter located at wavenumber $\sigma = 230\,\mathrm{cm}^{-1}$. The spike around the second zero of the beamsplitter in the corrected

spectrum is an artifact resulting from a large over-correction due to poor signal-to-noise ratios in this spectral range. The roll-off rate of the corrected spectrum at high frequency is closer to that of a rectangular distribution rather than that of a Gaussian distribution. The multitude of absorption lines in the spectrum are identified as water absorption lines[43] caused by humidity in ambient air since the interferometer is not protected from it.

To measure the bunch length, shorter scans containing only the central part around the peak are sufficient since only the width of the peak is important in this method. Short 2.2-mm-long interferograms with 5-μm mirror step size are measured for four different Mylar beam-splitter thicknesses and shown in Fig. 2.23. This 5-μm mirror step size corresponding to a 33-fs time resolution is sufficiently accurate for these experiments; however, finer resolution could be achieved by the actuator through smaller step size. Especially, the system has no difficulty to make submicrometer movement, which means that it is capable of having subfemtosecond time resolution. The actual choice of step size or resolution is determined by the expected bunch length. This time resolution is far better than that of the best of time-resolved methods, the streak camera, which is about 0.5 ps so far. The beam parameters are kept the same when different beam splitters are used. As shown in Fig. 2.23, the valleys around the main peak are separated farther apart as the beam-splitter thickness increases. This widens the main peak [cf., Fig. 2.23(a)–(c)] until the valleys are out of the peak [cf., Fig. 2.23(c) and (d)]. In Fig. 2.23(d), even the base of the peak can be seen. Specifically, we note that for a beam splitter thickness $t \gtrsim 50\,\mu$m the width of the main peak does not change anymore and therefore represents a true measure of the bunch length. In the figure, the FWHM's of the main peaks are measured in terms of mirror movement, while corresponding widths in terms of optical path difference are twice of them. These measured interferogram FWHM's and the
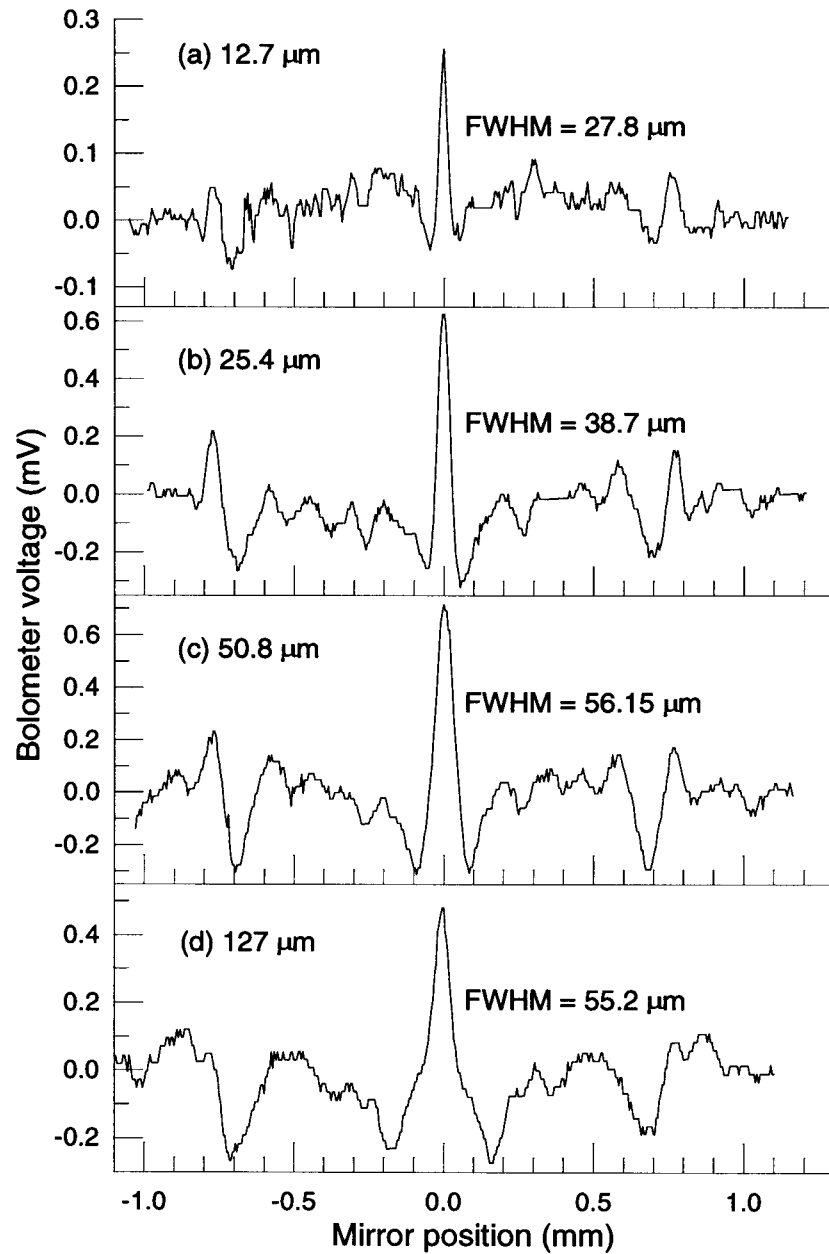
Figure 2.23: Interferograms measured for different Mylar beam-splitter thicknesses: (a) 12.7, (b) 25.4, (c) 50.8, and (d) 127 μm. The FWHM's of the main peaks are measured in mirror movement, which are half of widths in optical path difference.

Table 2.2: Measured interferogram FWHM's in optical path difference (OPD) for different beam-splitter thicknesses and the corresponding estimated equivalent bunch lengths deduced from Fig. 2.21 for Gaussian and rectangular distributions.

Beam splitter thickness (μm)	Interferogram FWHM OPD (μm)	Estimated equivalent bunch length (μm)	
		Gaussian	Rectangular
12.7	55.6	60.8	100.6
25.4	77.4	72.8	103.2
50.8	112.3	86.9	111.0
127.0	110.4	83.1	109.1

rectangular distribution are shown in Table 2.2. The estimated bunch lengths provide bounds for the real bunch length. As the beam-splitter thickness increases from 12.7 to $50.8\,\mu$m, the bound narrows down, which indicates the estimation gets better for thicker beam splitter. Additionally, the bounds stay the same for 50.8- and 127-μm beam splitters and agree with the estimation made from Eq. (2.41) for the ideal beam splitter . It is also worth noticing that the estimated bounds are consistent over a 10-fold change in the beam-splitter thickness. In addition, as indicated in Table 2.2 the variation of the estimated equivalent bunch length for the Gaussian bunch distribution is 34%, while the variation in estimated bunch length for the rectangular one is only 9.8%. This further indicates that the real bunch distribution is closer to the rectangular one than the Gaussian one, which is consistent with the conclusion derived from the roll-off rate of the corrected spectrum discussed in the previous paragraph. The estimated equivalent bunch length is about $110\,\mu$m long (0.367 ps), which corresponds to an rms bunch length of $\sigma_z \approx 32\,\mu$m or $\sigma_t \approx 106\,$fs

assuming a rectangular bunch distribution[2].

2.6.3 Alternative Sources

For linear accelerators, using a solid metal foil to generate coherent transition radiation for the interferometer does not seem to cause a problem although it generally destroys the electron-beam quality after the foil. However, such destructive way is not desirable in circular accelerators. Non-destructive methods such as using a bending magnet to generate coherent synchrotron radiation[44] and using a metal foil with a center hole to generate coherent diffraction radiation[45,46] are suitable for this application. Unlike the case for transition radiation, the single-electron spectrum of these radiating processes is not constant in frequency. In order to extract bunch information $f(\nu; \hat{n})$, the measured spectrum has to be corrected for the single-electron spectrum of these radiating methods [i.e., $I_e(\nu)$ in Eq. (1.10)].

2.6.4 Measurement Summary

A new frequency-resolved bunch-length measuring method specialized for subpicosecond electron pulses has been developed at the Stanford SUNSHINE facility. This method measures the autocorrelation of coherent transition radiation emitted at wavelengths longer than or equal to the bunch length via a far-infrared Michelson interferometer. The bunch length can be derived from the interferogram with special consideration of interference effects in the beam splitter. Measurements have verified

---

[2]We define the root-mean-square (rms) bunch length of a normalized one-dimensional bunch distribution $f(x)$ as

$$l_{rms} \equiv \left(\int_{-\infty}^{+\infty} x^2 f(x) dx \right)^{1/2}.$$

For the Gaussian bunch distribution defined in Eq. (1.18), $l_{rms} = \sigma_z$, while for the rectangular one defined in Eq. (1.16), $l_{rms} = 2\sigma_z/\sqrt{12}$.

this method by showing consistent results over a broad range of beam-splitter thicknesses for subpicosecond electron bunches. In a separated study, it has been shown that this method will work also for bunch length on the order of one picosecond[47]. Based on a low-cost, easy-to-operate, compact, and transportable Michelson interferometer, this autocorrelation method demonstrates femtosecond resolving power beyond the reach of existing time-resolved methods.

2.7 Bunch Distributions and Phase-retrieval Methods

·From the theory of Michelson interferometer discussed in Sec. 2.5.1.3, the autocorrelation method will only measure the power spectrum of the incident light pulse. Phase information, however, is lost in the measurement. In order to obtain the bunch distribution, the phase information has to, somehow, be retrieved from the measured amplitude information through numerical methods with some assumed constrains applied to the measured data.

2.7.1 Longitudinal Distribution

In principle, the measured spectral information can be used to reconstruct the bunch distribution and give a better bunch-length measurement. However, there are some practical difficulties in reconstructing the electron distribution for this experiment. First, the spectrum is contaminated by water absorption lines[17,18] because the interferometer is not protected from humidity. These lines are hard to remove, and their effects on the reconstructed distribution are not clear. Secondly, the zeros of the beam-splitter efficiency produce artificial peaks when the spectrum is numerically corrected for the beam-splitter interference effects[17,18]. Unfortunately, in the presence

of measurement noises, these peaks are also not easy to remove. Finally, there are *infinite* distributions which give the same autocorrelation even if the constraints for non-negative and real electron distribution are employed[48]. This one-dimensional phase-retrieval problem is equivalent to that of an under-determined system, and the non-uniqueness is followed from the *existence* of the Fundamental Theorem of Algebra for polynomials of one variable[48,49]. Although one-dimensional phase-retrieval methods have been suggested for this reconstruction problem[44,50,51], they can not guarantee the uniqueness of the solution, not to mention the immunity against noises in data. Structures generated by these reconstruction methods need to be verified as to whether they are real bunch structures or artifacts produced by the methods.

2.7.2 Three-dimensional Distribution

Although one-dimensional phase-retrieval methods do not give unique solutions to the bunch distribution, going to two- and higher-dimensional phase-retrieval methods can give *almost* unique solutions to this problem. This is equivalent to the problem of an over-determined system, and the uniqueness is followed from the *nonexistence* of the Fundamental Theorem of Algebra for polynomials of two or more variables[48,49]. This surprising result shed light on the possibility of extending this bunch-length measuring method to a three-dimensional bunch distribution measurement.

By recalling that the bunch form factor $f(\nu; \hat{n})$ is indeed a two-variable function, measuring the spectrum through the autocorrelation method at different observation angles (θ and ϕ) will give the information of the three-dimensional k-space (k_x, k_y, and k_z with $k = 2\pi/\lambda = \omega/c$) of the bunch distribution when the angular spectral distribution [i.e., $d^2\mathcal{E}/d\omega d\Omega$] of the radiating process has been deconvolved. This is similar to the x-ray computed tomography (CT) scans in the medical applications, which measures x-ray transmission through the body at different angles. By applying a three-dimensional phase-retrieval method, it is more likely to obtain an unique

solution to the three-dimensional bunch distribution. However, more complicated hardware and longer measuring time are necessary for this extension. And definitely, more study has to be devoted to investigate and realize this new idea.

Chapter 3

Stimulated Coherent Transition Radiation

The characterization of coherent transition radiation described in the previous chapter shows that the spectrum of the radiation emitted from subpicosecond electron bunches covers a broad range in the far-infrared regime from millimeter waves to about 100-μm radiation (cf., Fig. 2.22). Furthermore, the energy characterization discussed in Sec. 2.3.2.2 also shows promise for the use of coherent transition radiation as a new way to produce high-power far-infrared light. In the measurement, each electron bunch radiates a total energy of about 0.544 μJ, and about 0.171 μJ energy is collected by the bolometer. The bunch length is estimated about 0.483 ps. If one calculates the simple-minded "peak" power by the ratio of the total radiation energy to bunch duration, this would give a peak power of about 1.13 MW for the total emitted radiation and 354 kW for the collected part of radiation! To get a more precise estimate from the spectral peak power, one can compare the energy radiated from a bunch to that described in Fig. 1.4. Such comparison would give an estimated spectral peak power on the order of about a few hundred watts (collected) to a few kilowatts (total) per 0.1% bandwidth in the far-infrared regime. These results are

already far better than blackbody radiators (cf., Fig. 1.4) and are in the middle range among other existing high-power light sources shown in Fig. 1.3.

In order to further increase the power of coherent transition radiation, a few directions can be considered. A direct way to do this is to pack more electrons in one electron bunch since the intensity increases quadratically with the electron number. An alternative direction is to decrease the bunch length, which will increase the spectral range to produce photons with higher energy. However, both methods depend upon the bunch generation and compression system, which may or may not provide an extra degree of freedom for such improvements. Any dramatic improvement in these directions requires new ideas and a major design change in the system. Instead of increasing the power through spontaneous emission of coherent transition radiation, a possible direction is to use stimulated emission of coherent transition radiation to boost the radiation power. In this way, it does not require changes in the bunch generation and compression system; however, a special device is needed to make stimulation possible.

Similar to the principle of lasers, the emission of coherent transition radiation from subpicosecond electron bunches is stimulated when an "external" electromagnetic stimulation is appropriately arranged through a special device. The extra amount of radiation energy through stimulation is proportional to this external stimulation. Hence, the total radiation energy through stimulated emission can be much larger than that through spontaneous emission. Unlike lasers, such stimulated emission of coherent transition radiation from electron bunches is not in favor of any color, nor does it require population inversion since the energy states of free electrons are continuous. Therefore, stimulated coherent transition radiation is a good direction to produce high-power, broadband, coherent, far-infrared radiation.

In this chapter, we will study the possibility of using stimulated coherent transition radiation as a new high-intensity far-infrared light source. Through the invention of a

special cavity named BRAICER, a new way of using a train of subpicosecond electron bunches generated at SUNSHINE to produce self-stimulated, broadband, coherent radiation is explored. In the cavity, far-infrared light pulses of coherent transition radiation emitted from subpicosecond electron bunches are delayed and circulated to coincide with subsequent incoming electron bunches. This coincidence of light pulses with electron bunches enables the light to do work on the electrons, thus, stimulates more radiated energy. The stimulation of radiation is observed through detuning measurements of the cavity and agrees with theoretical predictions[52]. Following this observation, different cavity designs to produce high-intensity radiation in multi-pulsed and fast Q-switched modes will be discussed.

3.1 Stimulation of Transition Radiation

Stimulated transition radiation is emitted when electrons pass through the interface between two media of different dielectric constants in the presence of an external electromagnetic field in phase with the spontaneous transition radiation. The special phase relation enables the external field to do work on the electrons so that additional energy is extracted from the electrons to the radiation field. This phenomena was predicted in theory several years ago[53,54].

Since Maxwell's equations are linear, the field solution to stimulated transition radiation in the inhomogeneous wave equations can be split into two linearly independent parts[54]: the general solution of homogeneous equations for the external field and the special solution of inhomogeneous equations including the electron beam. The former part is equivalent to Fresnel's equations for reflection and refraction of the external field, while the latter part is just ordinary spontaneous transition radiation emitted from electrons. Let us assume the electric field solution to the first part is $\mathbf{E}_{ext}$, and that to the second part is $\mathbf{E}_{sp}$. Then the total field for stimulated transition

radiation is the sum of these two fields: $\mathbf{E}_{ext} + \mathbf{E}_{sp}$. Hence, the total radiated intensity is proportional to $|\mathbf{E}_{ext} + \mathbf{E}_{sp}|^2$. The extra output energy

$$
\begin{aligned}
\Delta \mathcal{E} \quad &\propto \quad |\mathbf{E}_{ext} + \mathbf{E}_{sp}|^2 - |\mathbf{E}_{ext}|^2 - |\mathbf{E}_{sp}|^2 \\
&= \quad 2\,\mathrm{Re}(\mathbf{E}_{ext} \cdot \mathbf{E}_{sp}^*)
\end{aligned}
\tag{3.1}
$$

is the stimulated radiation which is due to the work done by the external field on electrons[54]. This extra stimulated energy is proportional to the applied external field. When the external field $\mathbf{E}_{ext}$ is in phase with the spontaneous field $\mathbf{E}_{sp}$ (i.e., $\mathbf{E}_{ext} \cdot \mathbf{E}_{sp}^* > 0$), the energy is extracted from electrons into the radiation field, and the extra stimulated energy is maximized. This process is called *stimulated emission*. On the other hand, when the external field is out of phase with the spontaneous field (i.e., $\mathbf{E}_{ext} \cdot \mathbf{E}_{sp}^* < 0$), the energy is transferred from the external field into electrons, and the electrons are accelerated by the external field. This is called *stimulated absorption*. Stimulated absorption may be useful for the acceleration of electrons and is out of the scope of this thesis.

3.1.1 External versus Self Stimulation

In order to make stimulation happen, it is necessary to supply the "external" stimulation field in some way. One direct way is to use an external high-intensity light source such as a laser to achieve high stimulation electric field. The electrons will then emit radiation through stimulation. The stimulated radiation will have the same bandwidth as the external light source. This can be viewed as an amplifier for the external source. However, such way of stimulation requires designs to incorporate other high-intensity light sources and complicates the design of the experimental apparatus.

Another direction to supply an "external" stimulation field is to use a special structure to delay the previously generated spontaneous radiation and to coincide this radiation with electrons at the following stage of the radiating process. Such a
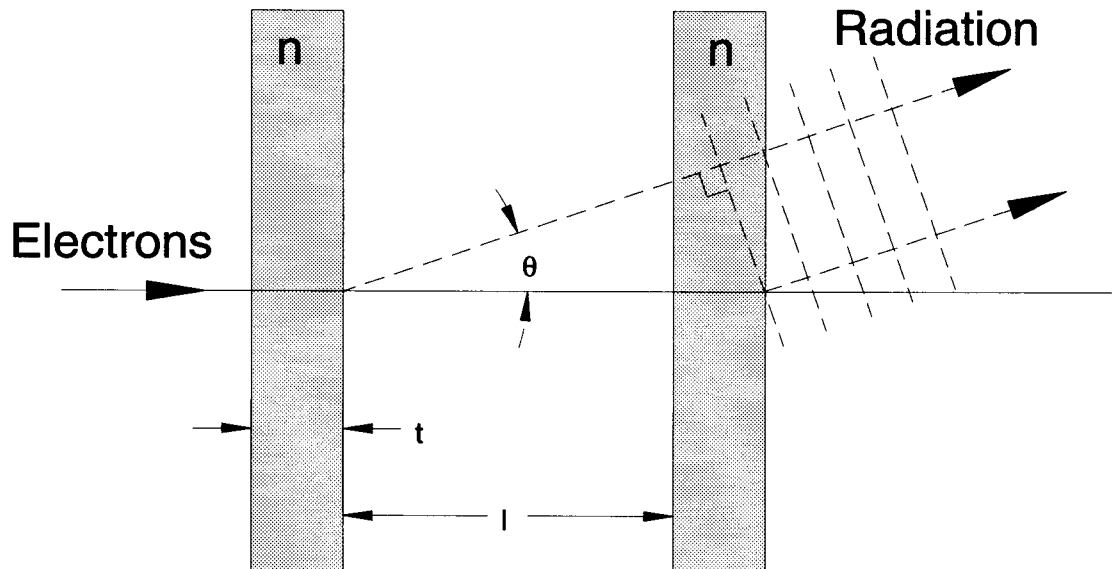
Figure 3.1: A single-bunch auto-stimulation design through a multi-foil structure.

structure for self-supplied stimulation field can be realized in a simpler design and is quite suitable for the production of broadband radiation. In the following sections, two different structures for single-bunch and multi-bunch cases will be discussed.

3.1.2 Single-bunch Auto-stimulation

When there is only one electron bunch produced in the time period of interest (e.g., a low repetition rate in the bunch generation system), one can consider a multi-foil structure shown in Fig. 3.1 to generate the self-supplied stimulation field. Although the speed of light c is always faster than the speed of electrons v in vacuum (i.e., $\beta = v/c < 1$), this situation is totally reversed in a dielectric material with a refractive index n greater than one. The speed of relativistic electrons in this material is not so different from that in vacuum. However, the speed of light in this material is slower than that in vacuum by a factor of n (i.e., $c_{\text{material}} = c/n$). This usually makes the electrons traveling much faster than light, i.e., $\beta > c/n$ (e.g., consider $n = 1.85$ for

Mylar in the far-infrared regime). Hence, by selecting the appropriate foil thickness t and foil spacing l, the radiation emitted from the previous foil can be delayed to coincide with the electrons at the corresponding interface of the next foil. Such coincidence could provide a way to stimulate the emission of transition radiation.

To derive the resonance condition, let us consider the geometry shown in Fig. 3.1. The electrons are traveling in the direction normal to the foil surfaces. The phase difference between the radiation emitted from the material-to-vacuum interface of the first foil and that from the corresponding interface of the second foil is

$$
\begin{aligned}
\psi &= \omega \left(\frac{l \cos \theta}{c} + \frac{t \cos \theta}{c/n} - \frac{l+t}{\beta c} \right) \\
&= \frac{\omega c}{\beta} [t(n\beta \cos \theta - 1) - l(1 - \beta \cos \theta)],
\end{aligned} \tag{3.2}
$$

where ω is the angular frequency of the light, and θ is the angle between the radiation direction and the electron motion. The condition of resonance is obtained by setting this phase difference to zero, i.e., the electrons catch up the light at corresponding interface of the second foil. This condition can be expressed as

$$
\frac{t}{l} = \frac{1 - \beta \cos \theta}{n\beta \cos \theta - 1}. \tag{3.3}
$$

This resonance condition is also that for the radiation emitted from the vacuum-to-material interfaces of all foils. Besides, there is a strong destructive interference between the radiation from both sets of interfaces. This interference effect will reduce the total intensity. Furthermore, the multiple reflection and transmission of the foils will also reduce the strength of the stimulation field and, hence, the total intensity. These are the undesirable features of this structure. However, if the losses are negligible, the field of light pulses will increase linearly with the number of foils that the electrons have passed through. Hence, the intensity of light pulses will increase quadratically with the number of foils passed.
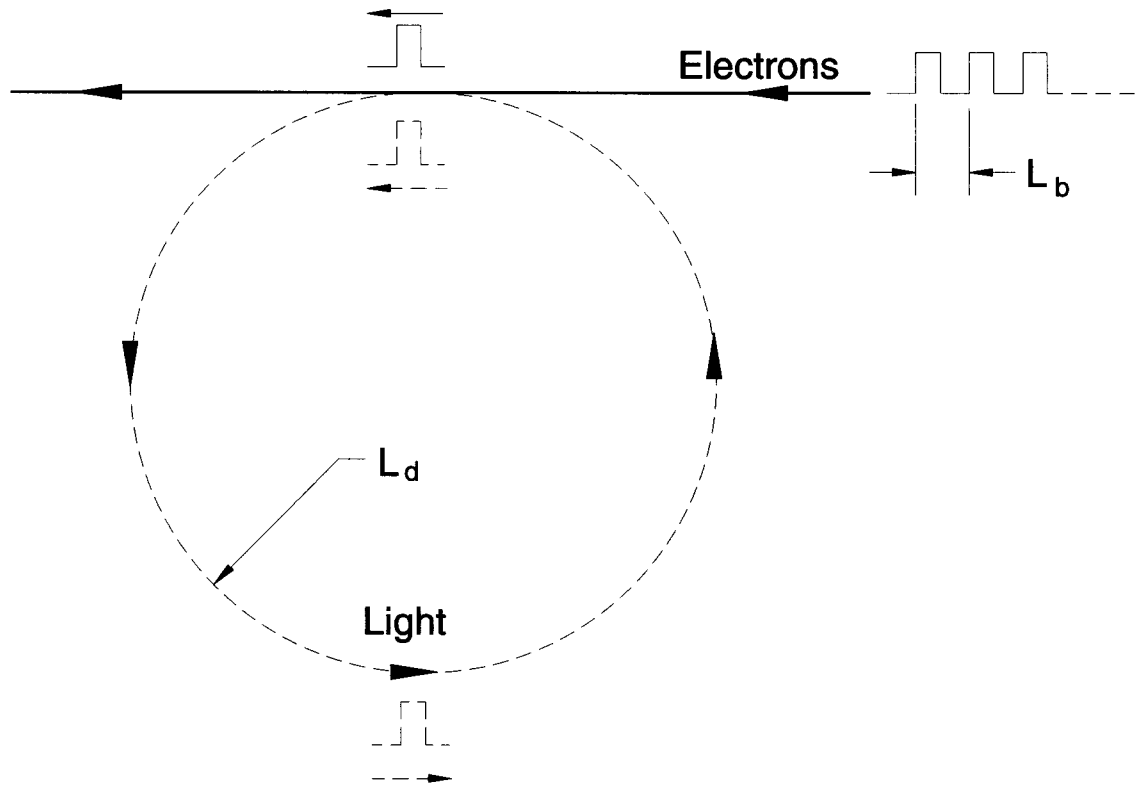
Figure 3.2: A multi-bunch cross-stimulation structure using a time-delayed loop.

3.1.3 Multi-bunch Cross-stimulation

When there is a train of equally spaced electron bunches produced within the time period of interest, one can consider the structure as shown in Fig. 3.2 as a way to produce the self-supplied stimulation fields. This multi-bunch cross-stimulation structure uses a time-delayed loop to delay and circulate the radiation emitted from previous electron bunches. By adjusting the amount of delay, light pulses can coincide with subsequent electron bunches and, thus, provide a way to stimulate the emission of radiation. The resonance condition for this structure using the geometry shown in Fig. 3.2 can be expressed as

$$L_\mathrm{d} = \frac{m}{n} L_\mathrm{b}, \tag{3.4}$$

where L_d is the length of the time-delayed loop, and L_b is the distance between two adjacent electron bunches. The parameters m and n are mutually primed integers with m smaller than the total number of electron bunches in the bunch train. This condition means that as the light pulses have traveled n turns in the loop, they will coincide with the subsequent m^{th} incoming electron bunch.

If the intensity loss during circulation is negligible, the field of light pulses will increase linearly with the number of electron bunches that they have encountered. Hence, the intensity of light pulses will increase quadratically with the number of encountered electron bunches. Since there are about 3000 electron bunches in each 1-μs-long macro-pulse produced at SUNSHINE, the total intensity of stimulated radiation using this structure can be much greater than that emitted from the same number of bunches through spontaneous emission if the circulation loss is minimized. In the following sections, different designs using this time-delayed structure will be studied both theoretically and experimentally to explore the possibility of using them for the production of high-intensity far-infrared radiation.

3.2   The BRAICER Cavity

As discussed in the previous section, the multi-bunch cross-stimulation design using a time-delayed structure shows a promising direction in the production of high-intensity radiation. Especially, it fully utilizes the feature of long trains of electron bunches at SUNSHINE. Unlike the multi-foil single-bunch auto-stimulation design, it does not have any intrinsic loss problem, and the circulation loss can be minimized through better component designs. In this section, a specially designed cavity using this time-delayed principle to produce broadband stimulated coherent transition radiation will be studied.
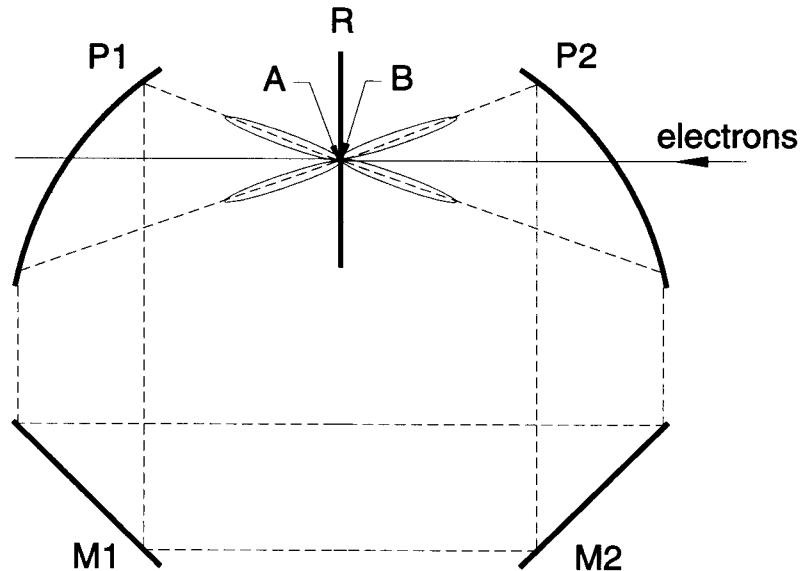
Figure 3.3: Conceptual schematic diagram of the BRAICER cavity.

3.2.1   A Conceptual Design

To observe stimulated transition radiation, we have designed a special cavity named BRAICER (Broadband Radiation Amplifier via Inducing and Circulating Emission of Radiation). The conceptual schematic diagram of the BRAICER cavity is shown in Fig. 3.3. It consists of a metallic foil radiator/reflector (R), two off-axis parabolic reflectors (P1 and P2), and two plane reflectors (M1 and M2). The focal points of P1 and P2 are aligned with points A and B, respectively. When divergent transition radiation is emitted from A, it will become parallel after P1. This parallel light is then transported through M1 and M2 to P2, which will focus this parallel light onto a point at B. In the same way, transition radiation emitted from point B will also be transported and focused at point A.

To see how this cavity works, let us assume the loop length (e.g., A → P1 → M1 → M2 → P2 → B) is equal to the distance between two adjacent electron bunches of a train of N identical equidistant electron bunches. No loss in the cavity is assumed. When the first bunch passes through A and B, it radiates forward (to the left-hand

side) and backward (to the right-hand side) transition radiation. We will first focus on the forward radiation (emitted at **A**). By assuming the emitted field is **E**, the radiated energy is proportional to $|\mathbf{E}|^2$ in the forward radiation. This radiation travels from **A** counterclockwise (CCW) to **B**. As it reaches **B**, the next incoming electron bunch also arrives at **B**. Hence, the total radiated field is **E** (traveling radiation from the first bunch reflected by **R**) + **E** (spontaneous backward radiation emitted from the second bunch). The radiated energy is now proportional to $|\mathbf{E} + \mathbf{E}|^2 = 4|\mathbf{E}|^2$, and the extra stimulated energy is proportional to $2|\mathbf{E}|^2$. The combined radiation then travels from **B** clockwise (CW) to **A**. As it reaches **A**, the third electron bunch also crosses **A**. This time, the total radiated field is 2**E** (traveling radiation from the first and second bunch reflected by **R**) + **E** (spontaneous forward radiation emitted from the third bunch). The radiated energy is then proportional to $|2\mathbf{E} + \mathbf{E}|^2 = 9|\mathbf{E}|^2$, and the extra stimulated energy is proportional to $4|\mathbf{E}|^2$. This process goes on until all N bunches have passed through the cavity. The radiated energy after N bunches is then proportional to $N^2|\mathbf{E}|^2$. Comparing this to the total energy radiated from the same N electron bunches through spontaneous emission, which is only proportional to $N|\mathbf{E}|^2$, this resonant cavity radiates N times more energy. The same process also applies to the backward radiation emitted from the first bunch. Therefore, there are two independent radiation pulses traveling in opposite directions around the cavity.

3.2.2 The Polarization Issue

The "in-phase" condition for the stimulation field (i.e., $\mathbf{E}_{ext} \cdot \mathbf{E}_{sp}^* > 0$) requires not only the phase of the stimulation field $\mathbf{E}_{ext}$ to be the same as that of the spontaneous field $\mathbf{E}_{sp}$ through appropriate timing method (e.g., the time-delay of the stimulation field) but also the polarization of the stimulation field to have the same direction and distribution as that of the spontaneous field through appropriate optical arrangement. Some ways to adjust the phase of the stimulation field to synchronize with that
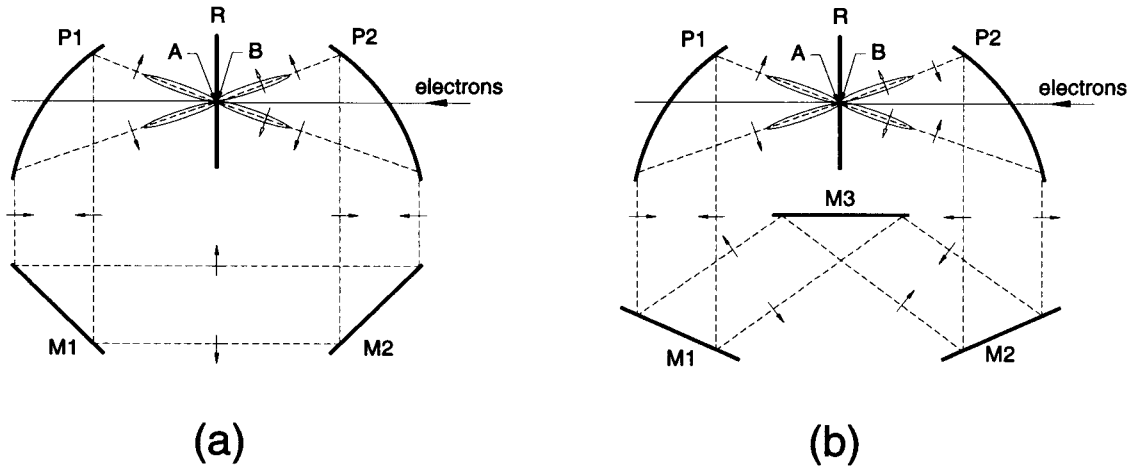
(a) **(b)**

Figure 3.4: The polarization alignments in the BRAICER cavity. Two designs to demonstrate (a) in-phase and (b) out-of-phase polarization alignments are shown. The solid arrows trace the polarization of forward transition radiation emitted from the radiator R which starts from the left-hand side of R and travels counterclockwise in the cavity to the right-hand side of R as the stimulation field. The hollow-headed arrows (near B) show the polarization of backward transition radiation emitted on the right-hand side of R.

of the spontaneous field through different timing methods have been discussed in Sec. 3.1.1. In this section, we will discuss the importance of the polarization issue in the stimulation of transition radiation when designing the optics for the BRAICER cavity.

As shown in Fig. 3.4, two different cavity designs demonstrate different polarization alignments. Since the cavity only consists of metallic reflectors, the only change of polarization vectors is the reversing of vectors after each reflection. By tracing the change of polarization vectors through out the cavity, the in-phase condition can be verified. In Fig. 3.4(a), the polarization of transition radiation emitted from one side of the radiator R after one-loop-length-long travel will have the same direction as that of the radiation emitted from the other side of R. This optical arrangement along with the resonance condition in Eq. (3.4) will meet the in-phase condition for stimulated

emission. On the other hand, the design shown in Fig. 3.4(b) makes the polarization of transition radiation emitted from one side of R after one-loop-length-long travel in the opposite direction to that of the radiation emitted from the other side of R. This violates the in-phase condition. However, with the resonance condition in Eq. (3.4), this design will meet the "out-of-phase" condition for stimulated absorption (i.e., $\mathbf{E}_{ext} \cdot \mathbf{E}_{sp}^* < 0$) for the acceleration of electrons. Hence, it is important to trace the polarization of radiation in the cavity in order to make sure that the optical design will meet the requirement for stimulation.

3.2.3   Resonances of the Cavity

According to the discussion in the above section, the BRAICER design shown in Fig. 3.3 will meet the polarization requirement for stimulated emission. Combined with the condition for the cavity loop length discussed in Sec. 3.2.1, transition radiation from bunches will resonate in the cavity and stimulate emission of transition radiation. In addition to the resonance at the loop length d_{lp} equal to the inter-bunch distance d_{ib}, the BRAICER cavity will also resonate at other loop lengths. When the loop lengths are integral multiples of the inter-bunch distance (say $d_{lp} = m\, d_{ib}$), the radiation emitted by an electron bunch will travel around the cavity once and meet the next m^{th} incoming bunch. All these resonances described so far are called *first-order resonances*. Similarly, if the loop lengths are half-integral multiples of d_{ib} (say $d_{lp} = \frac{m}{2} d_{ib}, m$ odd), the radiation emitted by a bunch must travel around the cavity twice (e.g., A $\xrightarrow{CCW}$ B $\xrightarrow{CW}$ A) to meet the next m^{th} incoming bunch. These are categorized as *second-order resonances*. Thus, the order of resonance is defined by the number of loop travel around the cavity necessary for the light pulse to meet a subsequent electron bunch. In general, it takes a pair of mutually primed integers (m, n) to specify a resonance, where m is called the *index* of the resonance, and n, the *order* of the resonance. The mth resonance of the nth order has the resonance
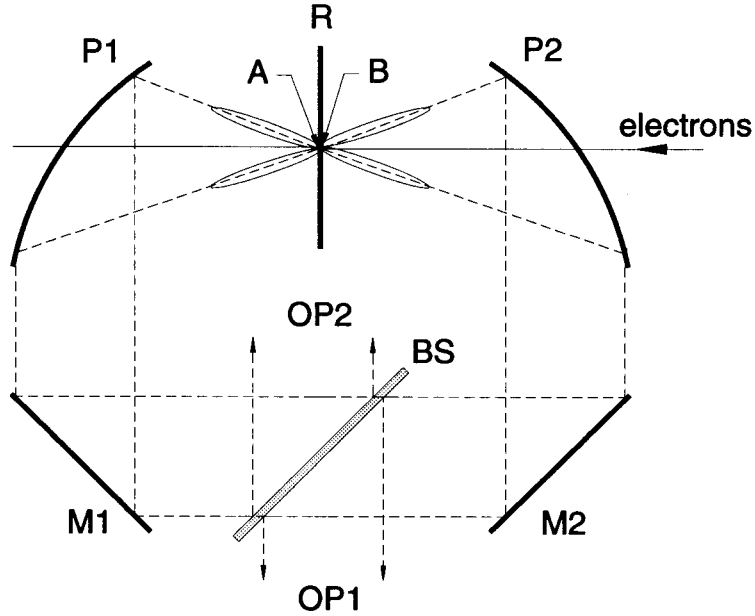
Figure 3.5: A BRAICER cavity with a beam splitter to monitor the progress of stimulation.

condition of

$$d_{lp} = \frac{m}{n} d_{ib},$$ (3.5)

which means that the light pulse emitted from some electron bunch has to travel n times around the cavity in order to meet the next m^{th} subsequent bunch. If there are no cavity losses, these resonances will reach an amplitude proportional to about $m(N/m)^2|E|^2 = N^2|E|^2/m$, which is independent of the order of the resonance n. The dependence on m, the index of the resonance, comes from the fact that there are m almost identical light pulses separated by a distance of d_{ib} traveling in the cavity as a group each encountering about N/m electron bunches. However, in the presence of cavity losses, the final amplitudes greatly depend on these losses, and higher order resonances will reach lower amplitudes due to longer travel in the cavity.

3.2.4 The Theoretical Perspective

In order to verify the stimulation of radiation, it is necessary to have a special mechanism to probe the radiation in the cavity. The easiest way is to insert a beam splitter (BS) in the path of radiation to couple a portion of the circulated energy out of the cavity as shown in Fig. 3.5. When the light pulses are circulating clockwise in the cavity, part of their energy will be coupled out to the port OP1. On the other hand, as the light pulses are traveling counterclockwise in the cavity, a fraction of the light will be coupled out to the port OP2. Both ports are similar to but independent of each other. Hence, only the case for one port needs to be considered.

Let us first assume that the amplitude reflection (R) and transmission (T) coefficients of the beam splitter are constant of frequency and satisfy $|R|^2 + |T|^2 = 1$. For analytic simplicity, the beam splitter is assumed to be located in the middle of the loop. The cavity loss is also assumed to be uniform in the cavity with α, the field attenuation per unit length. Hence, the remaining percentage for the light after travelling a distance of l is defined as α^l. Because of the linearity of Maxwell's equation discussed in Sec. 3.1, we can consider the contribution from each light pulse and use superposition principle for electric fields to calculated the total field and intensity from these light pulses. When a light pulse is emitted at R from some electron bunch, it travels back and forth around the cavity, loses energy along the way because of cavity losses, and couples out some energy into the ports every time when it passes through the beam splitter. When tracing a light pulse emitted on the right-hand side of R (backward transition radiation) from the kth electron bunch in a train of N electron bunches with inter-bunch distance of d_{ib}, the electric field coupled out to OP1 from this pulse can be expressed in the time domain as

$$E_k^{\text{RHS}}(t) = R\alpha^{d_{lp}/2}E(t - t_0 - k\frac{d_{ib}}{c}) + R\alpha^{5d_{lp}/2}T^2E(t - t_0 - k\frac{d_{ib}}{c} - 2\frac{d_{lp}}{c})$$
$$+ R\alpha^{9d_{lp}/2}T^4E(t - t_0 - k\frac{d_{ib}}{c} - 4\frac{d_{lp}}{c}) + \cdots$$

$$= Ra^{d_{lp}/2} \sum_{j=0}^{\infty} \left(\alpha^{d_{lp}}T\right)^{2j} E(t - t_0 - k\frac{d_{ib}}{c} - 2j\frac{d_{lp}}{c}), \qquad (3.6)$$

where E is the field of coherent transition radiation emitted from one electron bunch, the time t is referenced to the beginning of the bunch train, $t_0 = d_{lp}/2c$ is the time for the pulse to travel from R to BS, d_{lp} is the loop length, c is the speed of light, and k is an integer ranging from 0 to $N-1$. Similarly, when tracing a light pulse emitted on the left-hand side of R (forward transition radiation) from the kth electron bunch, the electric field coupled out to OP1 from this pulse is expressed as

$$\begin{aligned}
E_k^{LHS}(t) &= Ra^{3d_{lp}/2}T E(t - t_0 - k\frac{d_{ib}}{c} - \frac{d_{lp}}{c}) + Ra^{7d_{lp}/2}T^3 E(t - t_0 - k\frac{d_{ib}}{c} - 3\frac{d_{lp}}{c}) \\
&\quad + Ra^{11d_{lp}/2}T^5 E(t - t_0 - k\frac{d_{ib}}{c} - 5\frac{d_{lp}}{c}) + \cdots \\
&= Ra^{d_{lp}/2} \sum_{j=0}^{\infty} \left(\alpha^{d_{lp}}T\right)^{2j+1} E[t - t_0 - k\frac{d_{ib}}{c} - (2j+1)\frac{d_{lp}}{c}].
\end{aligned} \qquad (3.7)$$

These two series of light pulses (E_k^{RHS} and E_k^{LHS}) will cross stimulate each other while traveling in the cavity and meeting subsequent electron bunches. For example, if $d_{lp} = d_{ib}$, E_k^{RHS} after traveling one loop length in the cavity will stimulate radiation emitted on the left-hand side of R by the following bunch and, furthermore, after an additional loop-length-long travel stimulate radiation emitted on the right-hand side of R by the third subsequent bunch, and so forth. Hence, the total electric field coupled out to OP1 from all the bunches is the sum of Eqs. (3.6) and (3.7) over all k's, i.e.,

$$\begin{aligned}
E_{total}(t) &= \sum_{k=0}^{N-1} \left[E_k^{RHS}(t) + E_k^{LHS}(t) \right] \\
&= Ra^{d_{lp}/2} \sum_{k=0}^{N-1} \sum_{j=0}^{\infty} \left(\alpha^{d_{lp}}T\right)^{j} E(t - t_0 - k\frac{d_{ib}}{c} - j\frac{d_{lp}}{c}).
\end{aligned} \qquad (3.8)$$

Transforming this expression into the frequency domain using Eq. (2.34) yields a simple one for the electric field

$$\tilde{E}_{total}(\omega) = Ra^{d_{lp}/2} \sum_{k=0}^{N-1} \sum_{j=0}^{\infty} \left(\alpha^{d_{lp}}T\right)^{j} \tilde{E}(\omega) e^{i\omega[k(d_{ib}/c)+j(d_{lp}/c)]}$$
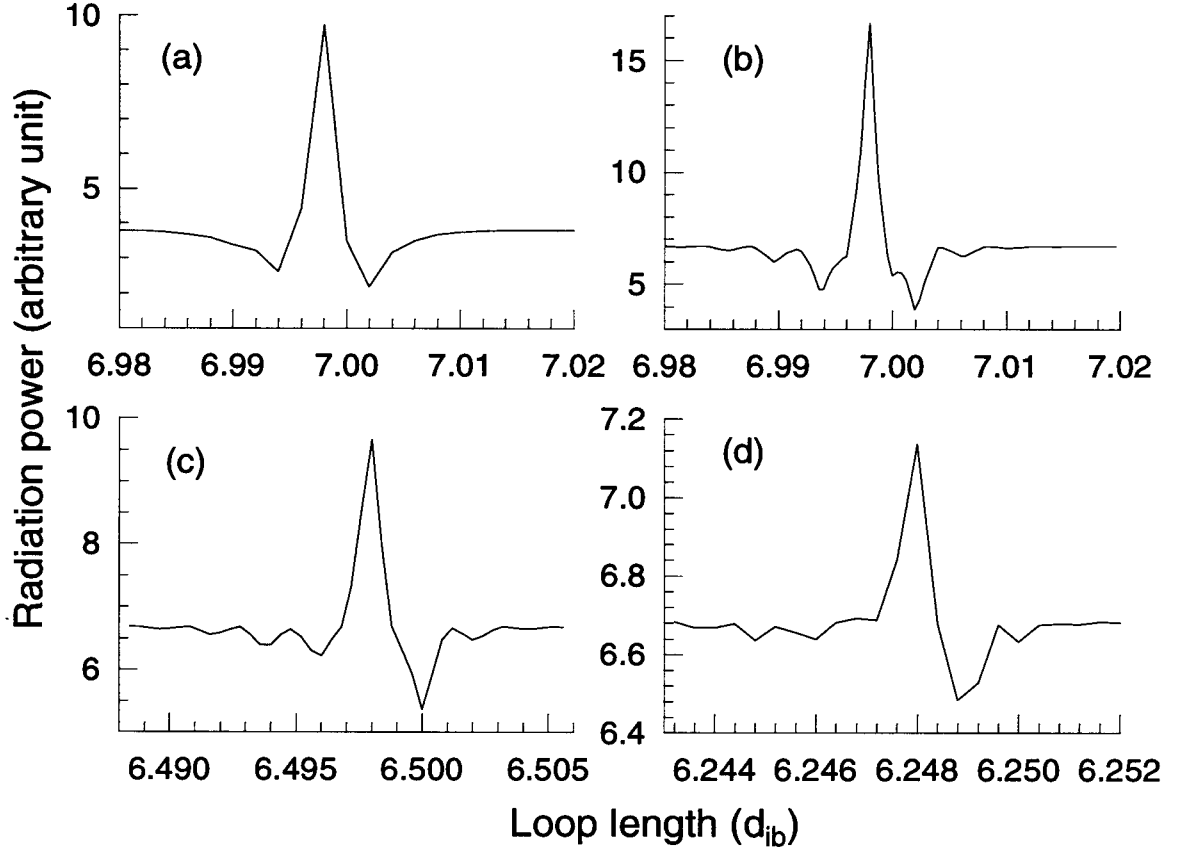
Figure 3.6: Some typical resonances of the BRAICER cavity for Gaussian and rectangular bunch distribution. Resonances shown here are for (a) Gaussian bunches at a first-order $(7d_{ib})$ resonance and for rectangular bunches at a (b) first- $(7d_{ib})$, (c) second- $(6.5d_{ib} = \frac{13}{2}d_{ib})$, and (d) fourth-order $(6.25d_{ib} = \frac{25}{4}d_{ib})$ resonance.

$$
\begin{aligned}
&= R\alpha^{d_{lp}/2}\tilde{E}(\omega)\sum_{k=0}^{N-1} e^{i\omega k(d_{ib}/c)}\sum_{j=0}^{\infty}\left(\alpha^{d_{lp}}T\right)^{j}e^{i\omega j(d_{lp}/c)}\\
&= R\alpha^{d_{lp}/2}\tilde{E}(\omega)\frac{1-e^{i\omega N d_{ib}/c}}{1-e^{i\omega d_{ib}/c}}\frac{1}{1-\alpha^{d_{lp}}Te^{i\omega d_{lp}/c}},
\end{aligned}
\tag{3.9}
$$

where $\tilde{E}(\omega)$ is the field of coherent transition radiation emitted from one electron bunch at angular frequency ω. The common phase factor $e^{i\omega d_{lp}/2c}$ resulting from the time shift t_0 has been ignored here since it does not offer any important physics.

Using Parseval's formula derived from Eq. (2.34):

$$\int_{-\infty}^{+\infty} |E(t)|^2 \mathrm{d}t = \int_{-\infty}^{+\infty} |\tilde{E}(\omega)|^2 \mathrm{d}\omega, \tag{3.10}$$

the total energy coupled out of the cavity is

$$\begin{aligned}
\mathcal{E}_{\text{total}} &\propto \int_{-\infty}^{+\infty} \mathrm{d}\omega \, |R|^2 \alpha^{d_{\text{lp}}} |\tilde{E}(\omega)|^2 \left| \frac{1 - e^{i\omega N d_{\text{ib}}/c}}{1 - e^{i\omega d_{\text{ib}}/c}} \right|^2 \left| \frac{1}{1 - \alpha^{d_{\text{lp}}} T e^{i\omega d_{\text{lp}}/c}} \right|^2 \\
&= \int_{-\infty}^{+\infty} \mathrm{d}\omega \, |R|^2 \alpha^{d_{\text{lp}}} |\tilde{E}(\omega)|^2 \frac{\sin^2(\omega N d_{\text{ib}}/2c)}{\sin^2(\omega d_{\text{ib}}/2c)} \left| \frac{1}{1 - \alpha^{d_{\text{lp}}} T e^{i\omega d_{\text{lp}}/c}} \right|^2 .
\end{aligned} \tag{3.11}$$

Expressions in the frequency domain such as Eqs. (3.9) and (3.11) can be directly applied for beam splitters with varying R and T in the frequency domain.

The power spectrum $|\tilde{E}(\omega)|^2$ in Eq. (3.11) can be obtained from the bunch distribution using Eq. (1.10) and the relation $I_{\text{total}}(\nu) \propto |\tilde{E}(2\pi\nu)|^2$. In Eq. (3.11), the factor $\sin^2(\omega N d_{\text{ib}}/2c)/\sin^2(\omega d_{\text{ib}}/2c)$ results from the Fourier transform of a train of N pulses separated at a distance of d_{ib}. This factor has a spectrum of sharp peaks of height N^2 distributed at integral multiples of $\omega_0 = 2\pi c/d_{\text{ib}}$ with equivalent width of ω_0/N. The cavity resonates when maxima of the factor $|1 - \alpha^{d_{\text{lp}}} T e^{i\omega d_{\text{lp}}/c}|^{-2}$ overlap with maxima of the factor $\sin^2(\omega N d_{\text{ib}}/2c)/\sin^2(\omega d_{\text{ib}}/2c)$ in Eq. (3.11), or equivalently, maxima of the former factor are integral multiples of ω_0, i.e.,

$$m\frac{2\pi c}{d_{\text{lp}}} = n\frac{2\pi c}{d_{\text{ib}}}, \tag{3.12}$$

where m and n are two mutually primed integers. This yields the same resonance condition of the cavity as that in Eq. (3.5) discussed in Sec. 3.2.3.

The behavior of the cavity near different resonant points can be studied using Eq. (3.11) and power spectra of known bunch distributions. Some calculated detuning results [i.e., $\mathcal{E}_{\text{total}}$ as a function of d_{lp} in Eq. (3.11)] for both Gaussian and rectangular bunch distribution are shown in Fig. 3.6. In the calculation, it has been assumed that there are 3000 bunches containing 2×10^8 electrons in each bunch. The bunch distributions are defined by Eq. (1.18) for Gaussian bunches and by Eq. (1.16)

for rectangular ones with a bunch length of $2\sigma_z = 200\,\mu$m. The beam splitter is assumed to be a 127-μm-thick Mylar foil, for which R and T are defined by Eqs. (2.48) and (2.50), respectively. A cavity attenuation of $\alpha^{d_{1p}} = 0.3$ is also assumed. At the first order resonance, the detuning curve for the rectangular bunch distribution [cf., Fig. 3.6(b)] has more structures than that for the Gaussian one [cf., Fig. 3.6(a)] because the former has more high frequency components in its power spectrum. In addition, the valley-like structures around the resonance peaks result from the beam splitter interference effect similar to that discussed in Sec. 2.5.3. At the second order resonance shown in Fig. 3.6(c), the detuning curve has basically the same structures as that for the first order resonance shown in Fig. 3.6(b) except that the horizontal structure scale of the former is about half that of the latter because the light has to travel twice as long in the former one. At the fourth order resonance shown in Fig. 3.6(d), its horizontal structure scale is about one fourth of that of the first order [cf., Fig. 3.6(b)] because the light has to travel four times as long. The slight shifts of the resonance peaks from the theoretical predictions are due to the additional optical path introduced by the Mylar beam splitter.

3.2.5 The On-resonance Gain

After studying the general properties of the BRAICER resonance through detuning calculations, let us focus on the on-resonance behavior of the cavity. In order to study the cavity at resonance, it is necessary to derive the energy coupled out of the cavity as a function of time, or equivalently, the number of electron bunches having passed through the cavity. Since the cavity is at resonance, we have the resonance condition for the loop length as expressed in Eq. (3.5).

When the pth bunch has passed through the cavity, the electric field coupled out of the cavity at this moment contributed from all the previous bunches can be derived

from Eq. (3.8) as

$$
\begin{aligned}
E_{p<N}^{\text{res}}(t) &= R\alpha^{d_{1p}/2} \sum_{\substack{k,j\geq 0 \\ k+j(m/n)=p}} \left(\alpha^{d_{1p}}T\right)^{j} E\left(t - t_0 - k\frac{d_{\text{ib}}}{c} - j\frac{d_{1p}}{c}\right) \\
&= R\alpha^{d_{1p}/2} \sum_{\substack{k,j\geq 0 \\ k+j(m/n)=p}} \left(\alpha^{d_{1p}}T\right)^{j} E\left(t - t_0 - p\frac{d_{\text{ib}}}{c}\right),
\end{aligned} \tag{3.13}
$$

where p is an integer ranging from 0 to $N - 1$, and Eq. (3.5) and $k\frac{d_{\text{ib}}}{c} + j\frac{d_{1p}}{c} = p\frac{d_{\text{ib}}}{c}$ have been used to simplify the equation. Solving k and j required in the equation from $k + j(m/n) = p$ for integers $k, j \geq 0$ and $0 \leq p \leq N - 1$, we obtain $j = nl$ and $k = p - ml$ with the integer $l = 0, 1, \ldots, \lfloor p/m \rfloor$, where $\lfloor x \rfloor$ denotes the *floor* function which rounds x to the nearest integer in the $-\infty$ direction. Hence, the equation can be further simplified as

$$
\begin{aligned}
E_{p<N}^{\text{res}}(t) &= R\alpha^{d_{1p}/2} E\left(t - t_0 - p\frac{d_{\text{ib}}}{c}\right) \sum_{l=0}^{\lfloor p/m \rfloor} \left(\alpha^{d_{1p}}T\right)^{nj} \\
&= R\alpha^{d_{1p}/2} E\left(t - t_0 - p\frac{d_{\text{ib}}}{c}\right) \frac{1 - \left(\alpha^{d_{1p}}T\right)^{n(\lfloor p/m \rfloor + 1)}}{1 - (\alpha^{d_{1p}}T)^{n}}.
\end{aligned} \tag{3.14}
$$

The corresponding Fourier transform of the equation is expressed as

$$
\tilde{E}_{p<N}^{\text{res}}(\omega) = R\alpha^{d_{1p}/2} \tilde{E}(\omega) e^{i\omega p d_{\text{ib}}/c} \frac{1 - \left(\alpha^{d_{1p}}T\right)^{n(\lfloor p/m \rfloor + 1)}}{1 - (\alpha^{d_{1p}}T)^{n}}, \tag{3.15}
$$

where the common phase factor $e^{i\omega d_{1p}/2c}$ resulting from the time shift t_0 has been ignored here. This frequency-domain expression can be extended for the beam splitters with varying R and T in the frequency domain. The total energy coupled out of the cavity at this moment, from either Eqs. (3.14) or Eqs. (3.15), is

$$
\mathcal{E}_{p<N}^{\text{res}} \propto \mathcal{E}_{\text{b}}|R|^{2}\alpha^{d_{1p}} \left[\frac{1 - \left(\alpha^{d_{1p}}T\right)^{n(\lfloor p/m \rfloor + 1)}}{1 - (\alpha^{d_{1p}}T)^{n}} \right]^{2}, \tag{3.16}
$$

where constant R and T are assumed for the beam splitter for simplicity, and $\mathcal{E}_{\text{b}} \propto \int_{-\infty}^{+\infty} |E(t)|^{2} dt = \int_{-\infty}^{+\infty} |\tilde{E}(\omega)|^{2} d\omega$ is the total energy radiated from one electron bunch into a light pulse.

After all the electron bunches have passed through the cavity, the energy stored in the cavity is decaying because the energy is still coupled out of the cavity. At the time $t = t_0 + p(d_{ib}/c)$, where the integer $p \geq N$, the electric field coupled out of the cavity has the same expression as Eq. (3.13) except for the requirement on p. Solving k and j from $k + j(m/n) = p$ for integers $j \geq 0$, $0 \leq k < N$, and $p \geq N$, we obtain $j = nl$ and $k = p - ml$ with the integer $l = \lceil (p - N + 1)/m \rceil, \ldots, \lfloor p/m \rfloor$, where $\lceil x \rceil$ denotes the *ceiling* function which rounds x to the nearest integer in the $+\infty$ direction. Substituting these solutions in Eq. (3.13), we have a simplified expression

$$
\begin{aligned}
E^{\text{res}}_{p \geq N}(t) &= R\alpha^{d_{ip}/2} E(t - t_0 - p\frac{d_{ib}}{c}) \sum_{l = \lceil (p-N+1)/m \rceil}^{\lfloor p/m \rfloor} \left(\alpha^{d_{ip}}T\right)^{nj} \\
&= R\alpha^{d_{ip}/2} E(t - t_0 - p\frac{d_{ib}}{c}) \frac{\left(\alpha^{d_{ip}}T\right)^{n\lceil (p-N+1)/m \rceil} - \left(\alpha^{d_{ip}}T\right)^{n(\lfloor p/m \rfloor + 1)}}{1 - \left(\alpha^{d_{ip}}T\right)^n}.
\end{aligned}
$$

(3.17)

Similar expression to Eq. (3.15) for the corresponding Fourier transform of Eq. (3.17) can be obtained. The total energy coupled out of the cavity at this moment, from Eq. (3.17), for constant R and T assumed for the beam splitter is

$$
\mathcal{E}^{\text{res}}_{p \geq N} \propto \mathcal{E}_b |R|^2 \alpha^{d_{ip}} \left[\frac{\left(\alpha^{d_{ip}}T\right)^{n\lceil (p-N+1)/m \rceil} - \left(\alpha^{d_{ip}}T\right)^{n(\lfloor p/m \rfloor + 1)}}{1 - \left(\alpha^{d_{ip}}T\right)^n} \right]^2.
$$

(3.18)

The energy coupled out of the cavity as a function of time (as multiples of d_{ib}/c) at resonance can be studied using Eqs. (3.16) and (3.18). Some typical calculated results are shown in Fig. 3.7 for different cavity attenuations. The output shown is the normalized factor defined as

$$
\begin{aligned}
\text{Normalized Factor} &\equiv \frac{\mathcal{E}^{\text{res}}_p}{\mathcal{E}_b |R|^2 \alpha^{d_{ip}}} \\
&= \begin{cases} \left[\dfrac{1 - \tau^{\lfloor p/m \rfloor + 1}}{1 - \tau} \right]^2 & \text{for } 0 \leq p < N \\[4mm] \left[\dfrac{\tau^{\lceil (p-N+1)/m \rceil} - \tau^{\lfloor p/m \rfloor + 1}}{1 - \tau} \right]^2 & \text{for } p \geq N \end{cases}
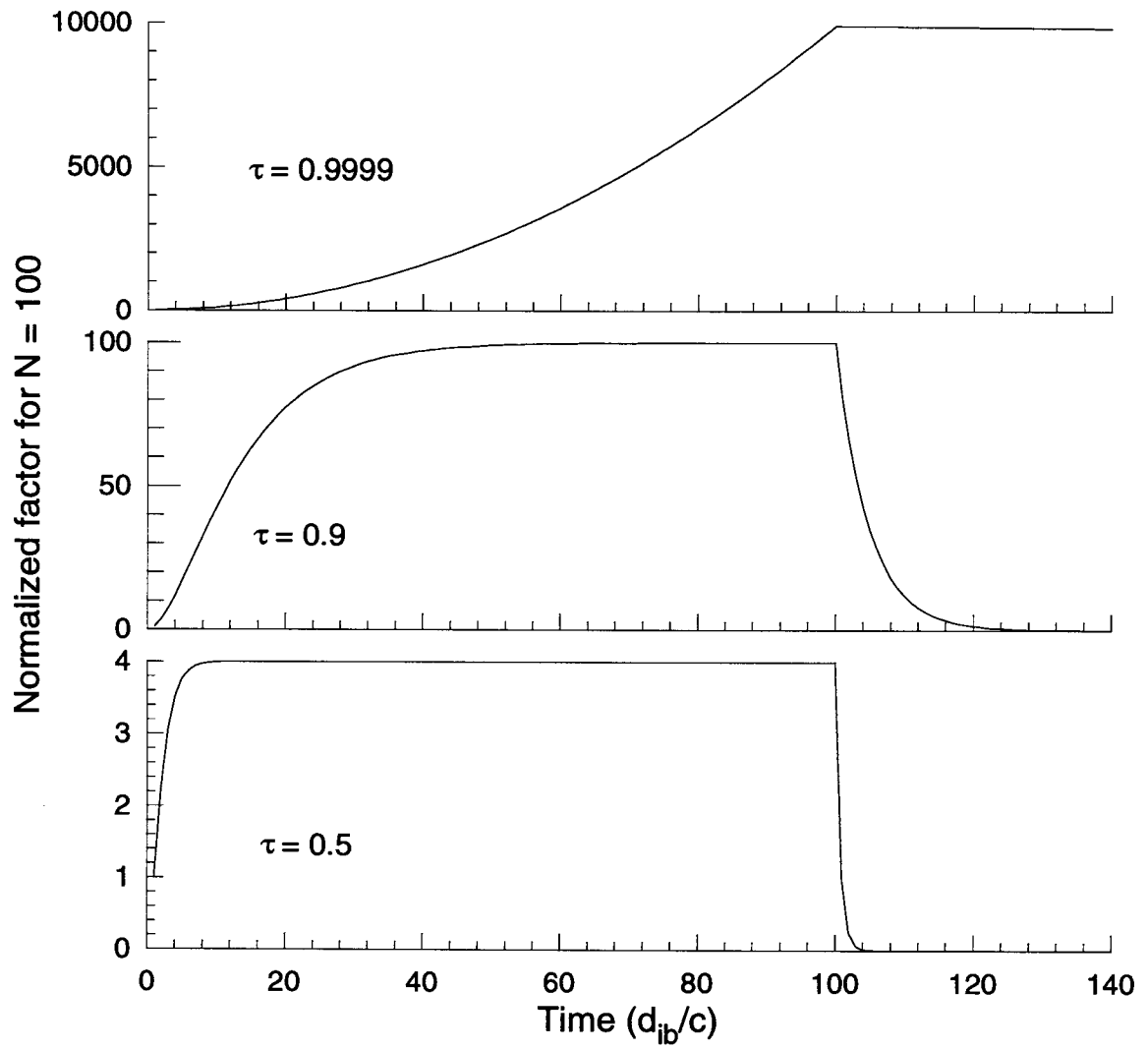\end{aligned}
$$

,(3.19)

Figure 3.7: The on-resonance behavior of the BRAICER cavity for $N = 100$ and $d_{lp} = d_{ib}$ ($m = n = 1$).

where

$$\tau \equiv (\alpha^{d_{1p}} T)^n \qquad (3.20)$$

indicates the total cavity attenuation. For small τ (high loss), the signal has a fast rise to the equilibrium level which is approximately equal to $(1 - \tau)^{-2}$ (cf., Fig. 3.7 for $\tau = 0.5$ and 0.9). After the last electron bunch has passed through the cavity, the signal quickly decays because of the high cavity loss. For τ very close to unity (low loss), the signal rises quadratically with time and reaches the maximum about N^2 and decays slowly after the bunch train has passed the cavity (cf., Fig. 3.7 for $\tau = 0.9999$). It is worth noticing that the energy coupled out is this normalized factor multiplied by $\mathcal{E}_b |R|^2 \alpha^{d_{1p}}$.

The signal gain of the cavity is defined as the maximum energy coupled out divided by $N\mathcal{E}_b$, which is the total radiated energy for spontaneous emission. This is an indicator of how effective the BRAICER cavity is producing stimulated radiation when compared to the spontaneous emission case. Since the maximum energy coupled out always happens when the last bunch is passing through the cavity, the signal gain can be expressed as

$$
\begin{aligned}
\text{Signal Gain} &\equiv \frac{\mathcal{E}_{p=N-1}^{\text{res}}}{N\mathcal{E}_b} \\
&= \frac{|R|^2 \alpha^{d_{1p}}}{N} \left[\frac{1 - \left(\alpha^{d_{1p}} T\right)^{n(\lfloor (N-1)/m \rfloor + 1)}}{1 - (\alpha^{d_{1p}} T)^n} \right]^2 \\
&= \frac{|R|^2 \alpha^{d_{1p}}}{N} \left[\frac{1 - \tau^{\lfloor (N-1)/m \rfloor + 1}}{1 - \tau} \right]^2, \qquad (3.21)
\end{aligned}
$$

where τ is defined in Eq. (3.20). However, for simpler comparison with different attenuation τ, we will define the normalized gain as

$$\text{Normalized Gain} = \frac{1}{N} \left[\frac{1 - \tau^{\lfloor (N-1)/m \rfloor + 1}}{1 - \tau} \right]^2. \qquad (3.22)$$

The calculated normalized gain as a function of attenuation τ is shown in Fig. 3.8. This gain increases slowly for small τ and quickly when τ approaches unity. For small
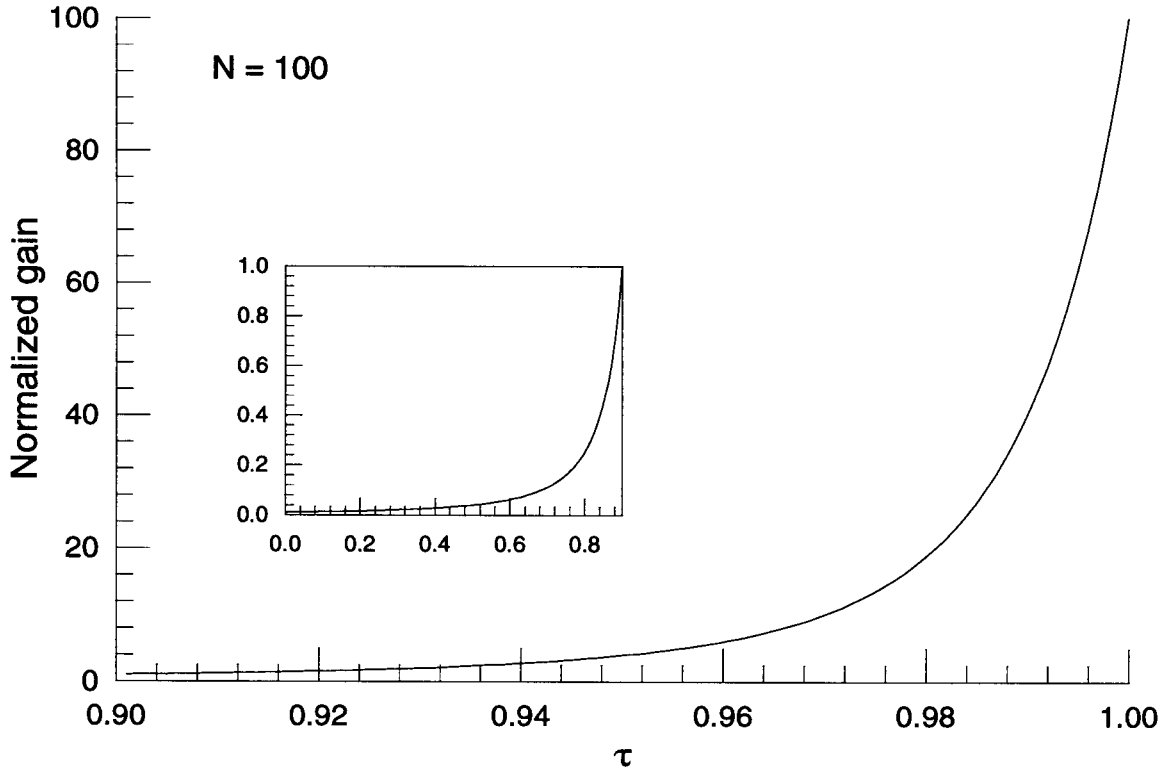
Figure 3.8: The on-resonance normalized gain of the BRAICER cavity for $N = 100$ and $d_{\mathrm{lp}} = d_{\mathrm{ib}}$ ($m = n = 1$). The inset shows the normalized gain for $\tau \leq 0.9$.

τ ($\tau \to 0$), the normalized gain is about $1/[N(1-\tau)^2]$, while for large τ ($\tau \to 1$), this gain approaches the maximum N. Hence, it is necessary to minimize the cavity loss (make τ as close to unity as possible) in order to have a significant signal gain.

3.2.6 The Offset Effect

The discussions of the resonance behavior of the BRAICER cavity so far assume that the electron bunches pass through the focal points of the parabolic mirrors P1 and P2. However, things do not always go like the "ideal" case. If the electron bunches pass through the cavity with an offset from the focal points of P1 and P2 demonstrated in Fig. 3.9, some of the resonances will be affected by this offset effect. For example, if
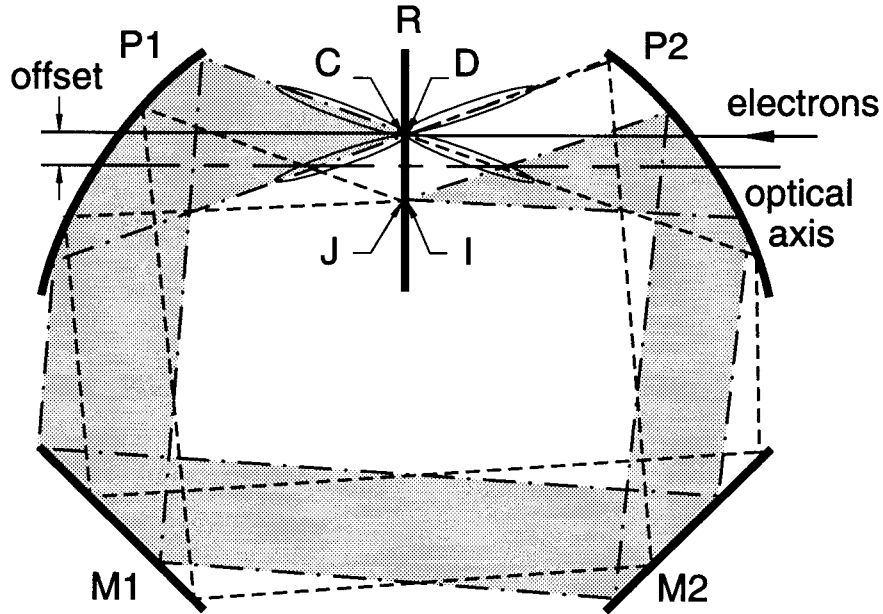
Figure 3.9: The offset effect in the BRAICER cavity. The electron bunches cross R (at C and D) with an offset from the optical axis defined by the focal points of P1 and P2. The image points of C and D are displaced to I and J, respectively.

the loop length is an integral (say m) multiple of d_{ib}, the radiation emitted from some bunch at C after a travel around the cavity will not meet the next m^{th} subsequent bunch at D to stimulate emission of radiation because the image point of C is displaced to I; however, this radiation will further travel back to C to meet the next $2m^{th}$ bunch with *two* loop-length-long travel. This is exactly the *second* order resonance, instead of the first one. On the other hand, resonances at half-integral multiples of d_{ib} will remain of the second order since the light pulses will meet the subsequent bunches at the same point where they are emitted after two-loop-length-long travel. In general, odd order resonances (say n^{th}, n odd) will in this case become even order $(2n^{th})$, while all even order resonances retain their order.

Because of this offset, the two series of light pulses E_k^{RHS} in Eq. (3.6) and E_k^{LHS} in Eq. (3.7) discussed in Sec. 3.2.4 will only stimulate radiation emitted from the same side of R; that is, E_k^{RHS} will only stimulate radiation emitted on the right-hand side of

R by subsequent electron bunches and vice versa. No stimulation on alternative sides will happen, and therefore E_k^{RHS} and E_k^{LHS} can be treated independently. Transforming Eqs. (3.6) and (3.7) into the frequency domain and summing over all electron bunches (with respect to k), we obtain

$$
\begin{aligned}
\tilde{E}^{\text{RHS}}(\omega) &= R\alpha^{d_{\text{lp}}/2} \sum_{k=0}^{N-1} \sum_{j=0}^{\infty} \left(\alpha^{d_{\text{lp}}} T\right)^{2j} \tilde{E}(\omega) e^{i\omega[k(d_{\text{ib}}/c)+2j(d_{\text{lp}}/c)]} \\
&= R\alpha^{d_{\text{lp}}/2} \tilde{E}(\omega) \sum_{k=0}^{N-1} e^{i\omega k(d_{\text{ib}}/c)} \sum_{j=0}^{\infty} \left(\alpha^{d_{\text{lp}}} T\right)^{2j} e^{i\omega 2j(d_{\text{lp}}/c)} \\
&= R\alpha^{d_{\text{lp}}/2} \tilde{E}(\omega) \frac{1 - e^{i\omega N d_{\text{ib}}/c}}{1 - e^{i\omega d_{\text{ib}}/c}} \frac{1}{1 - (\alpha^{d_{\text{lp}}} T)^2 e^{i\omega 2 d_{\text{lp}}/c}}
\end{aligned} \tag{3.23}
$$

and

$$
\begin{aligned}
\tilde{E}^{\text{LHS}}(\omega) &= R\alpha^{d_{\text{lp}}/2} \sum_{k=0}^{N-1} \sum_{j=0}^{\infty} \left(\alpha^{d_{\text{lp}}} T\right)^{2j+1} \tilde{E}(\omega) e^{i\omega[k(d_{\text{ib}}/c)+(2j+1)(d_{\text{lp}}/c)]} \\
&= R\alpha^{d_{\text{lp}}/2} \tilde{E}(\omega) \sum_{k=0}^{N-1} e^{i\omega k(d_{\text{ib}}/c)} \sum_{j=0}^{\infty} \left(\alpha^{d_{\text{lp}}} T\right)^{2j+1} e^{i\omega(2j+1)(d_{\text{lp}}/c)} \\
&= R\alpha^{d_{\text{lp}}/2} \tilde{E}(\omega) \frac{1 - e^{i\omega N d_{\text{ib}}/c}}{1 - e^{i\omega d_{\text{ib}}/c}} \frac{\alpha^{d_{\text{lp}}} T e^{i\omega d_{\text{lp}}/c}}{1 - (\alpha^{d_{\text{lp}}} T)^2 e^{i\omega 2 d_{\text{lp}}/c}}.
\end{aligned} \tag{3.24}
$$

Hence, the resulting total energy is the incoherent sum of the two contributions, i.e.,

$$
\begin{aligned}
\mathcal{E}_{\text{total}} &\propto \int_{-\infty}^{+\infty} d\omega \left[|\tilde{E}^{\text{RHS}}(\omega)|^2 + |\tilde{E}^{\text{LHS}}(\omega)|^2\right] \\
&= \int_{-\infty}^{+\infty} d\omega \, |R|^2 \alpha^{d_{\text{lp}}} |\tilde{E}(\omega)|^2 \left|\frac{1 - e^{i\omega N d_{\text{ib}}/c}}{1 - e^{i\omega d_{\text{ib}}/c}}\right|^2 \left[\left|\frac{1}{1 - (\alpha^{d_{\text{lp}}} T)^2 e^{i\omega 2 d_{\text{lp}}/c}}\right|^2\right. \\
&\quad \left. + \left|\frac{\alpha^{d_{\text{lp}}} T e^{i\omega d_{\text{lp}}/c}}{1 - (\alpha^{d_{\text{lp}}} T)^2 e^{i\omega 2 d_{\text{lp}}/c}}\right|^2\right] \\
&= \int_{-\infty}^{+\infty} d\omega \, |R|^2 \alpha^{d_{\text{lp}}} |\tilde{E}(\omega)|^2 \frac{\sin^2(\omega N d_{\text{ib}}/2c)}{\sin^2(\omega d_{\text{ib}}/2c)} \frac{1 + \alpha^{2 d_{\text{lp}}} |T|^2}{\left|1 - (\alpha^{d_{\text{lp}}} T)^2 e^{i\omega 2 d_{\text{lp}}/c}\right|^2}.
\end{aligned} \tag{3.25}
$$

This expression can be directly applied for beam splitters with varying R and T in the frequency domain. Based on the analysis discussed in Sec. 3.2.4, the resonance condition becomes

$$
\frac{d_{\text{lp}}}{d_{\text{ib}}} = \frac{m}{2n}, \tag{3.26}
$$

where m and n are two mutually primed integers. For example, if $d_{lp}/d_{ib} = 1$, then $m = 2$ and $n = 1$, which means that at this loop length, the light pulses have to travel $2n = 2$ loops to meet every other incoming bunch ($m = 2$). This is a second-order resonance if there is an offset; however, it would be a first-order resonance if there were no offset.

3.2.7 Reflection Losses of Metallic Reflectors

Since the BRAICER cavity consists mostly of reflectors to circulate the light pulses, the reflection loss from these reflectors becomes one of the major factors of cavity losses. In order to reduce reflection losses "good" reflectors are necessary for the construction of the cavity. As discussed in Sec. 2.1.3, silver, gold, and aluminum are good candidates of reflectors because their conduction properties are near perfect in the far-infrared regime. In this section, we will use the Drude model for silver, gold, and aluminum to calculate their reflectance in the far-infrared regime. These calculated results have been reported to have good agreement with experimental results[27–29].

By solving Maxwell's equations with appropriate boundary conditions, Fresnel's equations give the results for amplitude reflection and transmission coefficients. If the light travels from a medium of refractive index n_i into another medium of refractive index n_t at an angle θ_i with respect to the normal of the interface, then the amplitude reflection coefficients for parallel and perpendicular polarization are[12, Sec. 4.3]

$$r^{\parallel} = \frac{n_t \cos\theta_i - n_i \cos\theta_t}{n_t \cos\theta_i + n_i \cos\theta_t} = \frac{\tan(\theta_i - \theta_t)}{\tan(\theta_i + \theta_t)} \tag{3.27}$$

$$r^{\perp} = \frac{n_i \cos\theta_i - n_t \cos\theta_t}{n_i \cos\theta_i + n_t \cos\theta_t} = -\frac{\sin(\theta_i - \theta_t)}{\sin(\theta_i + \theta_t)}, \tag{3.28}$$

where θ_t is the angle of transmission and can be obtained from Snell's law:

$$n_i \sin\theta_i = n_t \sin\theta_t. \tag{3.29}$$

For the case of reflection from a metal, the refractive index is a complex number and has the following relation with its complex dielectric constant at angular frequency ω:

$$n(\omega) = \sqrt{\varepsilon(\omega)}, \tag{3.30}$$

where $\varepsilon(\omega)$ can be obtained from the Drude model as shown in Eq. (2.15). The real part of n describes the propagation of the wave, while the imaginary part of n describes the attenuation of the wave in the medium. The reflectances for parallel and perpendicular polarization are then defined as

$$R^{\parallel} = |r^{\parallel}|^2 \tag{3.31}$$

$$R^{\perp} = |r^{\perp}|^2. \tag{3.32}$$

By setting $n_i = 1$, $n_t = n(\omega)$ and using above equations and Eq. (2.15) with Table 2.1, the reflectances of silver, gold, and aluminum placed in air (or vacuum) are calculated. The dependencies on the incident angle at a fixed frequency of 10^{12} Hz are shown in Fig. 3.10 for both parallel and perpendicular polarization. For parallel polarization [cf., Fig. 3.10(a)], the reflectances slowly drop down as the incident angle increases and reach a minimum of about 0.2 at an angle of about 1.57 rad. For perpendicular polarization [cf., Fig. 3.10(b)], the reflectances slowly increase as the incident angle increases and reach unity at an angle $\pi/2$. The reflectances as functions of frequency at small (0.1 rad) and large (1.5 rad) angles are shown in Figs. 3.11 and 3.12 for both polarizations, respectively. The reflectances for both polarizations in both cases slowly drop down as the frequency increases. Overall, perpendicular polarization has higher reflectance than parallel polarization. Silver always has the highest reflectance, and aluminum, the lowest among the three good conductors. However, the difference is not significant. For small incident angles, reflectances are very close to unity for both polarization components. Such near perfect reflectance will help to minimize cavity losses and to maximize the signal gain.
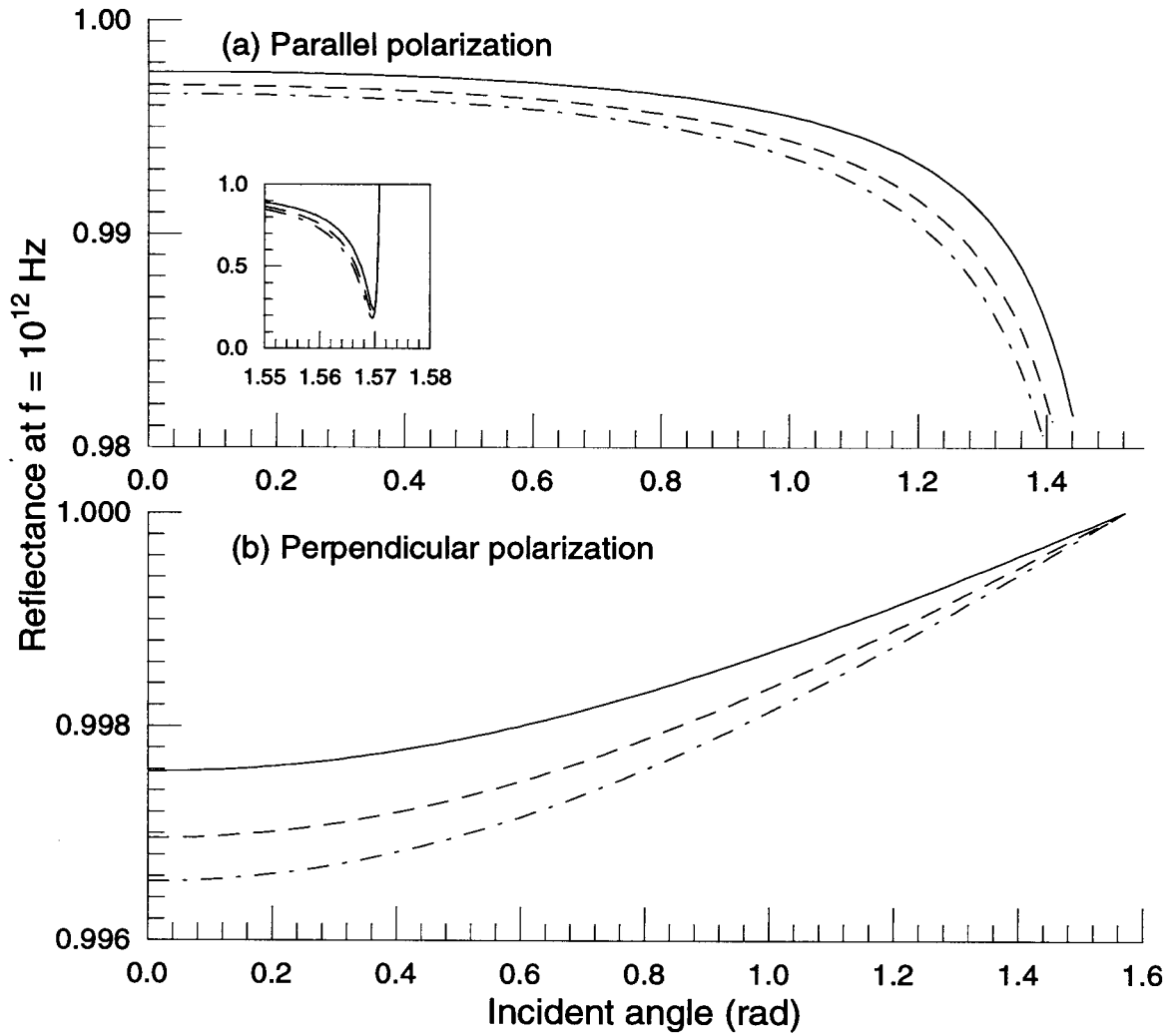
Figure 3.10: The reflectances of silver (solid), gold (dashed), and aluminum (dash-dotted line) as a function of incident angle for (a) parallel and (b) perpendicular polarization at frequency 10^{12} Hz. The inset in (a) magnifies the reflectances near the angle $\theta = \pi/2$.

Figure 3.11: The reflectances of silver (solid), gold (dashed), and aluminum (dash-dotted line) as a function of frequency at an incident angle $\theta = 0.1$ rad for (a) parallel and (b) perpendicular polarization.
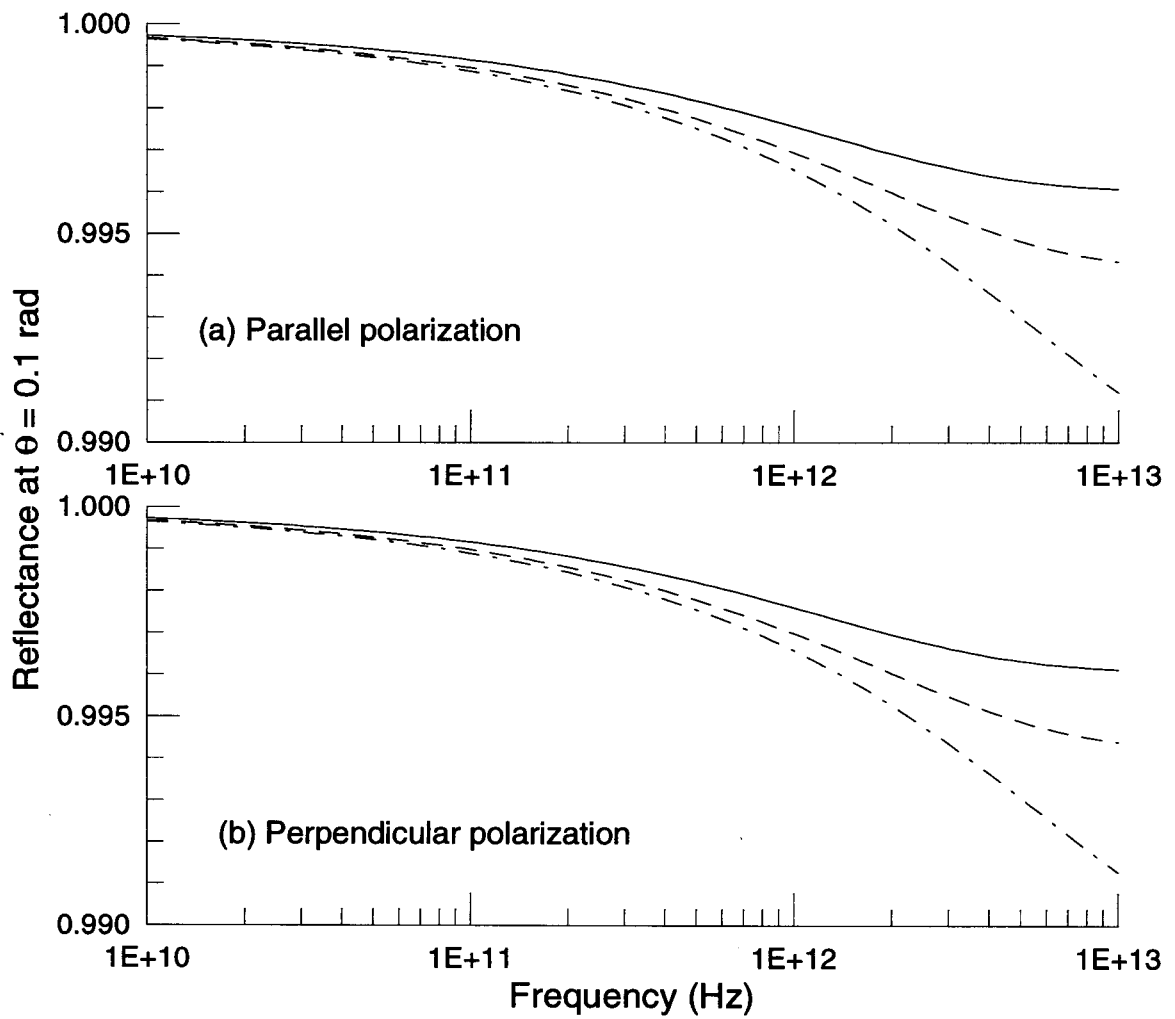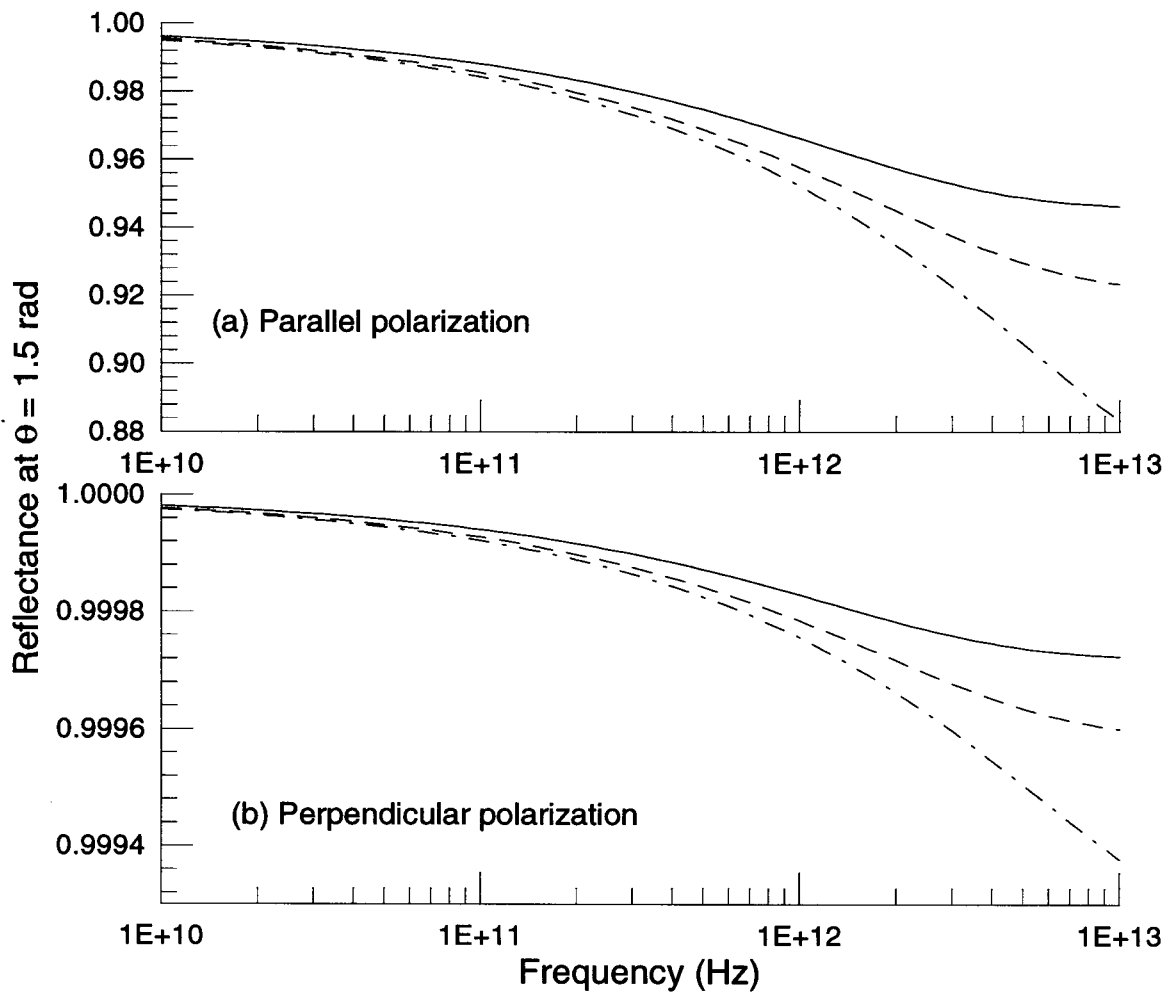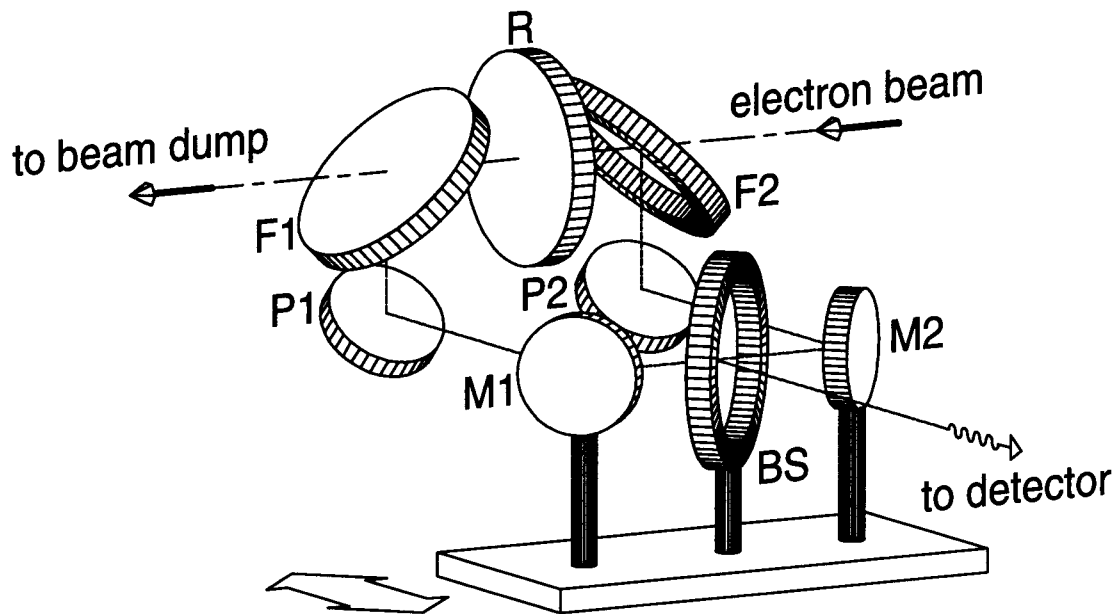
Figure 3.12: The reflectances of silver (solid), gold (dashed), and aluminum (dash-dotted line) as a function of frequency at an incident angle $\theta = 1.5\,\mathrm{rad}$ for (a) parallel and (b) perpendicular polarization.

Figure 3.13: Simplified schematic diagram of the experimental realization of the BRAICER cavity.

3.3 Experimental Verification

The theoretical results discussed in the previous section show a promising direction to produce high-power far-infrared radiation through the generation of stimulated coherent transition radiation from subpicosecond electron bunches in the BRAICER cavity. In this section, we will describe how to use the BRAICER cavity to verify this principle of stimulation for the first time experimentally at the SUNSHINE facility.

3.3.1 Experimental Setup

For this experiment, the SUNSHINE facility produces electron pulses at 10 Hz containing a train of about 3000 electron bunches at an energy of 30 MeV. Each bunch has about 2×10^8 electrons within a bunch length of about $200 \, \mu$m. The inter-bunch distance is 10.5 cm. By detecting radiation wavelengths longer than or equal to the

bunch length, we are able to observe stimulated coherent transition radiation in the far-infrared regime with a room-temperature bolometer.

A simplified schematic diagram of the experimental realization of the BRAICER cavity is shown in Fig. 3.13. It consists of a foil radiator/reflector (R), two foil reflectors (F1 and F2), two gold-coated off-axis parabolic reflectors of 152-mm effective focal length (P1 and P2), two gold-coated first-surface mirrors (M1 and M2), and a 127-μm-thick Mylar beam splitter supported by an aluminum ring (BS) using drumhead stretching principle. All foil reflectors (R, F1 and F2) are made of 8-μm-thick aluminum foils supported by aluminum rings stretched by the same method as that for the beam splitter. The focal points of P1 and P2 are aligned with the surfaces of R and with each other. The plane mirrors (M1 and M2) and the beam splitter (BS) are mounted to a remote-controlled linear translation stage. This allows us to change the loop length without affecting the alignment of the cavity. Some radiation is coupled out by a beam splitter and collected into a room-temperature pyroelectric bolometer through a copper light-cone. This light-cone and the bolometer combination will collect all the photons coupled out of the cavity through the beam splitter and produce a signal representing the total energy of the collected radiation. Hence, any increase in the output signal indicates additional energy produced by stimulation.

Presently, the whole cavity is placed in air. The electrons are extracted from the evacuated beam line through a 75-μm-thick stainless steel window. They cross the cavity through the foils (F2, R, and F1), and are finally absorbed into a beam dump. We simplify the assembly and alignment problems by placing the cavity in air but suffer from multiple scattering problems caused by electrons passing through the stainless steel window and the air, which reduces the radiation signal. Additionally, radiation is absorbed by humidity resulting in significant cavity losses. Forward transition radiation emitted from F2 and the backward one emitted from F1 will not be amplified by the cavity because of geometry but will contribute to the background.

This is also true for Cherenkov radiation emitted in air.

3.3.2 Results

By performing detuning measurements on the cavity, we are able to scan through its different resonances. This detuning procedure is carried out by measuring radiated energy into the bolometer as a function of the loop length. A typical detuning scan is shown in Fig. 3.14(a) where the loop length varies from $7\frac{1}{2}d_{ib}$ to $8d_{ib}$. Three resonances are observed in this range located at $7\frac{1}{2}d_{ib}$, $7\frac{3}{4}d_{ib}$, and $8d_{ib}$. A theoretical prediction using Eq. (3.11) for a perfectly aligned cavity-beam system, in which the electron bunches cross the focal points of P1 and P2 (cf., Fig. 3.3), is shown in Fig. 3.14(b). Electron beam parameters mentioned above along with the assumptions of uniform bunch distribution and 70% cavity losses, which is chosen to match the measurements, are used in the simulation. The comparison of experimental results and calculations is based on the relative heights of resonant peaks to their baselines. Although the second order resonance at $7\frac{1}{2}d_{ib}$ and the fourth order resonance at $7\frac{3}{4}d_{ib}$ agree with theory, there are still two major discrepancies between the two results: (1) the third order resonance at $7\frac{2}{3}d_{ib}$ in the measurement does not show the expected amplitude predicted by theory, and (2) the resonances at $8d_{ib}$ in both results behave differently.

By inspecting the oxidation trace on R, F1 and F2 caused by the electrons, we conclude that the electrons pass through R with an offset from the focal points of P1 and P2. This offset case is shown in Fig. 3.9 and discussed in Sec. 3.2.6. The theoretical simulation of the offset effect using Eq. (3.25) is shown in Fig. 3.14(c) and agrees with the measured scan for all the resonant peaks. The absence of odd order resonances in the measurement further indicates that the measured resonant peaks are real stimulation of radiation, instead of interference effects between radiation pulses. For example, at $7\frac{2}{3}d_{ib}(= \frac{23}{3}d_{ib})$ the radiation emitted from C by a bunch after a three-loop-length-long travel will co-propagate in the cavity with the radiation emitted
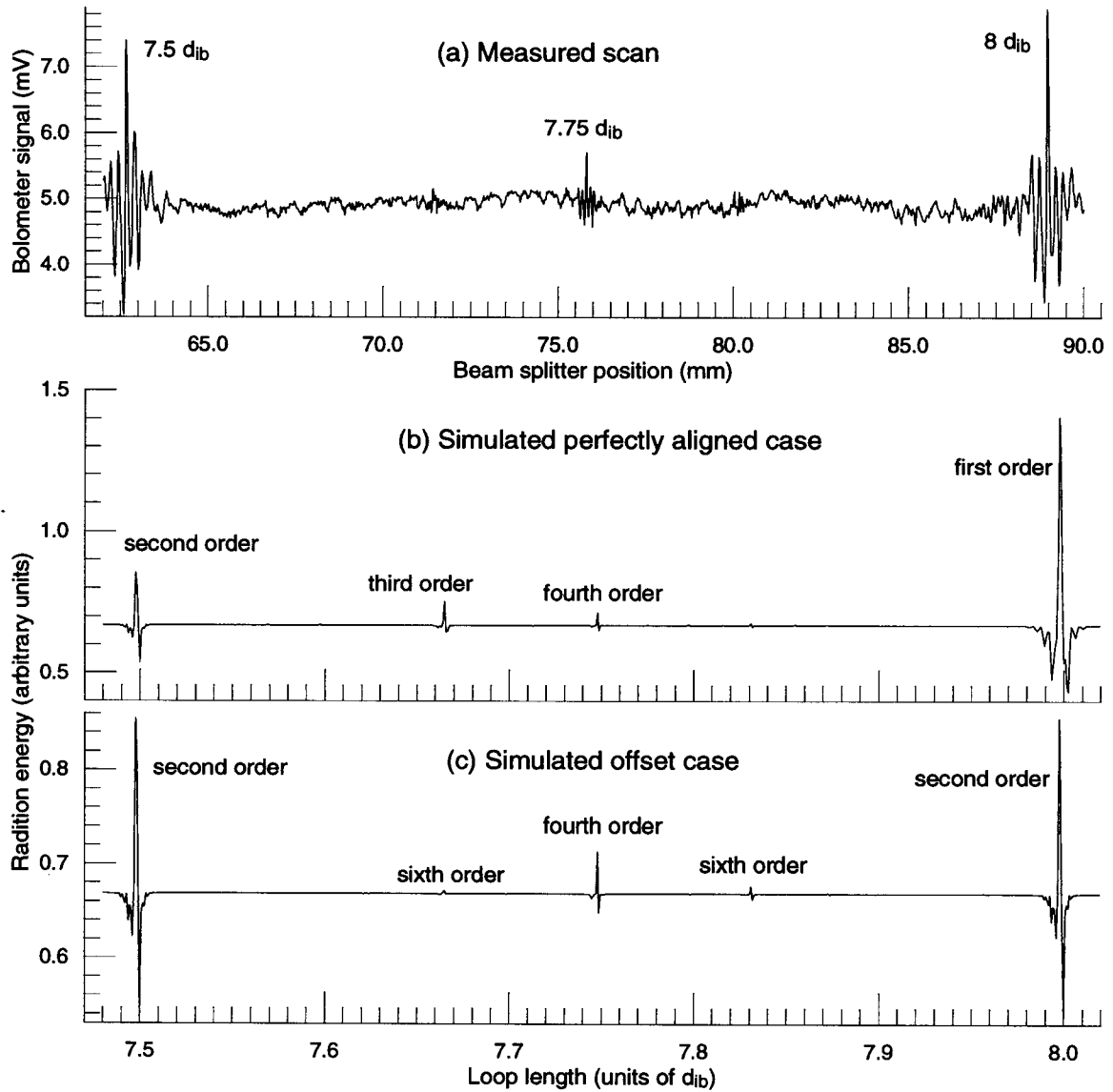
Figure 3.14: Typical experimental and theoretical detuning scans of the BRAICER cavity. An experimental scan is shown in (a) where the loop length varies from $7\frac{1}{2}d_{\mathrm{ib}}$ to $8d_{\mathrm{ib}}$. Note that a change of δ in the beam splitter position corresponds to 2δ in actual loop length. The theoretical predictions are shown in (b) for a perfectly aligned case and in (c) for an offset case.

from D by the next 23rd bunch. The two light pulses do not stimulate each other to produce more radiated energy because of the offset; instead, they interfere without producing any extra energy. No interference effects due to these two co-moving pulses are observed at this loop length, which confirms that the bolometer only measures the change in total energy due to stimulation, not the local intensity enhancement due to interference effect. In addition, the resulting 6th order resonance at this loop length predicted by the theory with the offset effect is too small to have a clear observation.

3.3.3 Measurement Summary

We have described the experimental verification of stimulated coherent transition radiation through a BRAICER cavity. Utilizing subpicosecond electron bunches produced at the Stanford SUNSHINE facility, we are able to observe the coherent part, whose wavelengths are longer than or equal to the bunch length, of stimulated radiation in the far-infrared regime via a room-temperature bolometer. By performing a detuning scan of the cavity, resonant peaks of the cavity have been observed. These resonances along with theoretical simulations confirm the observation of stimulated transition radiation for the first time. This implies that a BRAICER cavity can be used to generate high-power coherent far-infrared radiation through stimulated emission of coherent transition radiation. To achieve this, a new vacuum compatible cavity design is required to eliminate air's absorption losses and scattering of the electron beam through the stainless steel window.

3.4 Alternative Designs

The observation of stimulated coherent transition radiation through the BRAICER cavity described in the previous section has proved the principle of using stimulation of coherent transition radiation emitted from subpicosecond electron bunches to produce
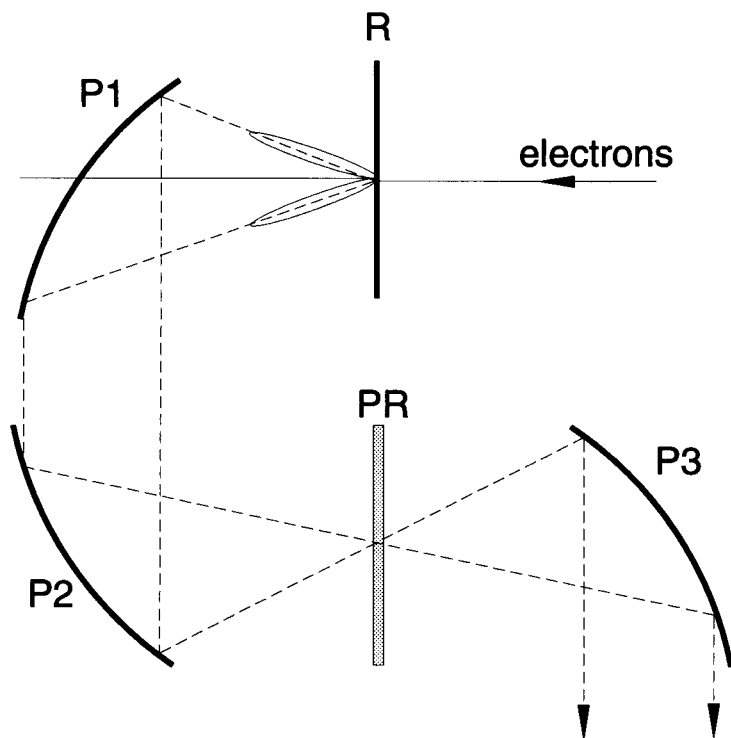
Figure 3.15: An offset insensitive BRAICER cavity design.

high-intensity far-infrared radiation. However, the design of the cavity shown in Fig. 3.3 and the experimental setup used to prove this principle are not suitable for the purpose of high-intensity light production because of high cavity losses and sensitivity to alignment errors. Hence, new designs optimized for this purpose have to be studied. One major design change to reduce cavity losses is to enclose the whole cavity in an evacuated environment to eliminate air absorptions and the electron multiple scattering problem due to an extra vacuum protection window. In this section, we will show two different optics design principles for different modes of operation.

3.4.1   An Offset Insensitive Design

One optical design change to increase the signal gain is to use an offset insensitive design so that the image of the beam can trace the change in the incidence point and make the stimulation more efficient. Such design will also ease alignment requirements on some parts. An offset insensitive BRAICER cavity design is shown in Fig. 3.15. This cavity consists a radiator/reflector (R), two paraboloidal mirrors (P1 and P2), one partial reflector (PR), and one output light collecting mirror (P3). This cavity only circulates transition radiation emitted from one side of R. The focal points of P1 and P2 are aligned with the mirror-facing surfaces of R and PR, respectively.

As shown in the figure, divergent rays of forward transition radiation emitted from ·the left-hand side of R are converted to parallel rays by P1, and focused to a point on PR by P2. Some parts of the light are reflected by PR and travel back to the original emitting point to meet subsequent incoming electron bunches, while the remaining parts transmit through PR and are collected by P3 into the application apparatus. The amount of energy coupled out of the cavity is controlled by the reflectivity of the partial reflector PR, which can be as simple as a thin coat of good conducting metal on a supporting substrate such as a Mylar foil. The polarization of the stimulation field is aligned with the spontaneous field and enables stimulated emissions from subsequent bunches. This condition is, for example, not fulfilled if a plane mirror were inserted between P1 and P2. Similar to the original BRAICER design, this design is operated in the *multi-pulsed* mode, which will output a train of light pulses while the electron bunches are passing through the cavity.

3.4.2   A Q-switched Design

The offset insensitive design described in the previous section will eliminate the offset effect which occurred in the original BRAICER design and increase the efficiency of
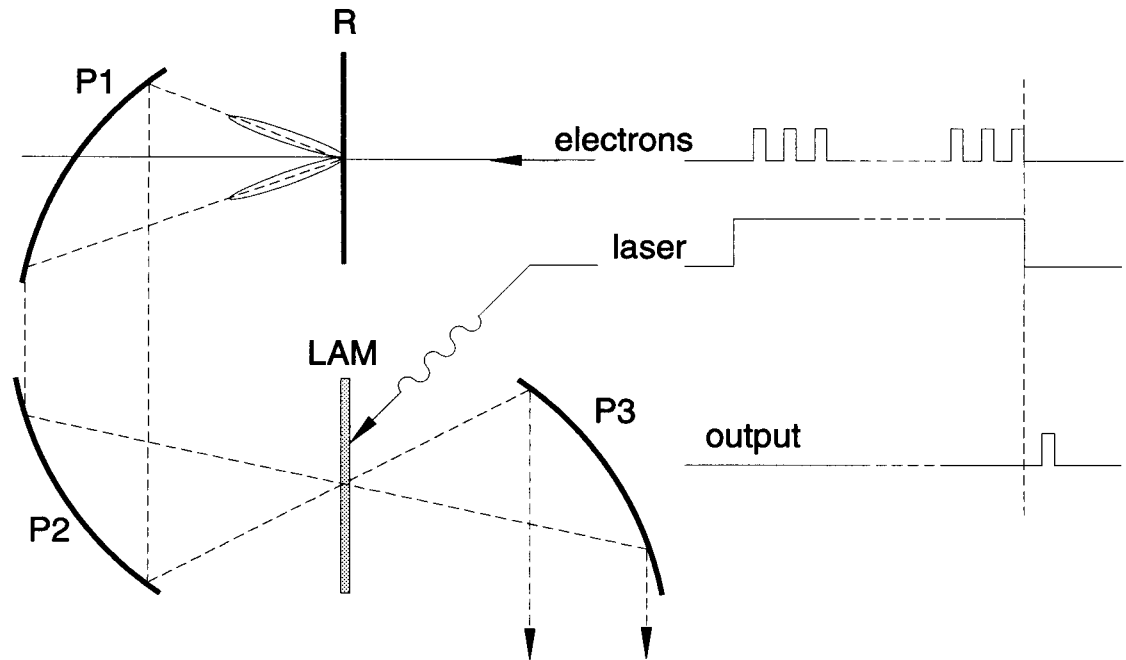
Figure 3.16: A Q-switched BRAICER cavity design. The timing of the electron bunches, the laser pulse, and the output light pulse for the first resonance of the first order [i.e., $(m, n) = (1, 1)$] are shown in the right part of the figure.

stimulation by increasing the overlapping of stimulation fields and electron bunches. However, the presence of the partial reflector PR makes it impossible to increase both the cavity gain and the output intensity at the same time since a constant portion of the energy is always coupled out of the cavity when the electron bunches are present. In order to increase the cavity gain, a switching mechanism has to be introduced into the cavity design. This mechanism will maximize the cavity gain (or the Q factor of the cavity) while the bunches are passing through the cavity and then maximize the output intensity (so the Q factor of the cavity is reduced) after the bunches have passed the cavity. This, in laser terminology, is called the *Q-switched* method.

A Q-switched BRAICER cavity design is shown in Fig. 3.16. This design has basically the same structure as the offset insensitive design shown in Fig. 3.15 except now the partial reflector PR is replaced by a laser-activated mirror LAM. Derived

from the offset insensitive design, this Q-switched design is also free from the offset problem. The laser activated mirror will become highly reflective when the laser is shining on it and highly transparent for waves in the far-infrared regime when the laser is turned off. A candidate for such mirror is, for example, a mirror made of semi-conducting material. When the laser with a photon energy greater than the bandgap of the mirror material shines on the mirror, the electrons in the mirror are excited into the conduction band, and the mirror becomes a good conductor, which is highly reflective for waves in the far-infrared regime. On the other hand, when the laser is turned off, the far-infrared coherent radiation does not have enough energy to excite electrons into the conduction band, and the mirror acts like a dielectric material, which is transparent for the coherent radiation. Hence, if the laser is turned on when the electron bunches are passing through the cavity, the cavity will resonate with very high gain (assuming the cavity loss is minimized). For the mth resonance of the nth order, there are only m light pulses circulating in the cavity and the intensity increases quadratically with the number of encountered electron bunches. When the last electron bunch has passed through the cavity, the laser is turned off to allow these m high-intensity light pulses to be released into the experimental apparatus through P3. The only requirement on the activating laser pulse is a very sharp trailing edge to allow the circulating light pulses to be released in a very short time period. There is no special requirement on the duration of the laser pulse except that it has to be longer than the duration of the electron bunch train.

Unfortunately, current laser technology and available materials make it difficult to realize this Q-switched design[55]. If the laser-activated mirror LAM is made of available semi-conducting materials, the laser required to activate the mirror has to be able to produce immense radiation energy within about $1\,\mu s$ to match electron beam conditions at SUNSHINE. Such lasers are not achievable with current technology. The reflectance of the mirror is not near perfect (~ 0.99) when the laser is shining
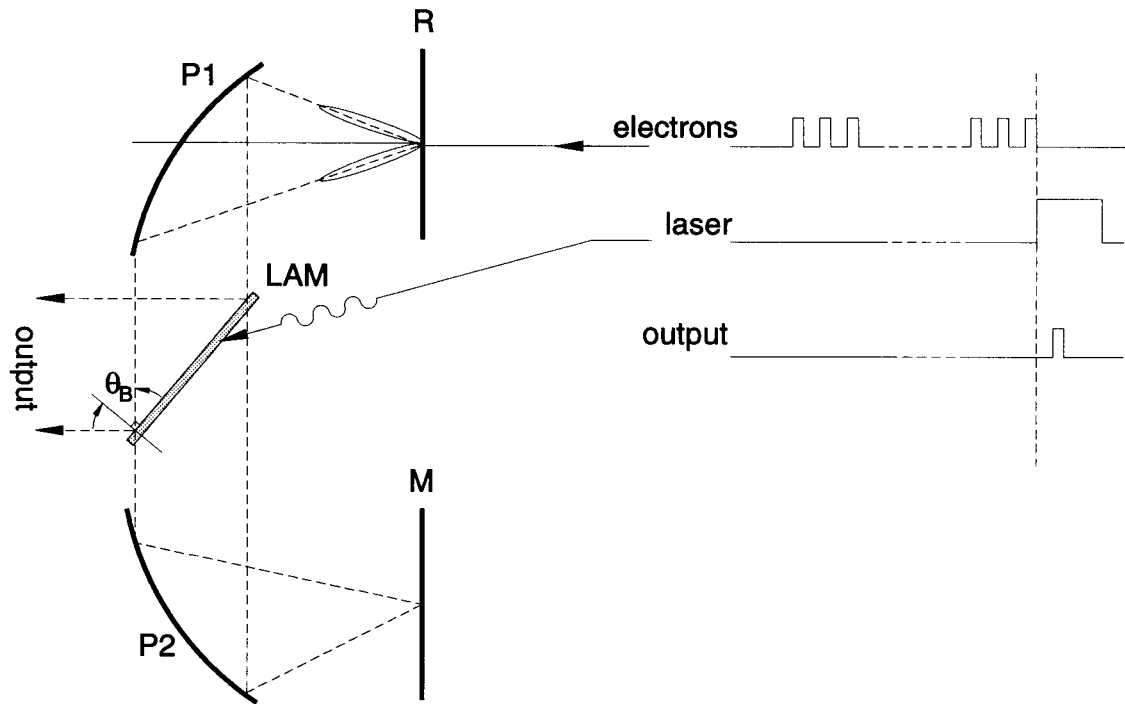
Figure 3.17: An alternative Q-switched BRAICER cavity design. The timing of the electron bunches, the laser pulse, and the output light pulse for the first resonance of the first order [i.e., $(m, n) = (1, 1)$] are shown in the right part of the figure.

on it. This poses a significant limit on the gain of the cavity. In addition, the carrier decay in the mirror is rather slow compared to the light-pulse duration after the laser is turned off. During this slow transition, light pulses in the cavity will be absorbed by the carrier-decay process. However, these constraints may be relieved when the laser technology is advanced, and new materials are discovered.

In order to utilize available semi-conducting materials as the laser-activated mirror in the Q-switched design, an alternative design of the Q-switched BRAICER cavity is shown in Fig. 3.17[55]. This cavity has the basic structure of the previous one (cf., Fig. 3.16) except that the laser-activated mirror **LAM** is inserted between **P1** and **P2**, and the end of the cavity is replaced by a plane mirror **M**. The normal of **LAM** is oriented at an angle equal to Brewster's angle with respect to the parallel rays.

Brewster's angle of a material with refractive index n placed in air (or vacuum) is defined as[12, Sec. 8.6]

$$\tan \theta_B = n. \tag{3.33}$$

When the angle of incidence is equal to Brewster's angle, 100% transmission is achieved for the polarization component parallel to the plane of incidence. As electron bunches are passing through the cavity and **LAM** is not activated by the laser, the polarization component parallel to the plane of incidence at **LAM** has 100% transmission through **LAM** and is amplified in the cavity with the maximum gain. However, the perpendicular component suffers reflection losses through **LAM** and is not amplified. The light circulating in this cavity is, therefore, polarized. After all electron bunches have passed, the laser is then turned on and activates **LAM** to dump light pulses out of the cavity. The three constraints discussed in the previous paragraph will not affect the operation of this design because of the following reasons. First, the laser does not have to be turned on for a long duration because the dumping of light pulses takes a few bunch repetition periods (d_{ib}/c). This eases the requirement on the total laser output energy and makes current laser technology applicable to this design. Secondly, the about 99% reflectance of **LAM** when it is laser-activated is enough for the light-pulse dumping purpose. Finally, the long carrier-decay time does not affect this operation since the laser can be turned off after light pulses have been dumped.

Bibliography

[1] H. Motz, J. Appl. Phys. **22**, 527 (1951).

[2] J. S. Nodvick and D. S. Saxon, Phys. Rev. **96**, 180 (1954).

[3] M. Born and E. Wolf, *Principle of Optics*, 6th Ed. (Pergamon Press, Oxford, 1989), Sec. 10.4.2(a).

[4] H.-C. Lihn, "Simulation of coherent synchrotron radiation from an ultra-short electron bunch," Stanford Synchrotron Radiation Laboratory ACD Note No. 124, Stanford, California, 1992.

[5] M. Abramowitz and I. A. Stegun, *Handbook of Mathematical Functions*, Applied Mathematical Series, Vol. 55 (Washington: National Bureau of Standards; reprinted by Dover Publications, New York, 1968), Eqs. (9.3.35) and (9.3.45) in Ch. 9.

[6] H. Wiedemann, *Particle Accelerator Physics*, Vol. 1 (Springer-Verlag, Berlin, 1993), Sec. 4.3.1.

[7] K.-J. Kim, and A. Sessler, Science **250**, 88 (1990).

[8] University of California at Santa Barbara FEL facility, `http://www.qi.ucsb.edu/cfels/`, (Santa Barbara, California, 1996).

[9] Stanford Picosecond FEL Research Center, `http://www-leland.stanford.edu/group/FEL/`, (Stanford, California, 1996).

[10] The CLIO FEL facility, `http://www.lure.u-psud.fr/www/lure/`, (LURE, Orsay, France, 1996).

[11] The FELIX Infrared FEL facility, `http://www.nikhefk.nikhef.nl/~ed/direct/nederland.html#15`, (Nieuwegein, Netherlands, 1996).

[12] E. Hecht and A. Zajac, *Optics* (Addison-Wesley, Reading, Massachusetts, 1974).

[13] H. Wiedemann, P. H. Kung, and H.-C. Lihn, Nucl. Instr. and Meth. in Phys. Res. **A319**, 1 (1992).

[14] M. Borland, *A High-brightness Thermionic Microwave Electron Gun*, Ph.D. thesis (Stanford University, Stanford, California, 1991).

[15] P. H. Kung, *Generation and Characterization of Subpicosecond Electron Bunches*, Ph.D. thesis (Stanford University, Stanford, California, 1995).

[16] P. H. Kung, H.-C. Lihn, D. Bocek, and H. Wiedemann, Proc. SPIE **2118**, 191 (1994).

[17] P. H. Kung, H.-C. Lihn, D. Bocek, and H. Wiedemann, Phys. Rev. Lett. **73**, 967 (1994).

[18] H.-C. Lihn, P. H. Kung, D. Bocek, and H. Wiedemann, AIP Conference Proceedings **333**, 231 (1995).

[19] T. Nakazato *et al.*, Phys. Rev. Lett. **63**, 1245 (1989).

[20] E. B. Blum, U. Happek, and A. J. Sievers, Nucl. Instr. and Meth. in Phys. Res. **A307**, 568 (1991).

[21] D. E. Williamson, J. Opt. Soc. Am. **42**, 712 (1952).

[22] V. L. Ginsburg and I. M. Frank, Zh. Eksp. Teor. Fiz. **16**, 15 (1946).

[23] J. D. Jackson, *Classical Electrodynamics*, 2nd Ed. (John Wiley & Sons, New York, 1975).

[24] M. L. Ter-Mikaelian, *High-energy Electromagnetic Processes in Condensed Media* (Wiley-Interscience, New York, 1972), Ch. 4.

[25] F. Wooten, *Optical Properties of Solids* (Academic Press, New York, 1972), Sec. 3.2.

[26] M. H. Cohen, Philos. Mag. **3**, 762 (1958).

[27] H. E. Bennett and J. M. Bennett, in *Optical Properties and Electronic Structure of Metals and Alloys*, edited by F. Abelès (North-Holland, Amsterdam, 1966), p. 175.

[28] D. Y. Smith, E. Shiles, and M. Inokuti, in *Handbook of Optical Constants of Solids*, edited by E. D. Palik (Academic Press, New York, 1985), p. 369.

[29] D. Y. Smith and B. Segall, Phys. Rev. **B34**, 5191 (1986).

[30] L. C. Yuan, C. L. Wang, and S. Prünster, Phys. Rev. Lett. **23**, 496 (1969).

[31] M. L. Cherry, G. Hartmann, D. Müller, and T. A. Prince, Phys. Rev. **D10**, 3594 (1974).

[32] L. Durand, Phys. Rev. **D11**, 89 (1975).

[33] M. A. Piestrup, M. J. Moren, B. L. Berman, P. Pianetta, and D. Seligson, Proc. SPIE **773**, 37 (1987).

[34] L. Wartski, S. Roland, J. Lasalle, and G. Filippi, J. Appl. Phys. **46**, 3644 (1975).

[35] U. Happek, A. J. Sievers, and E. B. Blum, Phys. Rev. Lett. **67**, 2962 (1991).

[36] Y. Shibata *at el.*, Phys. Rev. A45, R8340 (1992).

[37] V. L. Ginzburg and V. N. Tsytovich, Phys. Rep. (Rev. Sec. Phys. Lett.) 49, 1 (1979).

[38] R. L. Fork, B. I. Greene, and C. V. Shank, Appl. Phys. Lett. 38, 671 (1981).

[39] W. Barry, "An autocorrelation technique for measuring subpicosecond bunch length using coherent transition radiation," in *Proceedings of the Workshop on Advanced Beam Instrumentation* 1, KEK, Tsukuba, Japan, April 22-24, 1991 (unpublished); CEBAF Preprint No. PR-91-012.

[40] H.-C. Lihn, P. H. Kung, C. Settakorn, D. Bocek, and H. Wiedemann, "Measurement of subpicosecond electron pulses," Phys. Rev. E, to be published (1995); SLAC PUB 95-6958 (1995).

[41] R. J. Bell, *Introductory Fourier Transform Spectroscopy* (Academic Press, London, 1972), Ch. 9.

[42] G. W. Chantry, *Submillimetre Spectroscopy* (Academic Press, London, 1971), App. A.

[43] P. L. Richards, J. Opt. Soc. Am. 54, 1474 (1964).

[44] R. Lai, U. Happek, and J. Sievers, Phys. Rev. E 50, R4294 (1994).

[45] Y. N. Dnestrovskii and D. P. Kostomarov, Doklady Akad. Nauk 124, 792 (1959) [Sov. Phys. Doklady 4, 132 (1959)] and Doklady Akad. Nauk 124, 1026 (1959) [Sov. Phys. Doklady 4, 158 (1959)].

[46] Y. Shibata *et al.*, "Observation of coherent diffraction radiation from bunched electrons passing through a circular aperture in the millimeter and submillimeter region," Phys. Rev. E, submitted (1995).

[47] E. R. Crosson, K. W. Berryman, T. I. Smith, R. L. Swent, H.-C. Lihn, and H. Wiedemann, Nucl. Instrum. Methods Phys. Res. A358, 216 (1995).

[48] D. J. Kane and R. Trebino, IEEE J. Quantum Electron. 29, 571 (1993).

[49] H. Stark, *Image Recovery: Theory and Application* (Academic, Orlando, 1987).

[50] J. R. Fienup, Opt. Lett. 3, 27 (1978), Appl. Opt. 21, 2758 (1982), and J. Opt. Soc. Am. A3, 1897 (1986).

[51] G. R. Ayers and J. C. Dainty, Opt. Lett. 13, 547 (1988) and J. H. Seldin and J. R. Fienup, J. Opt. Soc. Am. A7, 428 (1990).

[52] H.-C. Lihn, D. Bocek, P. H. Kung, M. Hernandez, C. Settakorn, and H. Wiedemann, "First observation of stimulated coherent transition radiation," Phys. Rev. Lett., submitted (1995); SLAC PUB 95-6913 (1995).

[53] Y. N. Istomin and A. V. Luk'yanov, Zh. Eksp. Teor. Fiz. 97, 1578 (1990) [Sov. Phys. JETP 70, 891 (1990)].

[54] V. L. Ginzburg and V. N. Tsytovich, *Transition Radiation and Transition Scattering* (Adam Hilger, Bristol, 1990).

[55] T. I. Smith, private communication.